Static and dynamic electronic structure of ferromagnetic Ni metal and Co$_2$FeSi Heusler alloy studied by photoemission spectroscopy

vorgelegt von
Magister in Physik
Ruslan Ovsyannikov

von der Fakultät II – Mathematik und Naturwissenschaften
der Technischen Universität Berlin
zur Erlangung des akademischen Grades

Doktor der Naturwissenschaften
– Dr.rer.nat. –

genehmigte Dissertation

Promotionsausschuss:

Vorsitzender: Prof. Dr. M. Dähne
Berichter: Prof. Dr., Dr. h.c. W. Eberhardt
              Prof. Dr. S. Eisebitt
              Prof. Dr. W. Kuch

Tag der wissenschaftlichen Aussprache 2 September 2009

Berlin 2009
D 83

"Give me four parameters and I can fit an elephant. Give me five and I can wag its tail."

Variants of this phrase have been attributed to C.F. Gauss, Niels Bohr, Lord Kelvin, Enrico Fermi.

Abstract

Spintronics, also known as magnetoelectronics, is an emerging technology involving detection and manipulation of the electron spin in addition to the electron charge. High spin polarization at Fermi level is an important issue for spintronics applications. One of the promising candidates are half metallic ferromagnets.

The first part of this thesis contains a study of the Co_2FeSi Heusler alloy. For this system 100% spin polarization at the Fermi edge was predicted, but experimentally obtained values of 10-12% were significantly lower. In this a work novel spin resolved specto-microscopy technique was applied to study Co_2FeSi Heusler alloys. Effects of sample preparation on surface stoichiometry were observed and reduced as much as possible. The obtained spin polarization at the Fermi level of 16% is the highest experimentally determined so far for this material.

Another important issue for spintronics applications is the lifetime of the spin polarized carriers. The ultimate performance of spintronics devices is determined by the lifetimes of spin-polarized charge carriers, especially at interfaces, thus attracting a lot of attention to the electronic structure and the dynamic properties of strongly correlated electron systems like $3d$-ferromagnets, transition metal oxides and $4f$-rare-earths systems. Although the theoretical description of the electron scattering processes exists, the influence and the roles that these processes play in device performance are still open questions. Hence a better understanding of the electronic interactions in model systems is imperative.

The second part of the thesis deals with electron correlation effects in case of nickel bulk, a model system of an itinerant ferromagnet. At low temperature kink structures due to coupling of electronic to bosonic excitations for the minority bands were resolved. Coupling parameters obtained in this work are slightly less than reported before. This difference was attributed to different points in $\mathbf{k}$ space probed in this work. Contrary to the literature was proposed

to relate the kink not to the electron-phonon interaction but to an electron-magnon interaction. This explains unambiguously the absence of kinks for the majority bands.

With increasing temperature a decreasing quasiparticle lifetime at the Fermi level for all probed minority spin bands was observed as expected for electron-boson coupling. Surprisingly the majority spin states behave differently. A slightly increased lifetime at room temperature was observed. The corresponding increase in Fermi velocity points to a temperature dependent reduction of the majority spin quasiparticle renormalization. The microscopic origin of this novel effect is still unclear. Clearly studies over a extended temperature range are required.

Zusammenfassung

Spintronik, auch bekannt als Magneto-Elektronik, ist eine sich entwickelnde Technologie basierend auf der Detektion and Manipulation des Elektronenspins zusätzlich zur elektrischen Ladung. Eine hohe Spinpolarisation der Ladungsträger am Fermi-Niveau ist für Spintronikanwendungen von wesentlicher Bedeutung. Einige der vielversprechendsten Kanditaten für zum Einsatz kommende Materialien sind halbmetallische Heuslerlegierungen.

Der erste Teil der vorliegenden Dissertation beschäftigt sich mit der Heuslerlegierung Co_2FeSi. Für dieses Material wurde eine Spinpolarisation am Fermi-Niveau von 100% vorhergesagt, jedoch bisher nur 10-12% experimentell nachgewiesen. In dieser Arbeit kam eine neu entwickelte Spektromikroskopie zum Einsatz um die Co_2FeSi Heuslerlegierung zu untersuchen. Effekte der Probenpräparation auf Oberflächenstochiometrie wurden untersucht und soweit möglich reduziert. Die daraufhin beobachtete Spinpolarisation am Fermi-Niveau von 16% ist der bisher Höchste experimentell nachgewiesene Wert für dieses Material.

Ein weiteres wichtiges Thema für Spintronikanwendungen ist die Lebensdauer spinpolarisierter Ladungsträger. Die Leistungsfähigkeit von Spintronikanwendungen ist grossteils bestimmt durch die Lebensdauer spinpolarisierter Ladungsträger, besonders an Grenzflächen. Deshalb ist es von besonderer Bedeutung die elektronische Struktur und das dynamisch Verhalten von Ladungsträgern in 3d Ferromagneten, übergangsmetalloxyden und Seltene-Erdsystemen zu untersuchen. Die theoretische Beschreibung von Elektronenstreuprozessen existiert zwar, ihre Bedeutung für die Leistungsfähigkeit von Bauteilen ist jedoch eine offene Frage. Das bessere Verständnis der elektronischen Wechselwirkungen in Modellsystemen ist deshalb von grundlegender Bedeutung.

Der zweite Teil dieser Dissertation beschäftigt sich mit elektronischen Korrelationseffekten in Nickel, dem Beispiel eines itineranten Ferromagneten. Sogenannte Kinks, d.h. die Renormierung der Banddispersion und der Linien-

breite, in der Ni Bandstruktur, verursacht durch Kopplung von elektronischen zu bosonischen Anregungen, wurden für tiefe Probentemperaturen spektroskopisch aufgelöst. Die in dieser Arbeit ermittelten Kopplungsparameter sind etwas kleiner als entsprechende Literaturwerte. Dieser Unterschied ist erklärbar durch die unterschiedlichen Bereiche der Brillouinzone, die in dieser Arbeit geprobt wurden. Im Gegensatz zur Literaturmeinung schlagen wir von die beobachteten Kinks nicht durch Elektron-Phonon Kopplung zu erklären sonder mit der Wechselwirkung von Elektronen mit Magnonen. Dies erklärt zwanglos die Abwesenheit der Kinks für Majoritätsspinbänder.

Mit ansteigender Temperatur wurde die für Elektron-Boson-Kopplung erwartete Erniedrigung der Quasiteilchenlebensdauer für alle gemessenen Ni Minoritätsspinbänder beobachtet. überraschenderweise verhalten sich die Majoritätsspinbänder anders. Ein leichtes Anwachsen der Lebensdauer bei Raumtemperatur wurde beobachtet. Dei damit einhergehende Erhöhung der Fermigeschwindigkeit deutet auf eine temperaturabhängige Reduktion der Majoritätsspin-Quasiteilchenrenormierung hin. Die mikroskopische Ursache für diesen neuartigen Effekt ist jedoch immer noch unklar und weitere temperaturabhägige Studien über einen erweiterten Temperaturbereich werden benötigt.

Contents

List of Abbreviations

ADC   angular distribution curve

AIS   angle integrated spectum

ARPES   angle-resolved photoelectron spectroscopy

b.c.c.   bulk centered cubic (crystal structure)

BZ   Brillouin zone

DDL   dispersion dependent line shape

DOS   density of states

EDC   energy distribution curve

f.c.c.   face centered cubic (crystal structure)

FWHM   full width half maximium

GMR   giant magnetoresistance

HMF   half metallic ferromagnet

HWHM   half width half maximum

LDA   local density approximation

MDC   momentum distribution curve

MFP   mean free path

PEEM   photoemission electron microscopy

SPEEM   spin-resolved photoemission electron microscopy

TMR   tunnel magnetoresistance

UHV   ultra-high vacuum

XAS   x-ray absorption spectroscopy

XMCD   x-ray magnetic circular dichroism

XMLD   x-ray magnetic linear dichroism

XPS   x-ray photoelectron spectroscopy

Chapter 1

Introduction

Spintronics, also known as magnetoelectronics, is an emerging technology involving detection and manipulation of the electron spin in addition to the electron charge. In order to perform such an operation two primary types of systems are required – a system that could generate a spin polarized current, a so called spin-injector and a system that is sensitive to the spin polarization i.e., a so called a spin detector. One of the known spintronics systems is the giant magnetoresistance (GMR) device [1]. A typical GMR device consists of two ferromagnetic layers separated by a metallic nonmagnetic spacer layer. When the magnetization direction of two ferromagnetic layers is aligned the resistance will be smaller than that for antialigned layers. A similar idea uses tunnel magnetoresistance (TMR) devices[2]. In this case the spacer layer is made out of an insulating material and the magnetization vector alignment/antialignment will change the tunneling resistance. Such devices found common use as read heads of modern hard drives. Ultimate performance of such devices is determined by lifetimes of spin-polarized charge carriers, thus attracting a lot of attention to the electronic structure and the dynamic properties of strongly correlated systems like *3d*-ferromagnets, transition metal oxides and *4f-* rare-earths systems.

One of the promising candidates for spintronics application such as spin valves, spin injectors or magnetic tunnel junctions are half metallic ferromagnets (HMFs). Half metallic ferromagnets constitute a unique class of materials in which one of the spin bands has a metallic character, while the other one shows insulating or semiconducting behavior[3].Among proposed HMFs, Heusler alloys hold the greatest potential to provide half-metallicity at room temperature. Heusler alloys are usually categorized in two groups: alloys with a XYZ composition, crystallizing in the $C1_b$ structure and X_2YZ alloys crystal-

lizing in the structure L2$_1$. L2$_1$ Heusler alloys in an itinerant 2-1-1 compound mostly consist of two transition metals (X$_2$, Y) and one main group (Z) element crystallizing in the L2$_1$ structure. The sketch of the structure is shown in figure 1.1b. Kübler *et al* [4] recognized that the minority-spin state densities at the Fermi energy nearly vanish in the Heusler compounds Co$_2$MnAl and Co$_2$MnSn. The Heusler compound Co$_2$FeSi has attracted particular interest because it is predicted to have a large minority-spin band gap of about 1 eV (see figure 1.1a)[5, 6] and, with T$_C$ = 1100K [7, 8], it has one of the highest Curie temperatures among the known Heusler compounds. Bulk Co$_2$FeSi has been stabilized in the L2$_1$ structure with a saturation magnetization of 6μ_B per unit cell at 5K [7, 8]. Thin films of Co$_2$FeSi have been successfully used for fabrication of magnetic tunnel junctions [9]. The tunnel magneto-resistance (TMR) ratios of 60% at low temperature and 41% at room temperature suggest that still an improvement in the materials is necessary for successful use in devices, in particular with respect to their temperature behaviour. In particular, the magnetic moment of the thin films is with 3.9 - 4.9μ_B still much lower than in bulk samples [10].
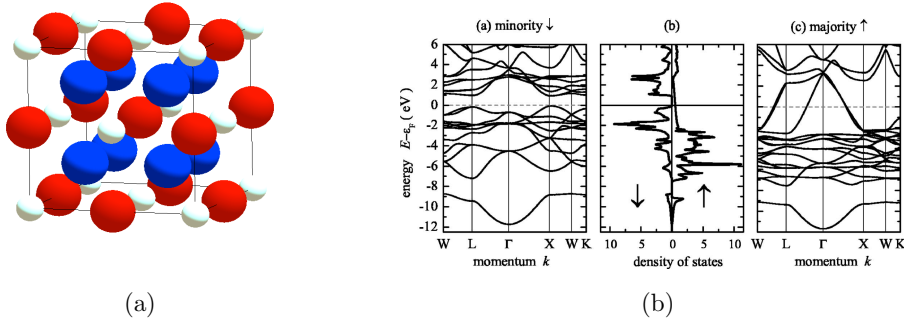

Figure 1.1: (a) Sketch of the Co$_2$FeSi crystal. Blue balls correspond to cobalt atoms, red to iron and white to silicon. (b) Calculated electronic structure taken from reference [8].

Another important issue for spintronics applications is the lifetime of the spin polarized carriers. The ultimate performance of spintronics devices is determined by the lifetimes of spin-polarized charge carriers, thus attracting a lot of attention to the electronic structure and the dynamic properties of strongly correlated electron systems like *3d*-ferromagnets, transition metal oxides and *4f-* rare-earths systems.

One of the fundamental consequences of electron correlation effects is that the bare particles in solids become 'dressed' with the excitation cloud result-

ing in quasiparticles. Such a quasiparticle will carry the same spin and charge as the original particle, but will have a renormalized mass and a finite lifetime. The properties of many-body interactions are described with a complex function, the called self energy $\Sigma = \mathrm{Re}\,\Sigma + \mathrm{Im}\,\Sigma$. The real part of the self energy $\mathrm{Re}\,\Sigma$ depicts the change of the band dispersion or the increase of the effective quasiparticle mass. The imaginary part of the self energy $\mathrm{Im}\,\Sigma$ contains the information about the lifetime of the quasiparticle. In case of electron scattering processes due to electron-electron, electron-phonon or electron-impurity interactions their contribution to the lifetime broadening, Γ, is independent of each other and can be expressed as a sum of each contribution: $\Gamma = \Gamma_{el-el} + \Gamma_{el-ph} + \Gamma_{el-imp}$ [11]. Γ_{el-imp} represents an energy-independent term arising from the electron-impurity scattering, while Γ_{el-el} and Γ_{el-ph}, which are contributions from electron-electron and electron-phonon scattering respectively, are energy dependent. For *3d*-metals Γ_{el-el} is well described at low energies by a Fermi liquid behavior and depends quadratically on the quasiparticle binding energy. In case of electron-phonon interaction the energy dependence of lifetime broadening is more complicated and will lead to the appearance of a kink – a sudden change in the dispersion below a finite binding energy.

Although the theoretical description of the electron scattering processes exists, the influence and the roles that these processes play in device performance are still open questions. Hence a better understanding of the electronic interactions is imperative, starting with a model system such as Ni bulk material that should be conceptually simpler and thus easier to explain.

The present work is structured as follows. Chapter 2 holds a general description of solids with emphasis on their electronic structure and the possible interactions that can happen upon photoionization. The theoretical formalism needed for the corresponding data evaluation is also introduced. A theoretical background of the employed data acquisition techniques that were used to investigate the Heusler alloys and the Ni(111) thin films is presented in chapter 3. The following chapter 4 concentrates on the comissioning results of the photoelectron microscope (SPEEM) and on the PEEM investigations of the Heusler alloys. Angle-resolved photoemission spectroscopy (ARPES) investigations on Ni thin films following the photohole lifetime effects are presented and evaluated in chapter 5. A thorough ARPES data analysis procedures as well as data modelling are also introduced. The summary of the thesis is given in chapter 6.

Chapter 2

Many body interactions and electronic structure of solids

2.1 Electronic structure of solids

In solid-state physics, the electronic band structure of a solid describes ranges of energy that an electron has. When a large number of atoms are brought together to form a solid, the number of orbitals becomes exceedingly large, so the levels form continuous bands of energy rather than the discrete energy levels of the atoms in isolation (figure 2.1). However, some intervals of energy contain no orbitals forming band gaps. Bands have different widths, based upon the properties of the atomic orbitals from which they arise. The electrons in the outermost shells of the isolated atom are the ones that interact strongly with similar electrons in neighboring atoms and these are called valence electrons. The remaining electrons of the atom are tightly bound to the nucleus, their wavefunctions (orbitals) do not extend far from the position of the nucleus and they are very little afected when the atom is surrounded by its neighbors in the solid. These are called the core electrons. Figure 2.2 shows a simplified picture of the bands in a solid that allows the three major types of materials to be identified: metals, semiconductors and insulators.

2.2 Magnetic solids

In physics, magnetism is one of the phenomena by which materials exert attractive or repulsive forces on other materials. Some well-known materials that exhibit easily detectable magnetic properties (called ferromagnets) are nickel, iron, cobalt, gadolinium and their alloys; however, all materials are influenced
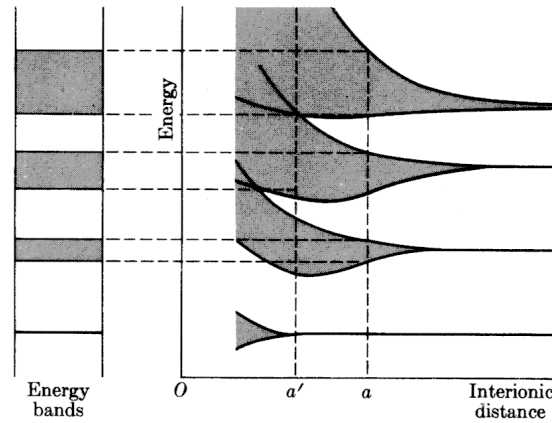
Figure 2.1: Electronic states in a solid built starting from isolated atoms at distance $a = \infty$: as the atoms move closer, the individual atomic levels spread out in bands, which then start to overlap, when the lattice separation a becomes comparable to the extension of the atomic wave functions.
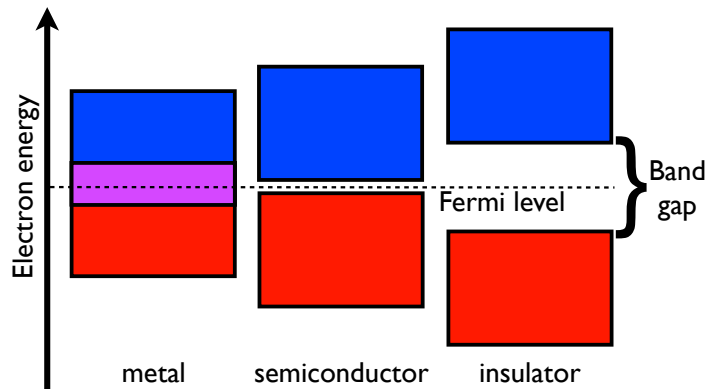

Figure 2.2: Diagram of the electronic band structure of metals, semiconductors, and insulators.

to greater or lesser degree by the presence of a magnetic field.

Magnetic materials can be classified in terms of the arrangements of magnetic dipoles in the solid. Materials with no elementary magnetic dipoles at
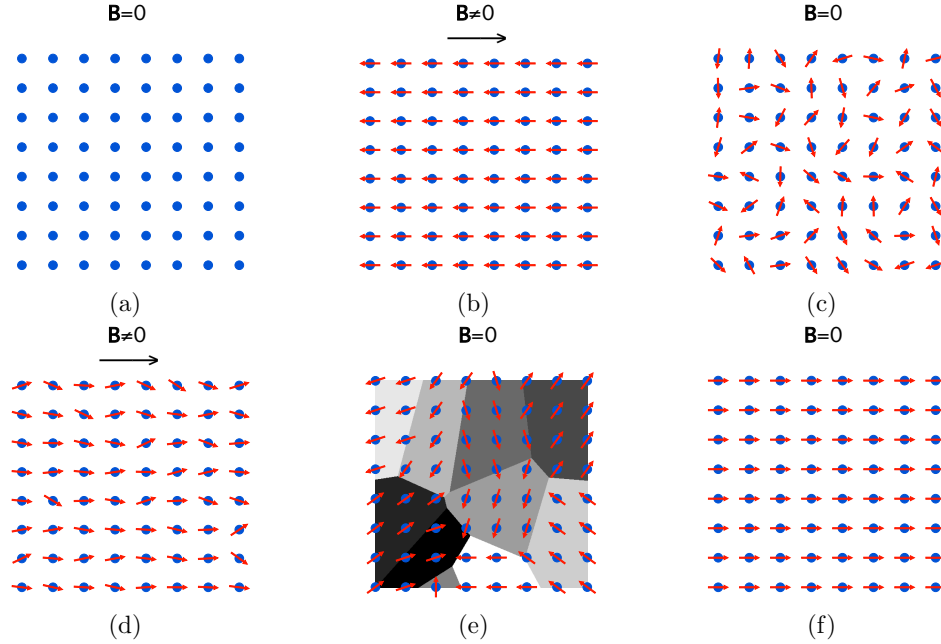

Figure 2.3: The effect of an applied magnetic field, **H**, or induction, **B**, on a solid. (a) A diamagnetic material has no dipoles present in the absence of magnetic induction; (b) weak dipoles are induced that oppose the field to give a weak repulsion. (c) In a paramagnetic material magnetic moments are present in the absence of magnetic field and oriented randomly; (d) in a field magnetic moments are aligned along the field. (e) In a ferromagnetic material magnetic moments align parallel to each other over a distance, creating magnetic domains (shown on the background in grayscale); (f) in the magnetic field all domains are aligning and this alignment remains after field removal.

all are diamagnetic (figures 2.3a and 2.3b). Application of a magnetic induction generates weak magnetic dipoles that oppose the applied induction. The magnetic susceptibility, χ, of a diamagnetic substance is negative. There is no appreciable variation of diamagnetism with temperature. Paramagnetic solids are those in which some of the atoms, ions or molecules making up the solid possess a permanent magnetic dipole moment. These dipoles are isolated from one another. In the absence of a magnetic field, these are arranged at random and the solid shows no net magnetic moment. In a magnetic field, the elementary dipoles will attempt to orient themselves parallel to the magnetic induction in the solid, and this will enhance the internal field within the solid and give rise to the observed paramagnetic effect (figures 2.3c and 2.3d). The

alignment of dipoles will not usually be complete, because of thermal effects and interaction with the surrounding atoms in the structure. The magnetic effect is much greater than diamagnetism, and the magnetic susceptibility, χ, of a paramagnetic solid is positive. Ferromagnetic materials are those in which the magnetic moments align parallel to each other over considerable distances in the solid (figure 2.3e). In magnetic field magnetic moments of different domains are aligned. This alignment remains after removal of the external field (figure 2.3f). An intense external magnetic field can be produced by this alignment. Ferromagnetism is associated with the transition elements, with unpaired d electrons, and the lanthanides and actinides with unpaired f electrons.

2.3   Exchange interaction

When speaking about solids, we can distinguish between two different types of magnetism, itinerant and localized, corresponding to the nature of the participating electrons. The localized states are well described by the atomic theory, including Hund's rules [12], with corrections due to the influence of the crystal fields. The itinerant magnetism is caused by the exchange interaction between valence electrons. This interaction originates from the Pauli exclusion principle [13] and favors spin polarization. On the other hand, hybridization, which causes band formation, favors a paramagnetic ground state. Therefore it is the competition between the exchange interaction and hybridization which will decide whether a particular system will exhibit itinerant magnetism or not.

One simple but useful model for itinerant magnetism is the Stoner model [14]. A finite magnetization $M \neq 0$, induces a magnetic field H. The eigenvalues of the kinetic energy ε_{nk} for a single spin in this field H are shifted by an amount of

$$\varepsilon_{nk}^{\pm} = \varepsilon_{nk} \mp \mu_0 \mu_B H \tag{2.1}$$

The total density of states is divided now in spin up and spin down densities defined as

$$D^{\pm} = D_0(\varepsilon \mp \mu_0 \mu_B H) \tag{2.2}$$
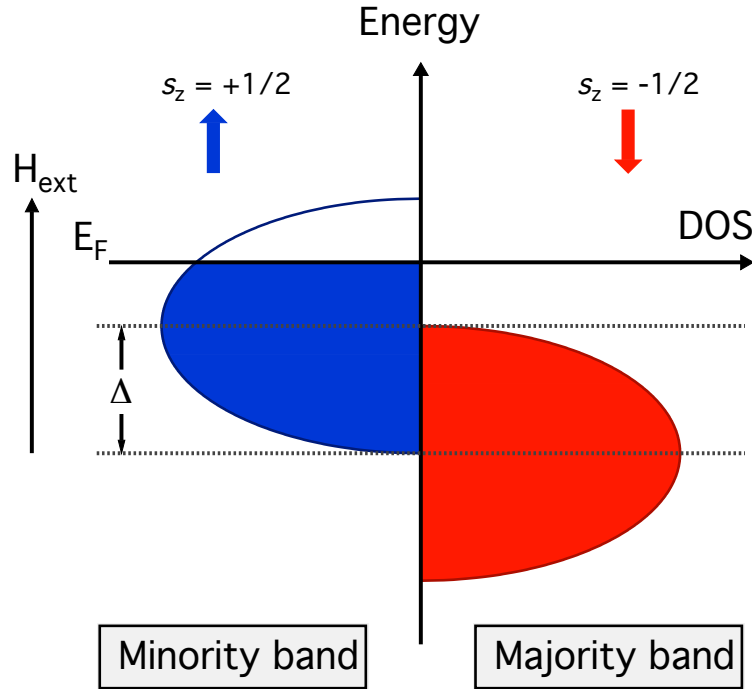
The magnetization can be written as

Figure 2.4: The Stoner model of ferromagnetic transition metals, illustrated for the 3d shell, and nomenclature used for the band description of magnetism. Filled electron states below the Fermi energy E$_F$ are shown shaded, hole states above E_F are shown unshaded. The spin states with the largest number of electrons are called "majority spins" and the corresponding band is the "majority band", and the term "minority" is used for the other electron spins and band. The centers of the majority and minority d bands, assumed to be reasonably localized as shown, are separated by the exchange splitting Δ. The labels "spin-up" and "spin-down" only have a meaning in conjunction with a quantization direction, which in our case is taken to be the direction of the external field H_{ext}. It is good to remember that the minority spins always point in the magnetization direction.

$$M = \int^{\varepsilon_F} \left(D^+(\varepsilon) - D^-(\varepsilon) \right) d\varepsilon \qquad (2.3)$$

For taking into account the exchange correlation contribution to the total energy, an extra term is added

$$E^{FM} = \int^{\varepsilon_F} \left(D^+(\varepsilon) + D^-(\varepsilon) \right) \varepsilon d\varepsilon - \frac{IM^2}{2}, \qquad (2.4)$$

where I is the Stoner exchange integral. For small magnetizations, equations 2.3 and 2.4 can be evaluated retaining only the first significant terms in M. It can be easily proven that the condition for ferromagnetism $E^{FM} < E^{PM}$ is equivalent to the Stoner criteria

$$ID(\varepsilon_F) > 1 \qquad (2.5)$$

The Stoner criteria correctly predicts that some of the $3d$ transition metals have magnetic ordering while none exists in the $4d$ and $5d$ series [15].

The magnetic behavior of itinerant and localized states is different. When localized moments couple, they create a macroscopic total magnetic moment. As the temperature increases, the ordering weakens and above the ordering temperature T_c, the total magnetic moments are completely disordered, but they retain their original magnitude. On the contrary, the itinerant moments disappear completely as the temperature rises above T_c (e.g. the collapse of exchange splitting in Ni). Because itinerant magnetization is influenced by the exchange interaction, the moment is strongly volume dependent. Unlike itinerant moments, localized moments show a very weak dependence on volume. A good example of localized moments are the rare earth systems. Here the $4f$ electrons are localized with the possible exception of Ce, that is, the $4f$ electrons retain their atomic character. If we allow the $4f$ electrons to form bands, these bands will be very narrow and local density approximations (LDA) will in general overestimate the bonding. $4f$ spin moments are correlated to each other by means of interaction with valence s, p or d electrons. At the same time, the $4f$ electrons polarizes the valence band which gives rise to small itinerant moments.

In rare earth – transition metal systems like GdFe$_2$ the situation is more complex. In these inter-metallic systems $4f$ spins are antiparallel to the transition metal $3d$ spins. The glue that pastes together $3d$ and $4f$ moments and brings out a ferrimagnetic spin alignment between these subsystems is the inter-atomic $3d$-$5d$ coupling, which can be as large as $0.6eV$.

2.4 Concept of the self energy

Electrons in a solid form bands due to interaction with the ion lattice and other electrons. Within a band the electron energy and the wave vector are not an independent values, but connected by dispersion relations.

As one of the fundamental consequences of electron correlation effects, bare particles in solids become 'dressed' with the excitation cloud resulting in quasiparticles (figure 2.5). Such a quasiparticle will carry the same spin and charge

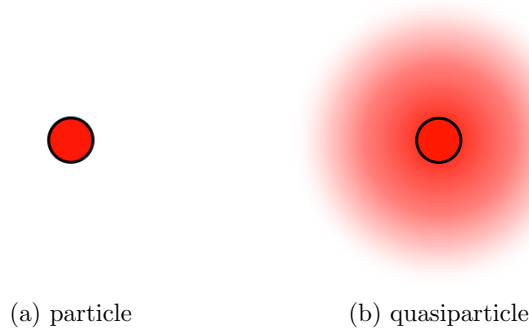(a) particle   (b) quasiparticle

Figure 2.5: (a) a particle and (b) a quasiparticle dressed in the excitation cloud.

as the original particle, but will have a renormalized mass and a finite lifetime. For the simple case of the plane wave, the wave function of a quasiparticle can be expressed as

$$\Phi(\tau) \approx exp\left(-i\tau\left(\frac{E - E_F}{\hbar} + i\Gamma\right)\right),\qquad(2.6)$$

where Γ is a damping term, having the meaning of lifetime. In case of zero damping ($\Gamma = 0$, see figure 2.6a) we obtain continuous oscillations described by a usual plane wave. If the damping term is small enough ($\Gamma \ll \frac{E - E_f}{\hbar}$, see figure 2.6b) the oscillations are still present, but their amplitude is decreasing with time. Such conditions describe the quasiparticle. However, when the dumping term is big $\Gamma \geq \frac{E - E_f}{\hbar}$, (see figure 2.6c) then there are no more oscillations present, ending in a situation where no quasiparticle is appearing.

The interaction between an electron and a solid is described by a complex function called self energy.

$$\Sigma = \text{Re}\,\Sigma + i\,\text{Im}\,\Sigma\qquad(2.7)$$

The real part of the self energy $\text{Re}\,\Sigma$ depicts the change of the dispersion or the increase of the effective mass, while the imaginary part of the self energy $\text{Im}\,\Sigma$

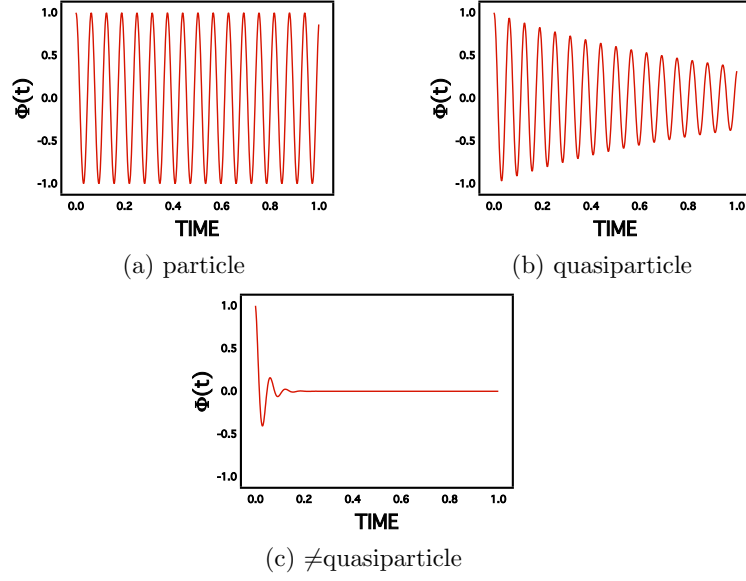(a) particle

(b) quasiparticle

(c) ≠quasiparticle

Figure 2.6: Change of the wave function in time for *(a)* a particle, *(b)* a quasiparticle and *(c)* a non-quasiparticle

contains the information about the lifetime of the quasiparticle. An example of the band structure in presence of correlation effects is shown in figure 2.7

The widths of the band can be interpreted using the Heisenberg uncertainty principle. If we consider a cut through the band plot at a fixed momentum that is an energy distribution curve (EDC) then we can obtain an energy width, δE. Using the uncertainty principle 2.8

$$\delta\tau\delta E \geq \hbar \tag{2.8}$$

this width will have the meaning of lifetime ($\delta\tau$). In case of a cut through the band at fixed energy thus obtaning a momentum distribution curve (MDC), we operate with the width in momentum direction δk. Taking into account that $p = \hbar k$ we can write the uncertainty equation as 2.9

$$\delta x\delta k \geq 1 \tag{2.9}$$

From which the width in k gains the meaning of mean free path.

The real and imaginary parts of the self energy are not independent but connected by the Kramers-Kronig relations [16].
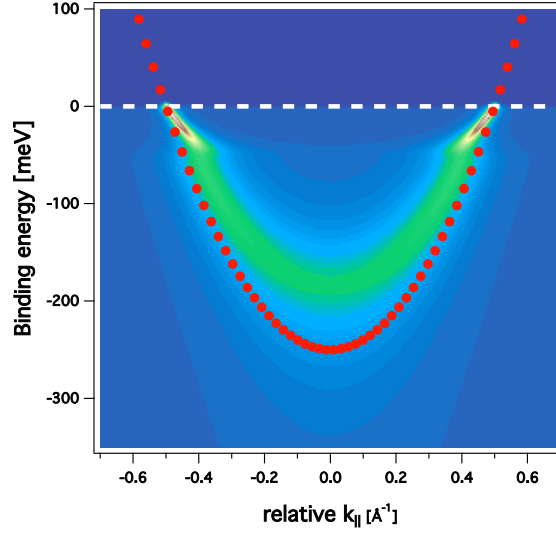
Figure 2.7: Model of a band structure with interactions on. Red dots denote
the bare particle dispersion.

2.5 Electron-electron interaction

As already mentioned in the photoemission process an electron is ejected and
a photohole is created. After a certain time the photohole will decay. In
the decay process based on the conservation laws, the energy, momentum and
spin will have to be preserved. This will lead to several different decay paths.
In this paragraph we will refer to one of them namely the electron-electron
interaction, which is also known as the three body scattering. This process is
actually an Auger decay of the photohole, since the energy from the electron
that fills the photohole is used to create an electron-hole pair (figure 2.8a).

In many cases the electron-electron contribution can by described by a
Fermi liquid. Then for energies in the vicinity of the Fermi level one obtains
the following expression for temperature and energy dependent self energy:

$$\Sigma^{El-El}(E,T) = \alpha E + i\beta \left[E^2 + (\pi k_B T)^2 \right],
\tag{2.10}$$

where β is the electron-electron coupling constant. The corresponding change
in a band dispersion is depicted in figure 2.8b.

While electron-electron scattering will play the dominant role at higher
binding energies, energy dependence next to Fermi level will be mostly deter-
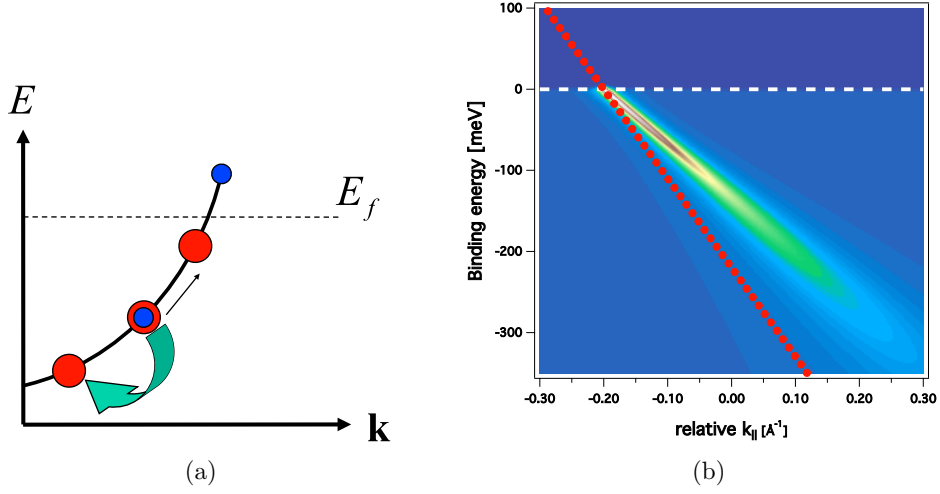mined by electron-phonon and/or electron-magnon scattering.

Figure 2.8: Electron-electron interaction. (a) Decay scheme for the electron-electron interaction. The photohole (red circle) is filled with an electron (blue circle) creating electron-hole pair. (b) Model of the linear band with the electron-electron interaction enabled. Red circles denote the bare particle dispersion.

2.6 Electron-phonon interaction

Another decay path of the photohole is phonon emission. At the beginning let us consider what would happen with the photohole if the sample would be at 0 K temperature. One of the decay ways is filling the photohole with an electron from a higher energy level and thus emitting a phonon to preserve energy and momentum. The process is sketched in figure 2.9.

In the simplest model, proposed by Einstein [17] we assume the boson as an oscillator with only one frequency (energy) Ω_0. In case of a bosonic interaction the situation will be the following. If the energy of the photohole is smaller than the mode energy $E^{hole} < \Omega_0$, then the photohole cannot decay and will have infinite lifetime or $\operatorname{Im}\Sigma = 0$. If the energy of the photohole is equal or more than the mode energy $E^{hole} \geq \Omega_0$, then it can decay into this mode having a finite life time or $\operatorname{Im}\Sigma \neq 0$. For the dispersion this will mean that in the first case the photohole will be dressed in virtual excitations leading to enhancement of the effective mass resulting in an increase in the real part of self energy. This change of the effective mass will lead to the appearance of a kink which is a sudden change in the dispersion below a finite binding energy. An example for the real and imaginary part of the self energy in case of the Einstein model is shown in figures 2.10a and 2.10b. The model band dispersion simulated for electron-boson interaction with the kink visible is shown in figure
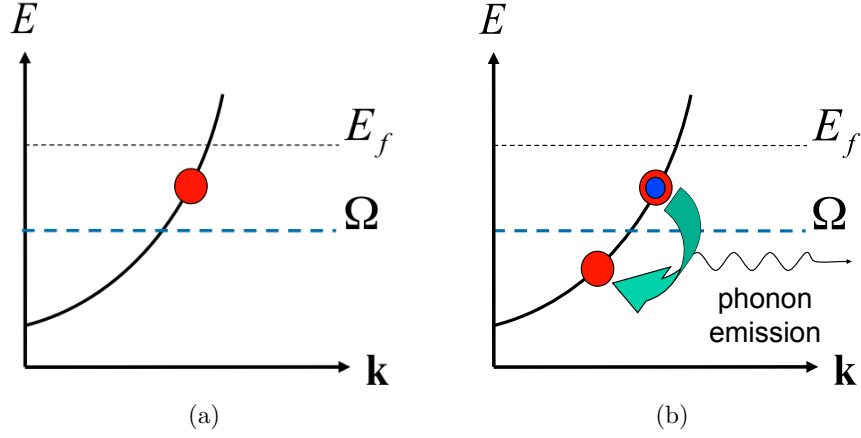
26

(a) (b)

Figure 2.9: Phonon emission at zero temperature in Einstein model. (a) If the
energy of the photohole (shown as a red circle) is smaller then the mode energy
$E^{hole} < \Omega_0$, then no phonon can be emitted. If the energy of the photohole is
equal or more then the mode energy $E^{hole} \geq \Omega_0$, then it can decay into this
mode giving a finite life time or $\mathrm{Im}\,\Sigma \neq 0$.

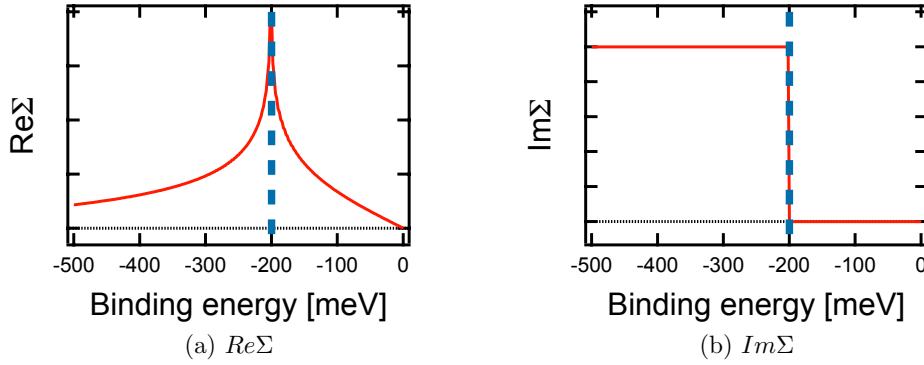2.11.

(a) $Re\Sigma$ (b) $Im\Sigma$

Figure 2.10: Examples of the (a) real and (b) imaginary part of self energy in
the case of Einstein model and 0 K temperature. The mode energy is denoted
with a blue dashed line.

One of the important parameters of bosonic interactions is the coupling
constant or the mass enhancement factor *lambda*. It is defined as a change of
the group velocity

$$v_k = \frac{1}{\hbar}\frac{\partial E}{\partial k} \tag{2.11}$$

by the factor of $\frac{1}{1+\lambda}$ of the Fermi energy. Or, in terms of effective mass this
could be written as

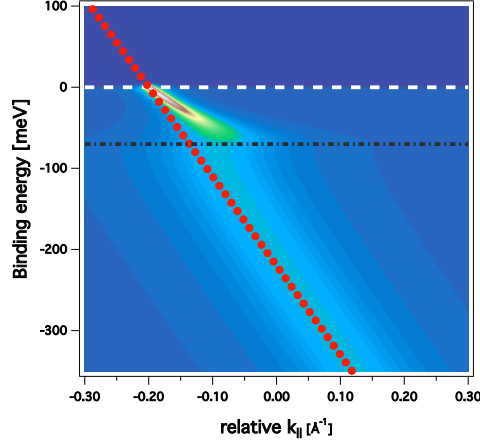$$m^{eff} = (1+\lambda)m \tag{2.12}$$

27

Figure 2.11: Model band dispersion with electron-phonon interaction. Red dots show the bare dispersion. The black dot-dashed line denotes the Debay energy.

In the case of T=0 K, lambda can be obtained from the real part of the self energy as

$$\lambda = \frac{d\operatorname{Re}\Sigma}{dE}\bigg|_{E=E_F} \tag{2.13}$$

The central property that describes the electron-bosonic interaction is the Eliashberg function $\alpha^2 F(E)$, which consists of the density of states $F(E)$ and the coupling between a boson and an electron expressed as $\alpha^2 F(E)$ [18]. The Eliashberg function is related to the coupling constant λ in the following way: at $T = 0K$ the coupling parameter is equal to the first momentum of the Eliashberg function:

$$\lambda = \int\limits_{0}^{\infty} \frac{\alpha^2 F}{\hbar\omega} d\hbar\omega \Bigg|_{T=0\ K} \tag{2.14}$$

The imaginary part of the self energy can be expressed as

$$\operatorname{Im}\Sigma^{el-ph} = 2\pi \int\limits_{0}^{\hbar\Omega_{max}} \alpha^2 F_k\left(E'\right)\left[2n\left(E'\right) + f\left(E' + E\right) + f\left(E' - E\right)\right], \tag{2.15}$$

where $f(E)$ is the Fermi-Dirac function, $n(E)$ is the Bose-Einstein distribution and $\alpha^2 F_k$ is the Eliashberg function.

A more realistic model that describes the phonon density of states is the Debye model. In this model it is considered that the dispersion of the phonon modes is linear $\hbar\omega \propto |\mathbf{k}|$ in all three dimensions [11], and one assumes that only the longitudinal modes interact with the electrons with $\alpha(\omega) = const.$
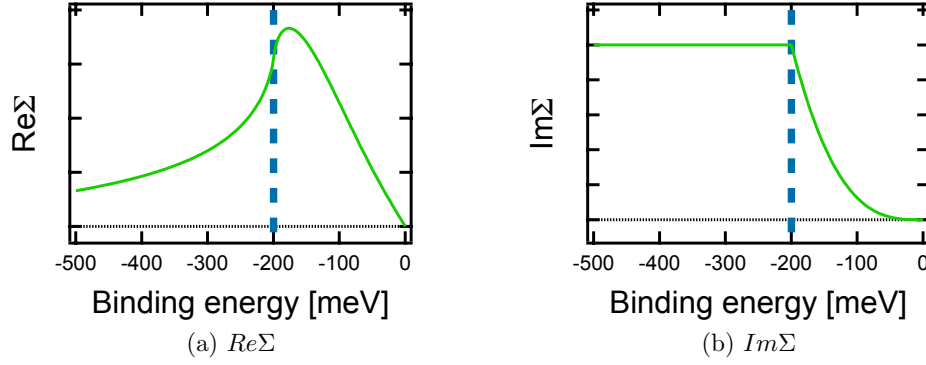
(a) $Re\Sigma$ (b) $Im\Sigma$

Figure 2.12: Examples of the (a) real and (b) imaginary part of the self energy in the case of Debye model and 0 K temperature. The cut off energy is denoted with a blue dashed line.

Thus, the Eliashberg function is proportional to the density of phonon levels and is simply given by

$$\alpha^2 F(E) = \begin{cases} \lambda \left(\dfrac{E}{\hbar \omega_D} \right)^2 & \text{for } E \leq \hbar \omega_D \\ 0 & \text{for } E > \hbar \omega_D \end{cases}, \tag{2.16}$$

where λ is the electron-phonon coupling constant and $\hbar \omega_D$ is the Debye energy. The resulting real and imaginary parts of the self energy are shown in figures 2.12a and 2.12b.

2.7 Electron-boson interaction in magnetic solid

In a magnetic solid the decay processes of a photohole can follow two paths, namely through the emission of either a phonon or a magnon. Since the phonon carries zero spin, the transitions associated with the photohole decay can only occur within the same band (figure 2.13a). This process does not depend on the spin character of a band and can happen both in minority and majority bands. In the case of decay by magnon emission in order to preserve the spin a spin-flip process must happen. Thus the photohole will be filled with an electron from a band with opposite spin orientation. (figure 2.13b). This type of transitions at $T = 0$ K temperature can only take place when the photohole in the minority band is filled by an electron from the majority band. Opposite spin flip process is not possible due to the fact that the system has a saturated magnetization.

(a) Phonon emission process.
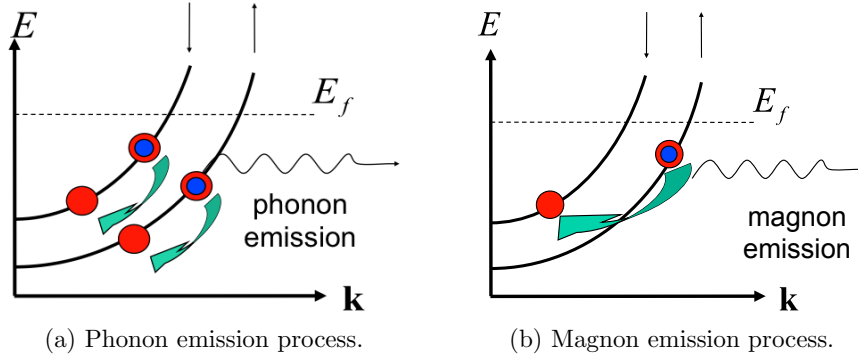
(b) Magnon emission process.

Figure 2.13: Bosonic models at low temperature. (a) phonon carries zero spin, therefore transitions could occur only within a band with the same spin character. (b) magnon have integer spin, therefore spin-flip takes place.

At non zero temperature both absorption and emission magnons can occur for both majority and minority bands, but the minority spin band will always have have higher density of states to scatter into.

Chapter 3

Experimental methods of investigating the electronic structure of solids

One of the fundamental interactions of x-rays with matter is photoelectric absorption. The effect was discovered in year 1887 by H. Herz [19]. It was unexplained untill Albert Einstein succeeded to explain the photovoltaic effect by the quantum nature of light in the year 1905 [20]. Today the photovoltaic effect is the base for many modern experimental methods to study the electronic structure of solids. The experimental methods utilizing the photoelectric effect can be divided in two main categories. The first one uses fixed photon energy and measures the energy distribution of emitted electrons or photons. This idea is exploited in a variety of photoelectron spectroscopies like X-ray Photoemission spectroscopy (XPS), Angle-Resolved Photoemission Spectroscopy (ARPES) and so on. The second group of methods measures absorption coefficient as a function of photon energy, e.g. Near Edge X-ray Absorption Fine Structure spectroscopy (NEXAFS), Extended X-ray absorption fine structure (EXAFS), etc.

3.1 X-Ray Photoelectron Spectroscopy

Twenty years after the discovery of the photoelectric effect, P.D. Innes [21] recorded emitted electrons as function of electron velocity, in fact obtaining the first XPS spectrum. After the development in mid-50es of the high resolution spectrometer by Kai Siegbahn and co-workers [22] the goal of XPS as method to investigate electronic structure was achieved.

The description of the photoemission process is quite simple. When a solid is illuminated with light photoexcitations of electrons can occur. If the energy of the excited electron is high enough to overcome a surface potential Φ, then it could escape the solid. Φ is usually denoted as work function and has a value of few eV.

3.1.1 General considerations

An equation binding photon energy $h\nu$ and kinetic energy of electrons is

$$E_{kin} = h\nu - E_B - \Phi, \tag{3.1}$$

where E_{kin} is the kinetic energy of emitted electrons and E_B is their binding energy. This equation can be used to determine the binding energy of the electrons. A sketch of the photoemission process is shown in figure 3.1 for both cases of emission of electrons from core levels and valence band. In the case of valence band the typical binding energy of electrons is several electron volts, while for core levels it could go up to several thousands of eV.
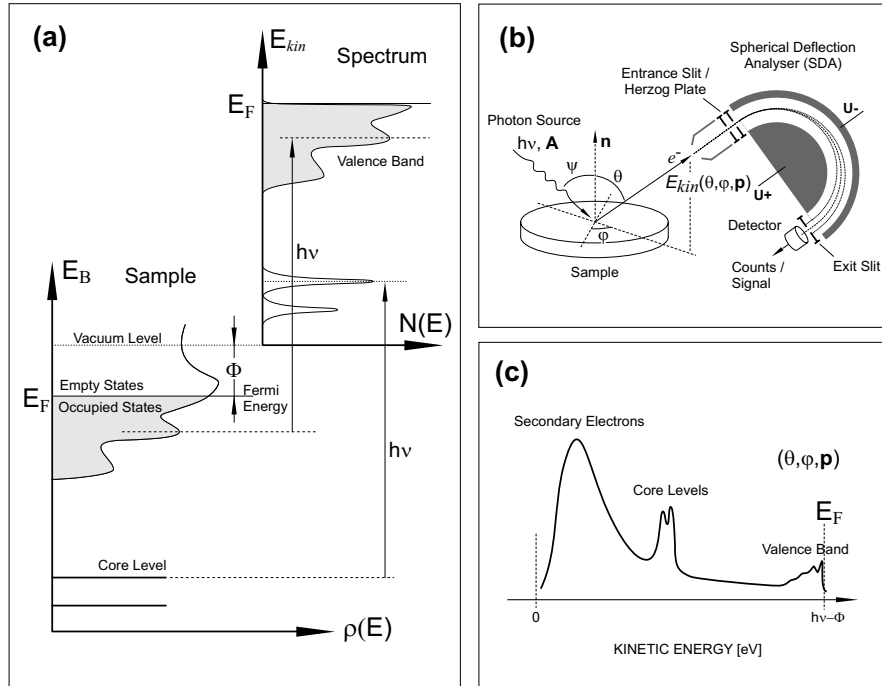

Figure 3.1: (a) energy diagram illustrating the photoexcitations with monochromatized light for core levels and valence band; (b) scheme of photoemission experiment; (c) shape of detected photoelectron spectrum.

The photoemission process is often described in the framework of the so

called *three step model* [16]. In this case photoemission is decomposed into
three different steps and each of them are treated independently. In the first
step the photoexitation itself is happening. It has to be considered in the
framework of quantum mechanics, namely by the single particle approximation
[16]. In this case the photocurrent produced in the XPS experiment results
from excitations of electrons from an initial state $|\psi_i>$ to a final state $<\psi_f|$.
The transition probability in this case can by calculated by *Fermi's Golden
Rule*:

$$w \sim \frac{2\pi}{\hbar} |<\psi_f|H'|\psi_i>|^2 \delta\left(E_f - E_i - h\nu\right), \qquad (3.2)$$

where δ function is responsible for the energy conservation and H' describes the
interaction in between the electron and the vector potential $\mathbf{A}$ of the photon.
Within the dipole approximation $\mathbf{A}$ is considered constant. Then H' can be
written as

$$H' = \frac{e}{2mc}\mathbf{A} \cdot \mathbf{p}. \qquad (3.3)$$

Inserting 3.3 into eq. 3.2 and taking into account the ordinary Hamiltonian
of the electron $H = \frac{p^2}{2m} + V(\mathbf{r})$ [12] one gains two forms of the matrix element:

$$<\psi_i|\mathbf{p}|\psi_f> = im\omega <\psi_i|\mathbf{r}|\psi_f> = \frac{i}{\omega} <\psi_i|\nabla V|\psi_f> \qquad (3.4)$$

The second stage of the three step model is the transport of the electron to
the surface. The electron escape depth is limited by inelastic scattering. The
amount of electrons that could reach the surface and escape to vacuum from
depth d is:

$$N = N_0 \exp -\frac{d}{\lambda}, \qquad (3.5)$$

where λ is the inelastic mean free path and N is the amount of emitted pho-
toelectrons. λ depends on the kinetic energy of electrons and has a line shape
shown in the figure 3.2

The last stage is the escape of the electron into vacuum. In order to do it
the electron has to overcome the surface potential barrier.

The momentum vector of the electron can be written as $\mathbf{k}^{int} = \mathbf{k}_{\parallel}^{int} + \mathbf{k}_{\perp}^{int}$
(see figure 3.3), where $\mathbf{k}_{\parallel}^{int}$ denotes the projection parallel and $\mathbf{k}_{\perp}^{int}$ perpendic-
ular to the surface [23].

The transmission of the electron over the surface leaves $\mathbf{k}_{\parallel}^{int}$ conserved.
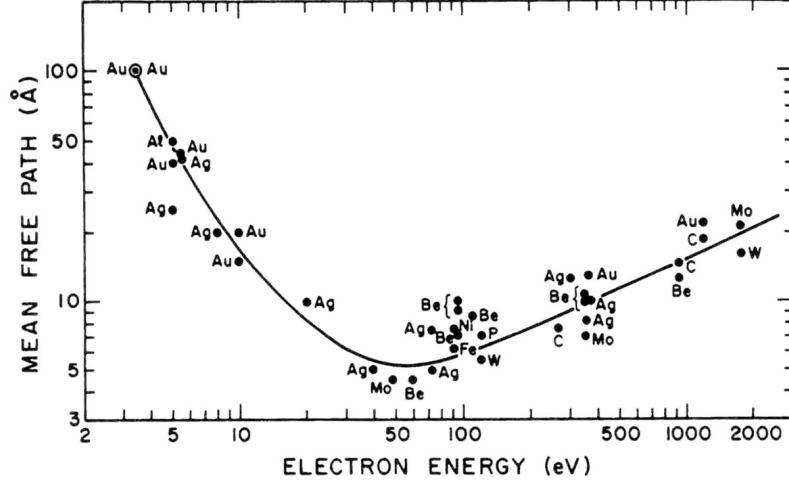
Figure 3.2: The inelastic mean free path of electrons - the so called "Universal curve" [13]

However it could be translated by the reciprocal surface vector $\mathbf{G}$, i.e.

$$\mathbf{k}_{\parallel}^{ext} = \mathbf{k}_{\parallel}^{int} + \mathbf{G}_{\parallel}. \tag{3.6}$$

Taking into account that $E_{kin} = \frac{\mathbf{k}^2}{2m}$ and $|\mathbf{k}_{\parallel}| = |\mathbf{k}| \cdot \sin\theta$ equation 3.6 becomes:

$$|\mathbf{k}_{\parallel}^{ext}| = |\mathbf{k}_{\parallel}^{int}| = \sqrt{\frac{2m}{\hbar^2} E_{kin}} \cdot \sin\theta \tag{3.7}$$

This equation is important for the concept of angular-resolved photoemission. Collecting electrons under different emission angles one could map the band structure $E(\mathbf{k}_{\parallel})$.

The case of $\mathbf{k}_{\perp}$ is more complicated, since $\mathbf{k}_{\perp}$ is changed when the electron leaves the solid, so $\mathbf{k}_{\perp}^{ext}$ does not reflect the value of $\mathbf{k}_{\perp}^{int}$ directly. Thus $\mathbf{k}_{\perp}^{int}$ could be approximated by

$$\mathbf{k}_{\perp}^{int} = \sqrt{\mathbf{k}_{\perp}^{ext2} + \frac{2mV_0}{\hbar^2}} \tag{3.8}$$

where V_0 stands for the inner potential and it is an empirically adjustable parameter.
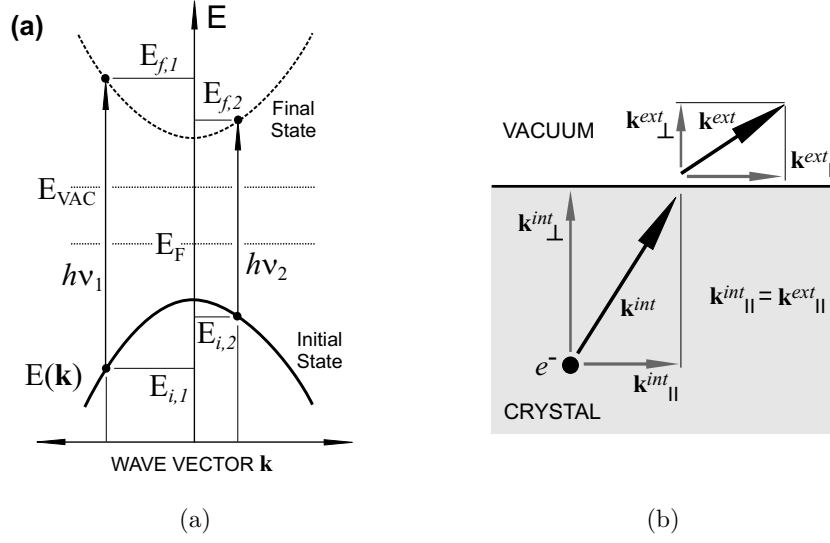
Figure 3.3: (a) momentum-energy diagram showing optical (direct) electron transitions for two different photon energies; (b) refraction of a photoelectron at the surface barrier upon escape from the crystal.

3.2 Angle-resolved photoemission spectroscopy

In the photoemission experiment both energy and momentum have to be preserved. The relations between the k-vectors and the angles are given by the following equations:

$$k_{||} = \sqrt{\frac{2m_e}{\hbar^2}} \sqrt{E_{kin} \sin^2 \theta} \tag{3.9}$$

$$k_{\perp} = \sqrt{\frac{2m_e}{\hbar^2}} \sqrt{E_{kin} \cos^2 \theta + V_0} \tag{3.10}$$

The intensity measured in the photoemission experiment is proportional to

$$I(E, \mathbf{k}) = M(E, \mathbf{k}) \times A(E, \mathbf{k}) \times f(E) \tag{3.11}$$

where $M(E, \mathbf{k})$ are matrix elements given by $\langle \psi_f | H_{PE} | \psi_i \rangle$, $A(E, \mathbf{k})$ is a spectral function and $f(E)$ is a Fermi-Dirac distribution. The spectral function $A(E, \mathbf{k})$ is related to the Green's function of the system by

$$A(E, \mathbf{k}) = \frac{1}{\pi} |\text{Im} \, G(E, \mathbf{k})|, \tag{3.12}$$

where

$$G(E, \mathbf{k}) = \frac{1}{E - E(\mathbf{k})}. \tag{3.13}$$

In the non-interacting electron case this yields

$$A^0(E, \mathbf{k}) = \frac{1}{\pi} \delta \left(E - E^0(\mathbf{k}) \right), \tag{3.14}$$

namely a δ - function at $E^0(\mathbf{k})$ (Koopmans' Theorem [24]), where $E^0(\mathbf{k})$ is the bare particle dispersion. In the interacting electron case one has to take the self energy Σ into account

$$E(\mathbf{k}) = E^0(\mathbf{k}) + \Sigma \tag{3.15}$$

With $\Sigma = \operatorname{Re} \Sigma + i \operatorname{Im} \Sigma$, this is leading to the final formula

$$A(E, \mathbf{k}) = \frac{1}{\pi} \frac{\operatorname{Im} \Sigma}{(E - E^0(k) - \operatorname{Re} \Sigma)^2 + \operatorname{Im} \Sigma^2} \tag{3.16}$$

3.2.1 Final state effects

The spectral function presented in the equation 3.16 is a spectral function of the photohole. But usually the contribution of the photoelectron final state has to be taken into account. While the exact treatment is quite complicated, an influence on the lifetime widths could be estimated, as found by [25].

If the contributions from photohole and photoelectron could be described as Lorentzians with linewidths of Γ_i and Γ_f respectively, then the resulting lifewidth $\Gamma^{measured}$ could be expressed as follows:

$$\Gamma^{measured} = \frac{\Gamma_i/|v_{i\perp}| + \Gamma_f/|v_{f\perp}|}{\left| \frac{1}{v_{i\perp}} \left(1 - \frac{m v_{i||} \sin^2 \theta}{\hbar k_{||}} \right) - \frac{1}{v_{f\perp}} \left(1 - \frac{m v_{f||} \sin^2 \theta}{\hbar k_{||}} \right) \right|} \tag{3.17}$$

where $v_{i\perp}$ is the initial state group velocity ($\hbar v_{i\perp} = \partial E / \partial k_{\perp}$), v_f is the final state velocity and θ is the angle between the measurement direction and sample normal. In case of normal emission ($\theta = 0$) and in case of $v_{i\perp} \ll v_{f\perp}$ expression 3.17 simplifies to

$$\Gamma^{measured} = \Gamma_i + \frac{|v_{i\perp}|}{|v_{f\perp}|} \Gamma_f \tag{3.18}$$

If the photoelectron is described as a free particle, then we could estimate the speed and the lifetime (broadening) of it. Using the Heisenberg uncertainty principle $\delta x \delta p \geq \hbar$ and taking into account that δx has the meaning of mean free path of the electrons (λ_{MFP}) we can write that

$$\lambda_{MFP} m_e \delta v_f \geq \hbar, \tag{3.19}$$

taking into account that $\delta E = m_e v_f \delta v_f$ this gives:

$$\Gamma_f \equiv \delta E = v_f \frac{\hbar}{\lambda_{MFP}} \tag{3.20}$$

Including this into equation 3.18 the final formula is given by

$$\Gamma^{measured} = \Gamma_i + v_i \frac{\hbar}{\lambda_{MFP}} \tag{3.21}$$

3.2.2 Photohole lifetime

The photohole lifetime can be expressed as a sum of different contributions as:

$$\Gamma^{photohole} = \Gamma^{el-el} + \Gamma^{el-ph} + \Gamma^{el-mg} + \Gamma^{el-imp} \tag{3.22}$$

where Γ^{el-el} is the electron-electron scattering contribution, Γ^{el-ph} electron-phonon, Γ^{el-mg} electron-magnon and Γ^{el-imp} impurity scattering, the latter usually taken as a constant and not dependent on the value of k vector or energy.

The measured lifetime will also have other contributions:

$$\Gamma^{measured} = \Gamma^{photohole} + \Gamma^{resolution} + \Gamma^{final}, \tag{3.23}$$

where $\Gamma^{resolution}$ is the contribution of the finite angular resolution of the experiment and Γ^{final} is the final state broadening.

3.2.3 Experimental resolution

The contribution of experimental resolution can be estimated in the following way. From equation 3.9

$$\delta k_{||} = \sqrt{\frac{2m_e}{\hbar^2}} \sqrt{E_{kinetic}} \cos \theta \delta \theta \tag{3.24}$$

and taking into account that $\mathrm{Im} \, \Sigma = \hbar v_F \delta k$, where v_F is the Fermi velocity then the contribution of the experimental resolution becomes

$$\Gamma^{resolution} \leq \sqrt{2m_e \hbar E_{kinetic}} v_F \delta \theta \tag{3.25}$$

3.3 X-ray absorption spectroscopy and magnetic dichroism

Probing changes of the x-ray absorption coefficient near core excitations as a function of the photon energy provides information about the electronic and magnetic states of the probed element. The use of the technique became possible with the development of synchrotron sources which can provide high brilliance soft x-ray with full polarization control and high resolution. Polarization control is especially important in the case of the study of magnetic properties, since the x-ray absorption coefficient for polarized x-rays depends of the magnetization vector.

3.3.1 Dipole transition

The X-ray absorption cross section σ of an atom is defined as the number of electrons exited per unit time divided by the amount of incident photons per unit time per unit area [26]

$$\sigma(E) = \frac{\Sigma_{i,f} P_{i \to f}}{I_{ph}} \qquad (3.26)$$

where $P_{i \to f}$ denotes the probability of transition from initial state $< i|$ into final state $|f>$ by the absorption of photon of energy $E = h\omega$. This probability is given by Fermi rule and can be written as:

$$P_{i \to f} = \frac{2\pi}{\hbar} |< f|H'|i >|^2 \delta\left(E_f - E_i - h\nu\right) \qquad (3.27)$$

where δ-function is responsible for energy conservation and H' is the perturbation hamiltonian. The δ - function represents the energy conservation; transitions are only possible if the energy interval between initial and final state corresponds to the energy of the absorbed photon. The electromagnetic field of the photons can be described by the vector potential $A(r,t) = A_0 \epsilon e^{i(ky-\omega t)}$ in terms of an electromagnetic plane wave. With the wave vector k, frequency ω and the polarization vector ϵ. ϵ^0 corresponds to linear and ϵ^{+1} (ϵ^{-1}) to right (left) circular polarized light with a polarization vector $\epsilon^{+1} = 1/\sqrt{2}(\epsilon_x + i\epsilon_y)$ ($\epsilon^{+1} = 1/\sqrt{2}(\epsilon_x + i\epsilon_y)$). Circular polarized photons carry an angular momentum which is parallel (antiparallel) to the wave vector k for left (right) circular polarization.
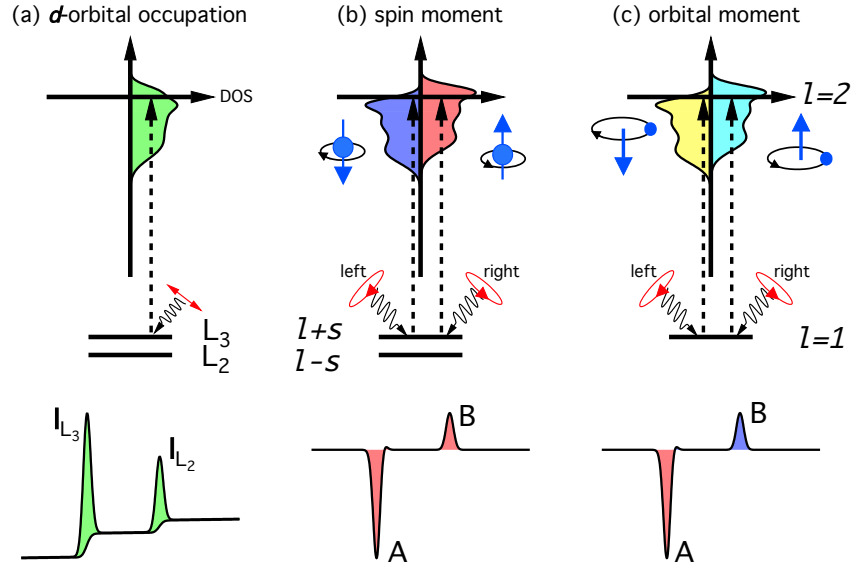
Figure 3.4: Electronic transitions in conventional L-edge x-ray absorption (a), and x-ray magnetic circular x-ray dichroism (b,c), illustrated in a one-electron model. The transitions occur from the spin-orbit split $2p$ core shell to empty conduction band states. In conventional x-ray absorption the total transition intensity of the two peaks is proportional to the number of d holes (first sum rule). By use of circularly polarized x-rays the spin moment (b) and orbital moment (c) can be determined from linear combinations of the dichroic difference intensities A and B, according to other sum rules.

3.3.2 Circular dichroism

The x-ray magnetic circular dichroism (XMCD) is defined as the difference in the absorption cross section between left and right circularly polarized x-ray light with the wave vector $\mathbf{k}$ parallel to the magnetization $\mathbf{M}$ (the x-ray helicity $\epsilon^\pm$ is collinear with the propagation direction)(see figure 3.4). This effect is analogue to the magneto optical Faraday effect in the soft x-ray regime. In 1845 Faraday discovered a rotation of the polarization vector of linearly polarized light upon the transmission through silicon borate in an applied magnetic field. Due to the exchange splitted valence states the absorption coefficient for the two circular components of the incident light is different. This effect also causes a rotation of the linear polarization into elliptically polarized light after the transmission.

The XMCD effect occurring at the L_3 and L_2 edge of 3d transition metals can be explained within a qualitative picture. The circular polarized photon gets absorbed generating a hole in the $2p$ shell. The p states are split into the

$2p_{3/2}$ and $2p_{1/2}$ level by the spin orbit interaction. This interaction couples the spin of the $2p$ electrons to the orbital moment. At the $2p_{3/2}$ and the $2p_{1/2}$ level the orbital angular momentum $\mathbf{l}$ and the spin angular momentum $\mathbf{s}$ are coupled parallel and antiparallel, respectively. The spin-orbit coupling allows to excite electrons of the $2p$ shell by circular polarized light spin selective into the valence shell even if the dipole operator does not act on the spin. The spin polarization arises from the selection rule for the orbital magnetic moment depending on the polarization of the absorbed x-ray photon. Because of the parallel coupling of $\mathbf{l}$ and $\mathbf{s}$ at the $2p_{3/2}$ level and the antiparallel at the $2p_{1/2}$ level, transitions from the $2p_{3/2}$ and the $2p_{1/2}$ levels into the valence shell occur with different spin polarization.

Possible final states for the photoexcitation are the unoccupied $3d$ and $4s$ states above the Fermi level. The dipole transition is spin conservative which means that a spin up electron can only be promoted in to a spin up empty state and vice versa. In a ferromagnetic transition metal there is an imbalance of unoccupied spin-up and spin-down states in the d-band due to the exchange coupling (Stoner model). If the orientation of the magnetization $\mathbf{M}$ is parallel to the photon wave vector $\mathbf{k}$ this imbalance of empty d-states leads to a spin selective excitation process, i.e. the probability of an electron transition excited by a circular polarized photon is proportional to the unoccupied d-states. It causes an asymmetry in the absorption cross sections for left and right circular polarized light which is proportional to the difference in the unoccupied spin-up and spin-down states, i.e. the spin magnetic moment. But the photoelectron also probes the orbital magnetic moment of the valence band. Due to the conservation of angular momentum the change in the quantum number m is determined by the polarization of the photon. Left circular polarized photons with the magnetic moment $+\hbar$ can cause only transitions with $\Delta m = 1$ and accordingly right circular polarized photons can cause only transitions with $\Delta m = -1$. If the valence states with quantum numbers $\pm m_l$ are unequally occupied the absorption of photons with opposite helicity will be different. An example of the XMCD effect is shown in figure 3.4b and 3.4c.

Chapter 4

Spin polarization near the Fermi edge in Heusler alloys

In this chapter we discuss the spin polarization near the Fermi edge in the Co_2FeSi Heusler alloy. This compound is a promising material for magneto-electronic devices. With a Curie temperature of 1100K, a saturation magnetization of 6 Bohr magnetons and a high spin polarization at the Fermi edge it fulfills the essential requirements for magnetic sensors or spin valve structures. An essential feature for such devices is the micro-magnetic domain structure. Using photoemission microscopy we directly observed the domain structure and performed spin resolved photoemission measurements within a single domain. Due to the complex chemical composition of the sample, cleaning procedures generally lead to a non stoichiometric sample composition. However small areas of the sample still preserve the nominal composition and thus the use of the photoelectron microscope becomes essential in this experiment. The experiment was performed using the SPEEM setup at the BESSY II storage ring.

The X_2YZ Heusler compounds [27, 28, 29, 30] are usually ternary 2-1-1 compounds. They consist mostly of two transition metals (X_2, Y) and one main group (Z) element crystallizing in the $L2_1$ structure. The sketch of the structure is shown in figure 4.1. They have attracted scientific and technological interest for their potential use as materials for magneto-electronic devices. The reason is the exceptional electronic structure found in many of those compounds, in particular the ones based on cobalt. Kübler *et al* [4] recognized that the minority-spin state densities at the Fermi energy nearly vanish in the Heusler compounds Co_2MnAl and Co_2MnSn. The authors concluded that this should lead to peculiar transport properties in these compounds because only
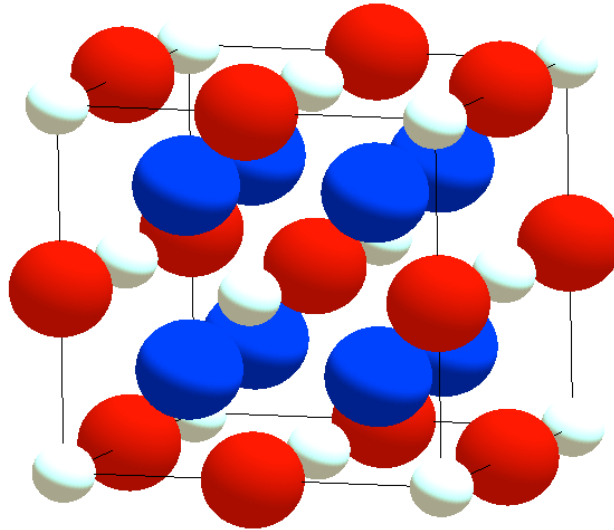
Figure 4.1: Structure of Co$_2$FeSi. Blue balls – cobalt atoms, red – iron, white – silicon

the majority density contributes. Materials with a complete spin polarization at E$_F$ are called half-metallic ferromagnets [3]. They behave like a metal for electrons of one spin direction and like an insulator for the other. The Heusler compound Co$_2$FeSi has attracted particular interest because it is predicted to have a large minority-spin band gap in the order of 1 eV (see figure 4.2)[5, 6] and, with T$_C$ = 1100K [7, 8], it has one of the highest Curie temperatures among the known Heusler compounds. Bulk Co$_2$FeSi has been stabilized in the L2$_1$ structure with a saturation magnetization of 6μ_B at 5K per unit cell [7, 8]. Thin films of Co$_2$FeSi have been successfully used for fabrication of magnetic tunnel junctions [9]. The tunnel magneto-resistance (TMR) ratios of 60% at low and 41% at room temperature suggest that still an improvement in the materials is necessary for successful use in devices, especially with respect to their temperature behaviour. However, the magnetic moment of the thin films is at 3.9 - 4.9μ_B per unit cell still much lower than in bulk samples.

We measured single crytal Co$_2$FeSi sample which was prepared by arc melting of stoichiometric amounts of the constituents in an argon atmosphere at 10^{-4} mbar [31]. The polycrystalline ingots that were formed were then annealed in an evacuated quartz tube for 21 days. This procedure resulted in
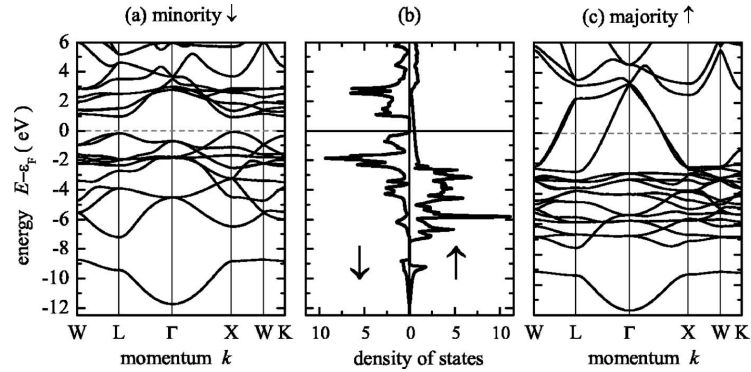
Figure 4.2: Calculated electronic stucture of Co_2FeSi (from [8]).

samples exhibiting the Heusler type $L2_1$ structure, which was verified by x-ray powder diffraction (XRD) using excitation by Cu K_{α} or Mo K_{α} radiation [31]. Flat discs were cut from the ingots and polished for spectroscopic investigations.

In the first section of this chapter we present an introduction to the fundamentals of photoelectron microscopy. Section two contains the description of the spin detection technique used to study the spin polarization near the Fermi edge in the Heusler alloy. Sample preparation and characterization are presented in section three. The following section four presents our evaluation of the spin polarization near the Fermi edge in the Heusler alloy.

4.1   Fundamentals of photoelectron microscopy

Photoelectron emission microscopy (PEEM) is a full field imaging technique based on the illumination of the sample with photons and recording the spatial distribution of emitted electrons. The use of PEEM with tunable synchrotron X-rays that have very high brightness makes possible the attainment of a sufficient signal at a high spatial resolution. Figure 4.3 shows the principle scheme of the SPEEM setup at BESSY II synchrotron in Berlin. The emitted photoelectrons are accelerated to 20 keV towards the microscope by a strong electric field between the sample and the first electrode of the electron optical system (Objective Lens) and then pass through the Intermediate Lens and the Projective Lens. Finally a magnified image is formed on the detector (Chevron style multichannel plate and phosphor screen) that converts electrons into visible light, which is detected by a CCD camera. Alternatively using deflectors the electron beam can be diverted to one of the two spin detectors.
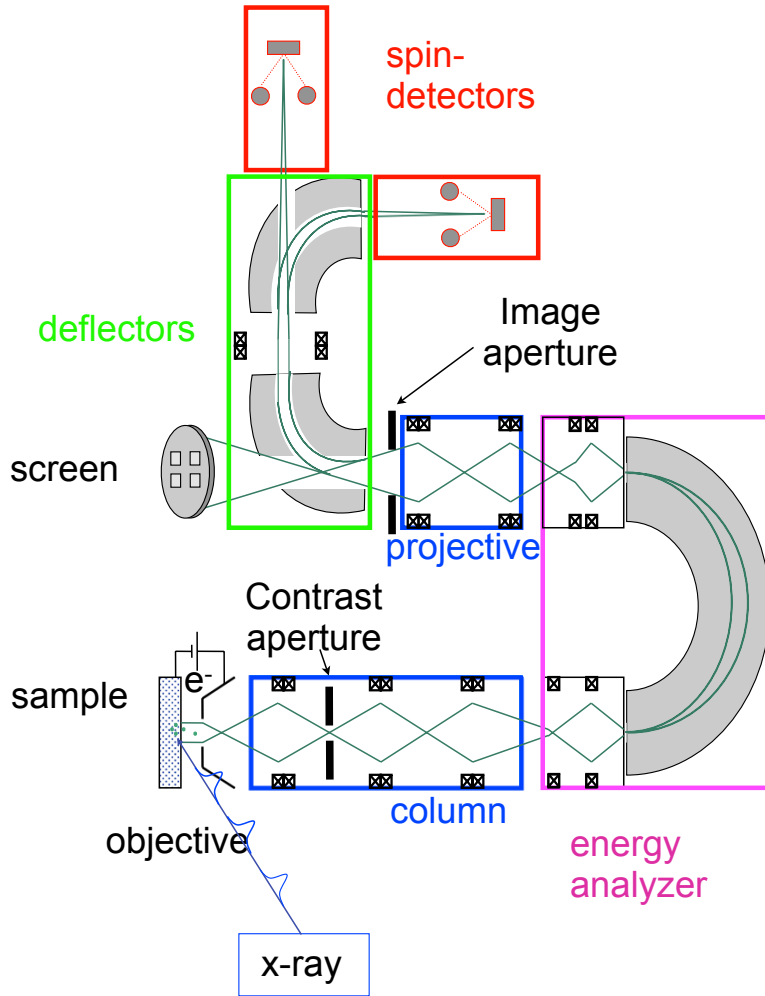
Figure 4.3: PEEM optics

Depending on the sample and the energy of the incoming light different mechanisms generate an image contrast. Spatial variations of the local work function lead to the appearance of the work function contrast. While this contrast is very weak when the sample is illuminated with X-rays it plays a major role in case of UV illumination. The topographical contrast appears due to the roughness of the sample surface. Height difference, sharp edges etc. lead to potential variations and thus to changes in the electron trajectories. Moreover, since the sample is illuminated under a small angle of 16° relative to the surface, a three-dimensional effect of increased illumination on one side and shadowing on the opposite side is produced. The topographic contrast is quite strong - usually scratches or defects are clearly visible. Additional contrast mechanisms can be obtained at synchrotron radiation sources utilizing the strong dependence of the x-ray absorption cross section on excitation energy.

A strong element specific contrast appears when the photon energy is tuned to the absorption edge of the respective element. Areas on the surface containing the corresponding element emit more photoelectrons and thus appear bright in the PEEM image at a given absorption edge X-ray energy.

For magnetic materials the absorption cross section depends not only on the excitation energy, but also on the sample magnetization and the helicity of the incoming light. Magnetic domain contrast can be achieved from magnetic circular dichroism (XMCD) or magnetic linear dichroism (XMLD) by using polarized synchrotron radiation. XMCD spectroscopy can determine the size, the directions, and the anisotropies of the atomic magnetic moments. In a magnetic metal the d shell has a spin moment that is given by the imbalance of spin-up and spin-down states with different occupation. Absorption of right circularly polarized light mainly excites spin-up photoelectrons. Since spin flips are forbidden in electric dipole transitions controlling X-ray absorption and the empty state must have same spin as the emitted electron, the measured resonance intensity is a function of the number of empty d band states of that certain spin. XMLD can be utilized to study the properties of antiferromagnetic materials. In order to separate chemical and magnetic contrast two images taken with opposite helicity aligned parallel and anti-parallel to the sample magnetization are required (figures 4.4a and 4.4b). Then the sum image (shown on the figure 4.4c) will produce the combination of the topographic and chemical contrast and the difference (depicted in figure 4.4d) will give the magnetic contrast. Figure 4.5 shows a zoomed image of one the structures visible in figure 4.4d. The bright area in figure 4.5a corresponds to the case when the polarization vector of light $\mathbf{P}$ (shown as a white arrow) and the magnetization direction $\mathbf{M}$ (red arrows) both point into the same direction. Dark areas appear when the light polarization and magnetization vectors point to opposite directions. When $\mathbf{P}$ is perpendicular to $\mathbf{M}$ a gray area appears in the image. In this case it is not possible to identify in which direction points $\mathbf{M}$ – up or down. In order to solve this problem the sample has to be rotated by 90°. The corresponding image is shown in figure 4.5b. Then the gray domains from figure 4.5a become bright and dark, making the identification of the magnetization direction possible.

The intensity of X-ray magnetic circular dichroism images obtained from two images taken with opposite light polarization can be interpreted by calcu-

(a) σ^+ (b) σ^-

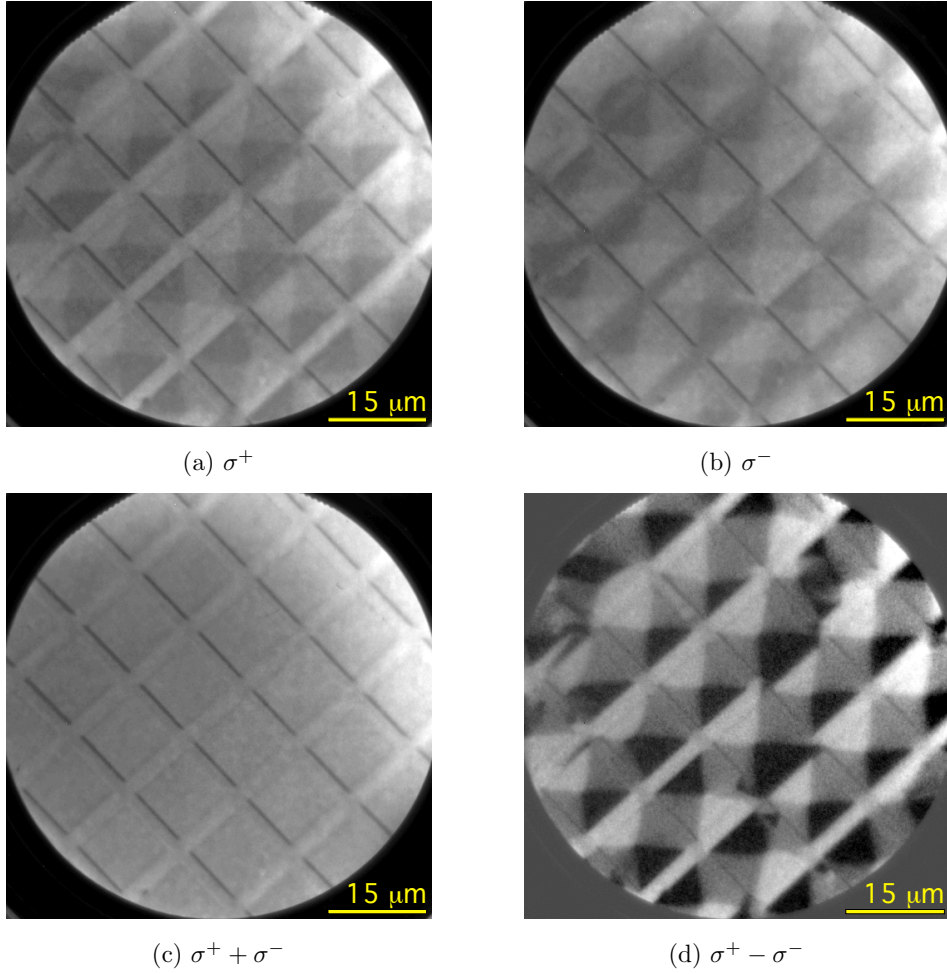(c) $\sigma^+ + \sigma^-$ (d) $\sigma^+ - \sigma^-$

Figure 4.4: PEEM contrast on a thick permalloy film deposited on a patterned silicon wafer taken with different light polarization. (a) image taken with positive helicity of the incoming light, (b) image taken with negative helicity, (c) sum of two images, producing the chemical contrast. (d) difference image giving the magnetic contrast.
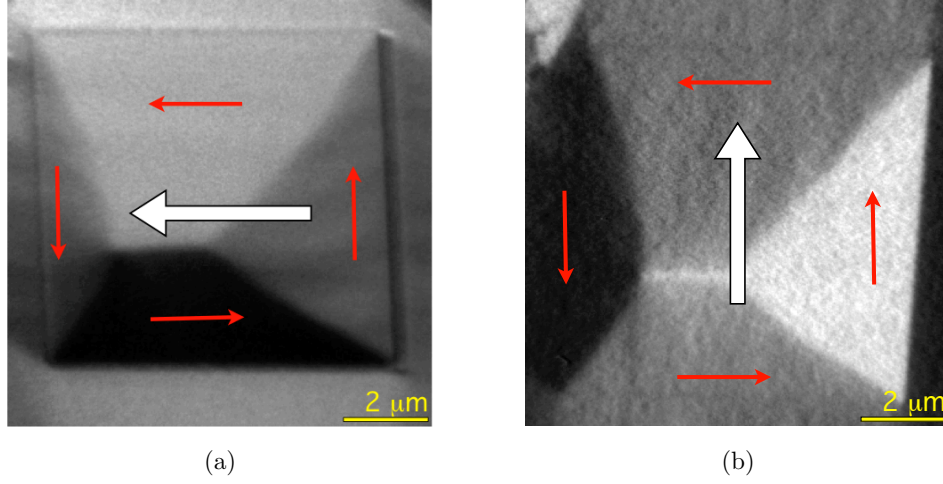
Figure 4.5: Interpretation of the magnetic contrast. White arrow shows po-
larization vector of the incoming light. Red arrows denote magnetization di-
rection. Sample rotated (a) 0° and (b) 90°.

lating the asymmetry A_{XMCD} at each pixel, which is given by:

$$A_{XMCD} \propto \frac{I^+ - I^-}{I^+ + I^-} \propto \mathbf{P} \cdot \mathbf{M} \cos(\alpha) \qquad (4.1)$$

with I^+ , I^- denoting the pixel intensity for the right or left helicity and α be-
ing the angle between the photon polarization $\mathbf{P}$ and the local magnetization
vector $\mathbf{M}$. The observed contrast scales with the degree of circular polar-
ization of the synchrotron radiation. The asymmetry equation ensures that
all contrast mechanisms other than magnetic cancel out, because they do not
depend on the photon helicity. In the raw images, the contrast of chemical,
magnetic and topographic origin is present.

The images obtained in the PEEM experiment suffer usually from different
factors which limit the resolution. The electrons emitted under different an-
gles will focus in different image planes, producing the spherical aberrations.
In order to overcome this problem a contrast aperture is used. The contrast
aperture is placed in the backfocal plane of one of the second lens (see fig-
ure 4.3) and benefits spatial resolution by rejecting all but a narrow band of
electron beam angles and hence reducing the spherical aberration. Chromatic
aberrations arise from electrons having different starting energies which will
be focused in different image planes and play a dominant role in the case of
PEEM investigations together with synchrotron radiation. Although the con-
trast aperture has an electron energy filtering effect and therefore reduces the

chromatic aberrations it fails when electrons starting from different depth and having different energies focus in the same plane. In order to overcome this problem an energy filter is used. This filter is implemented in the SPEEM setup as a hemispherical energy analyzer (see figure 4.3). In addition to the enhancement of lateral resolution, the analyzer also allows photoelectron spectroscopy experiments to be performed. The analyzer is always tuned to a narrow bandpass energy. This setting is selected to avoid any kind of distortion in an image passing through the analyzer. By scanning the start voltage, an additional voltage offset applied to the first lens, we can select the electron energy passing through the system. Other factors affecting the resolution are sample charging, vibrations *etc.*

4.2 Spin detection

The most common method of detecting the spin polarization of electrons is Mott scattering [32, 33]. In Mott detectors the spin polarization is calculated from the measured scattering asymmetry of a gold foil in the detectors:

$$A = (N_L - N_R)/(N_L + N_R), \tag{4.2}$$

with high limit of absolute statistical error

$$\Delta A = 1/\sqrt{N_L + N_R}, \tag{4.3}$$

where N_L and N_R are the number of scattered electrons in the detectors symmetrically positioned with respect to the incoming electron beam. Then the true electron spin polarization P is given by

$$P = A/S, \tag{4.4}$$

where S is a proportionality factor called the Sherman function. S corresponds to the asymmetry measured for a fully polarized beam. An absolute statistical error of the polarization is given by

$$\Delta P = 1/S\sqrt{N_L + N_R} = 1/\sqrt{\varepsilon N_0}, \tag{4.5}$$

where N_0 is the number of incoming electrons and ε is the efficiency of the polarimeter [34]

$$\varepsilon = S^2(N_L + N_R)/N_0 \tag{4.6}$$

In the following subsections we will briefly describe the Mott detector and its commissioning.
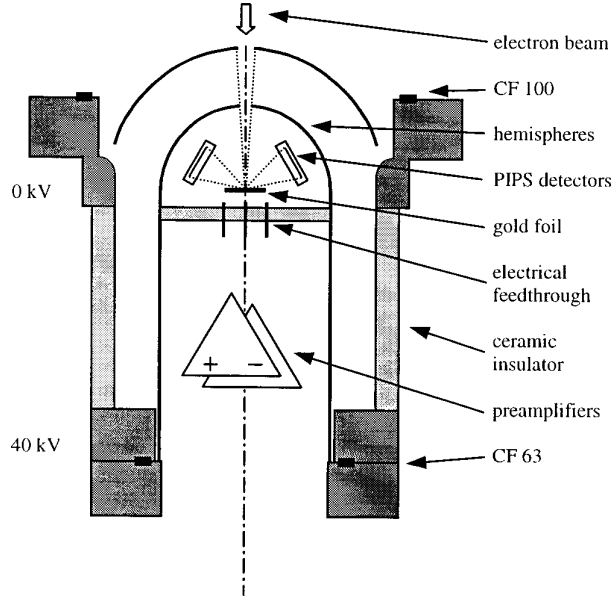
4.2.1   Mott detector

Figure 4.6: Schematic of Mott polarimeter.

The schematics of the spin detector used in the SPEEM instrument at BESSY II is shown in figure 4.6. The two detectors shown in figure 4.3 allow the measurement of the electron spin orientation perpendicular to the drawing plane. The polarimeter has been built by the Surface Magnetism Group at St. Petersburg Technical University [34]. It is based on the classical Mott detector design. The electrons, the polarization of which is to be measured, are accelerated in the field between the two hemispheres. The device was designed to operate at 40 keV scattering energy. Taking into account that the electrons in the PEEM are already accelerated to 20 keV, an additional accelerating voltage of 20 kV was applied between the hemispheres. After back-scattering off the gold foil they are counted by passivated implanted planar silicon (PIPS) barrier detectors. The thickness of the gold foil is 800 Å on a thin free standing formvar film. The active area of the detectors is 10×10 mm^2 and the distance between the centers of the gold foil and the detectors is 17 mm. It is very important to note here that the electrons move in a field free space. Field free regime makes detection scheme insensitive to variations of incoming beam direction and shape.

Inside the polarimeter (outside vacuum) there are four preamplifiers. Each preamplifier includes a section sensitive to the incoming charge, a voltage preamplifier, a quasi-Gauss shaper scheme, and an active filter with Bessel characteristic. The discrimination level of the preamplifiers was calibrated according to the procedure described in reference [35].

4.2.2 Spin detector commissioning

In order to obtain the Sherman function we performed two reference experiments. For this we used the spin-resolved circularly polarized $2p$ (L_3) resonant photoemission technique, a spectroscopic tool with the unique property that it is capable of measuring the local $3d$ spin polarization independent of the orientation of the local moment, allowing the study of local moments not only below, but also above T_C. It utilizes the strong spin-orbit coupling of the $3d$ transition metals 2p core levels. Together with the use of the circular polarization, $2p$ electrons with a preferred spin orientation are resonantly excited into $3d$ unoccupied levels. An Auger decay transfers the spin polarization to the emitted photoelectrons. This way, spin polarization up to 55% has been detected even for antiferromagnets [36].

In the first experiment we measured the spin polarization of the resonant $2p3d3d$ photoemission process in CuO. The sample was provided by the group of Nick Brooks from ESRF. It was transported in a inert atmosphere and transferred into the experimental system avoiding any air exposure. Photon energy was set to Cu L_3 absorption edge (930.4 eV). The red line in the top plot of figure 4.7a corresponds to the parallel alignment of the incoming photon helicity and electron spin. The blue line depicts the spectral line shape for anti-parallel alignment of the incoming photon helicity and electron spin. The measured spectrum reveals mainly Cu $3d^8$ final states [37]. Two peaks at 16.2 eV and 12.6 eV binding energy are derived from ^1S and ^1G atomic states, respectively [38, 39, 40]. The bottom panel of figure 4.7a shows the degree of spin polarization calculated as the ratio between difference and sum spectra of figure 4.7a (top panel). The polarization curve was scaled to fit the known degree of spin polarization in CuO [37] shown in figure 4.7b. After taking into account the degree of circular polarization the resulting Sherman function value is obtained to $S = 0.07 \pm 0.005$. The obtained value is approximately 2 times less than the value of $S = 0.15$ reported by Petrov *et al* [34]. We attribute the observed difference to different discriminator parameters set for our detectors.
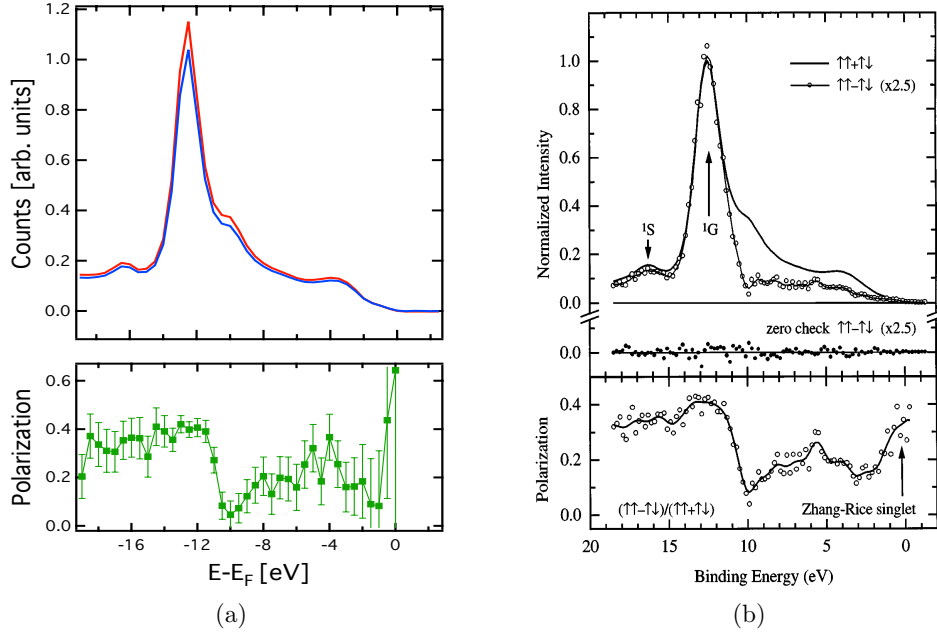
Figure 4.7: CuO spin polarization. **(a)** Measured data. The top panel shows
the valence band photoemission spectra of CuO taken with photon energy
tuned to the Cu L_3 absorption edge. Red (blue) lines correspond to parallel
(anti-parallel) alignment of incoming photon momentum and electron spin.
The bottom panel shows the degree of spin polarization. **(b)** Literature data
(from reference [37]);

Another control experiment to define the value of the Sherman function
utilized spin polarization in Ni using the resonant photoemission technique.
A strong spin polarization in the valence band of Ni, not only below but
also above T_C was observed in the work of Sinkovic *et al* [41]. In this work
it was shown that the low and high temperature spectra provide the direct
identification of the local singlet and triplet $3d^8$ states, both of which have a
considerable amount of band character. The singlets states are located at much
higher binding energies than the triplet states. The latter extend all the way to
the Fermi energy, providing strong support that the orbital degeneracy of the
$3d$ band and the Hund's rule splitting play an important role in ferromagnetic
exchange interactions in band-like late transition metals, both below and above
T_C[42]. The reported polarization is very large, up to about 40% [41].

A thick nickel film (≥ 100 Å) was prepared by *insitu* evaporation of the
pure material onto a silicon substrate. Since the experiment did not require
highly ordered films, substrate cleaning was not required.

The resulting data are illustrated in figure 4.8. The red line in the top plot
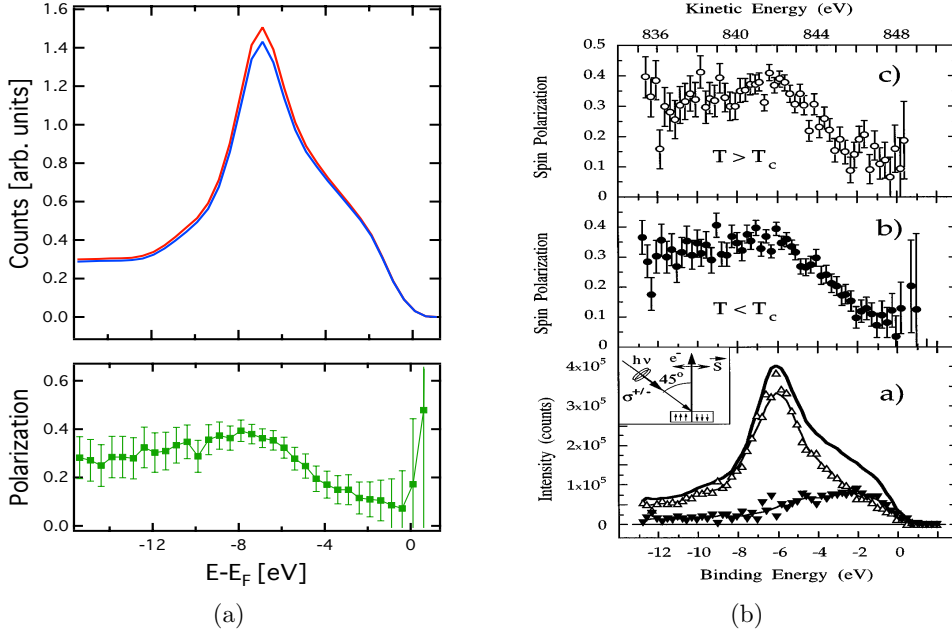of figure 4.8a corresponds to parallel alignment of the incoming photons helicity

Figure 4.8: Ni spin polarization. **(a)** Measured data. The top panel shows the valence band photoemission spectra of Ni taken with photon energy tuned to the Ni L_3 absorption edge. Red (blue) lines correspond to parallel (anti-parallel) alignment of incoming photon momentum and electron spin. The bottom panel shows the degree of spin polarization. **(b)** Literature data (from reference [41]);

and orientation of electrons spin. The blue line depicts spectral line shape for anti-parallel alignment of the incoming photons helicity and the sample magnetization. The bottom panel of figure 4.8a shows the degree of the spin polarization calculated as the ratio between difference and sum spectra. The polarization curve was scaled to fit the known degree of spin polarization in Ni [41]. After taking into account the degree of circular polarization the resulting Sherman function value is $S = 0.07 \pm 0.005$. The value of the Sherman function obtained in Ni experiment is exactly the same as the one obtained in CuO experiment.

4.3 Sample preparation and characterization

Figures 4.9a and 4.9b show the chemical contrast of iron and cobalt, respectively, of the Co_2FeSi sample. The PEEM image shown in figure 4.9a was taken at the photon energy of $h\nu = 707.5$ eV which corresponds to the Fe L_3 absorption edge. The PEEM image shown in figure 4.9b was taken at the photon energy of $h\nu = 778$ eV which corresponds to the Co L_3 absorption

edge. Both images were recorded with horizontal light polarization. Bright
islands visible in figure 4.9a correspond to areas on the sample with higher
concentration of iron than the rest of the surface. The chemical contrast at
the Co L_3 edge (figure 4.9a) exhibits the same island pattern as observed at
the Fe edge except with reversed intensity. From this we conclude that islands
are visible on the sample having higher concentration of Fe and smaller of Co.
The sample shows also a weak magnetic contrast as illustrated by figures 4.9c

(a) Fe chemical contrast

(b) Co chemical contrast

(c) Fe magnetic contrast

(d) Co magnetic contrast
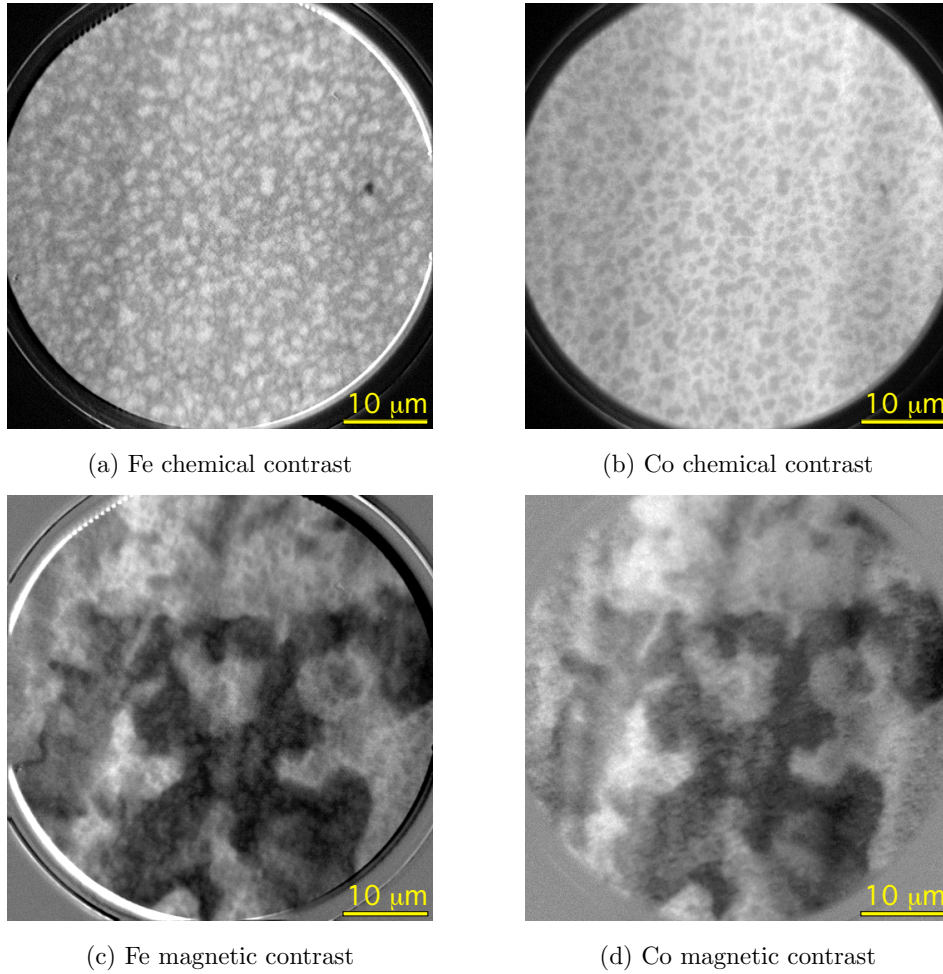
Figure 4.9: Chemical and magnetic contrast of Co_2FeSi after the sample trans-
fer. (a) Chemical contrast of Fe. (b) Chemical contrast of Co. (c) Magnetic
contrast of Fe. (d) Magnetic contrast of Co

and 4.9d. Both images show the sample pattern.

Chemical composition of the sample surface was controlled by means of
X-ray photoemission spectroscopy. We swept the start voltage and integrated
the complete image to obtain the intensity of the photoemitted electrons. The
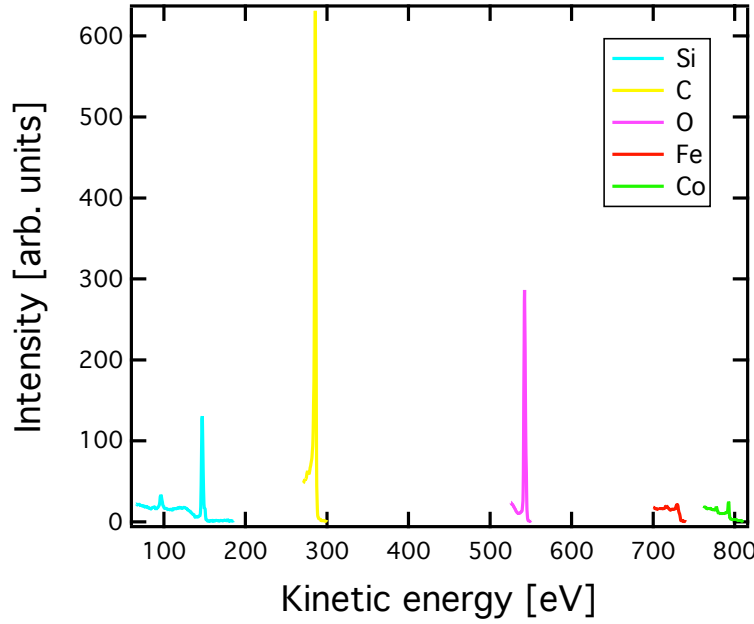
Figure 4.10: Core level photoemission spectra of the Co_2FeSi sample after the transfer.

resulting spectra were normalized to the incoming photon flux and collection time. Since the transmission function of the microscope is not known, all photoemission scans were recorded in the same range of electron kinetic energies. This was achieved by selecting the photon energy such that it tunes to the investigated core level.

Figure 4.10 shows the core level photoemission spectra of the sample after the transfer. It shows high levels of oxygen and carbon contamination.

In order to remove the contamination the sample was treated by 10 cycles of Ar^+ ion sputtering and subsequent annealing at temperatures up to 500°C. Sputtering parameters were set to $5 * 10^{-6}$ mbar Ar pressure, 20 mA emission current and 1000 V beam energy. The recorded ion current was 15 ± 4 μA. The sputtering duration was varied between 10 and 30 minutes. All sputtering cycles were performed under normal incidence, except cycles 5 and 8, which were done under 45° incidence. The annealing period was approximately 30 second.

Figures 4.11a and 4.11b show the PEEM images taken at Fe and Co L_3 edges after the second cycle of cleaning. Compared to the uncleaned sample (figure 4.9) the chemical contrast almost completely disappeared and the magnetic contrast depicted in figures 4.11c and 4.11d is enhanced.

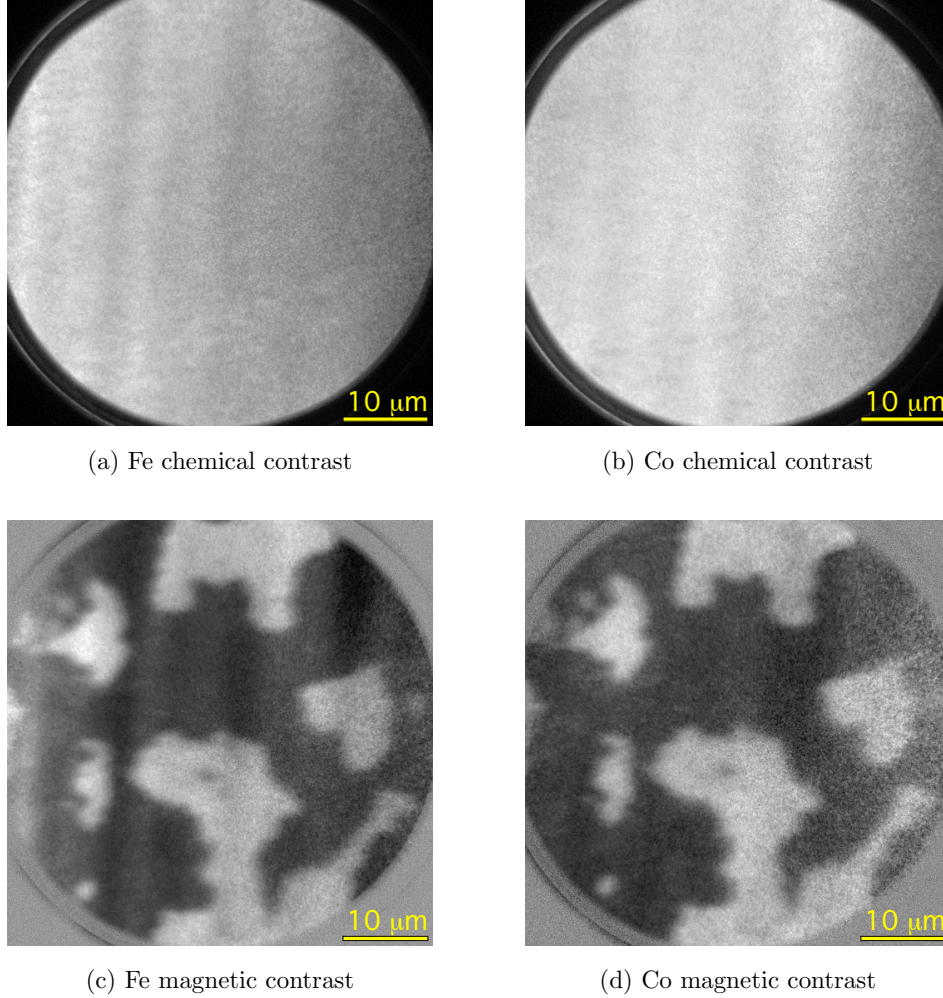The photoemission spectra presented in figure 4.12 still show high level of

(a) Fe chemical contrast

(b) Co chemical contrast

(c) Fe magnetic contrast

(d) Co magnetic contrast

Figure 4.11: Chemical and magnetic contrast of Co$_2$FeSi sample after the second cycle of cleaning. (a) Chemical contrast of Fe. (b) Chemical contrast of Co. (c) Magnetic contrast of Fe. (d) Magnetic contrast of Co

contaminations. We also observed that after annealing the sample the intensity of carbon $1s$ peak increases roughly 2.5 times as it shown in figure 4.13. This increase suggests that the sample bulk is contaminated with carbon.

After six cleaning cycles additional chemical contrast appeared. Figure 4.14 shows PEEM images taken at Fe L$_3$ (4.14a) and Co L$_3$ (4.14b) absorption edges. The image taken at Fe edge shows several dark islands indicating areas with decreased iron concentration. The same areas show higher intensity in the image taken at the Co L$_3$ edge (4.14b) suggesting a higher concentration of Co in the islands when comparing to the rest of the sample. The formation of islands with a different stoichiometry may originate from a preferential sputtering of different chemical elements. During subsequent sputtering cycles
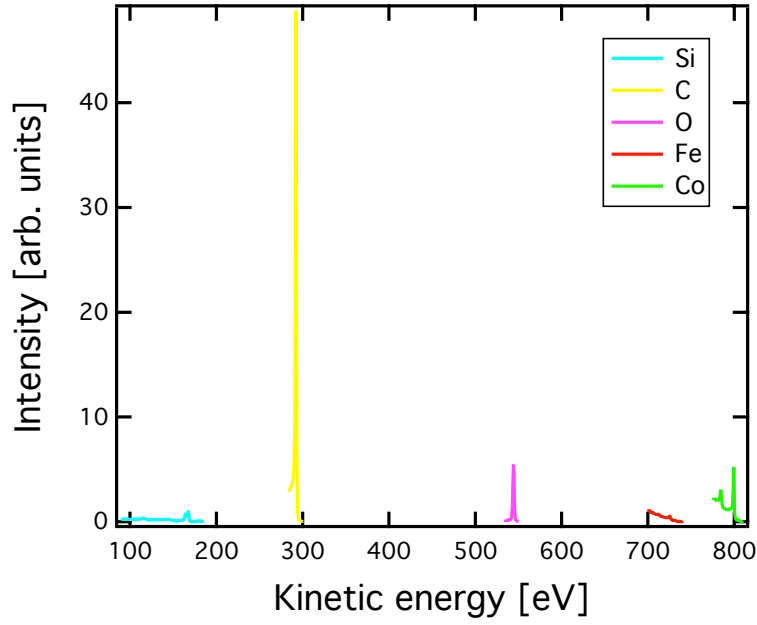
Figure 4.12: Core level photoemission spectra of the Co$_2$FeSi sample taken after the second cycle of cleaning.
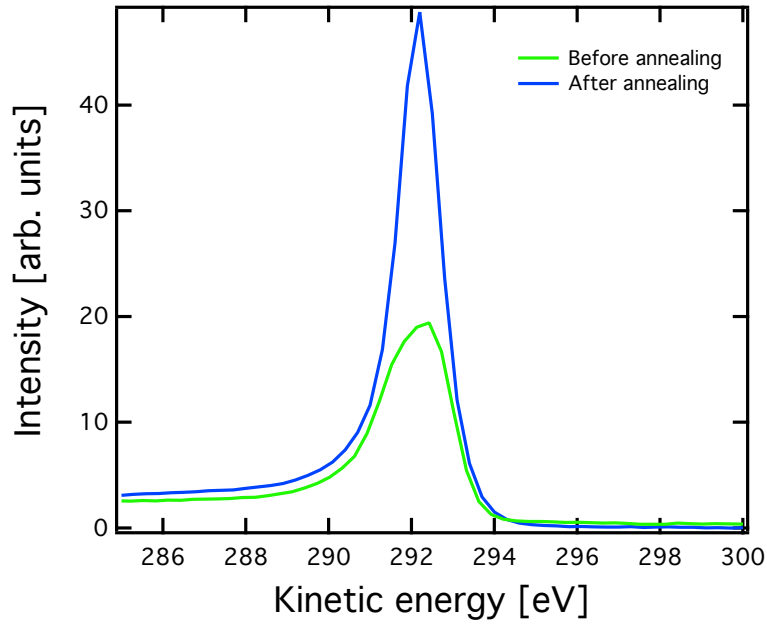

Figure 4.13: Photoemission core level spectra of the Co$_2$FeSi sample showing of C 1s taken before (green curve) and after (blue curve) sample annealing.
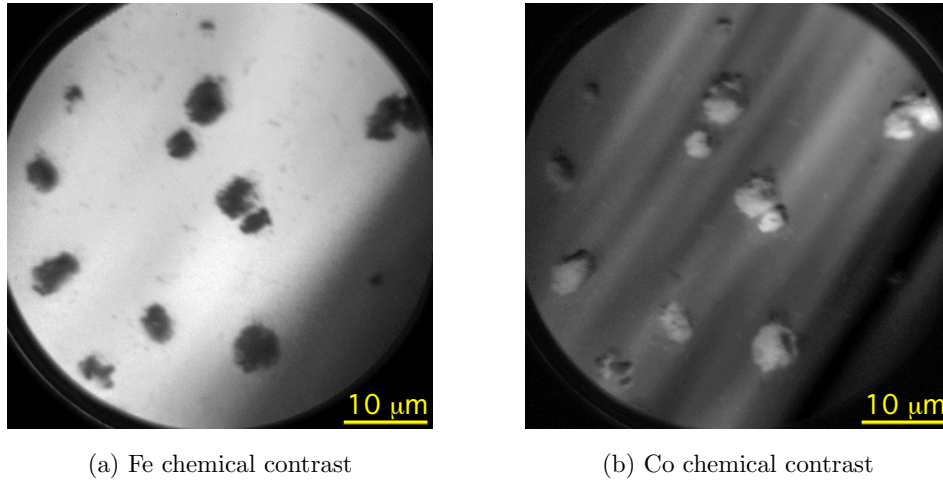
(a) Fe chemical contrast

(b) Co chemical contrast

Figure 4.14: Chemical contrast on the of the Co$_2$FeSi sample after the 6th cycle of annealing.

the amount and the size of these islands increased on the surface. However the position of already existing islands remained unchanged. This suggests that they are pinned to defects present in the crystal.

After the 10th cleaning cycle the amount of contaminants was strongly reduced and the sample composition was close to stoichiometric. Figure 4.15 shows silicon 2p, iron 2p and cobalt 2p XPS spectra taken after the 11th cycle of cleaning. The measured spectra were normalized to the incoming photon flux and collection time. Since the transmission function of the microscope is not known, all photoemission scans were recorded in the same electron kinetic energy range by varying the photon energy to tune to the investigated core level. Silicon 2p XPS spectrum was recorded at a photon energy $h\nu = 285$ eV, iron at $h\nu = 880$ eV, cobalt at $h\nu = 940$ eV. The kinetic energy range for all spectra was between 140 and 180 eV. The photon flux was estimated by a pre-calibrated GaAs diode that exist in the beamline. For all the spectra a constant background defined by the intensity before the peak was subtracted.

To estimate the expected intensity ratios for cobalt, iron and silicon we used the NIST Database for the Simulation of Electron Spectra for Surface Analysis (SESSA) [43, 44]. SESSA has been designed to facilitate the quantitative analysis of Auger electron spectroscopy (AES) and X-ray photoelectron spectroscopy (XPS). The database contains physical data required for quantitative interpretation of an electron spectrum for a specimen with a given composition. A simulation module is also available within SESSA that provides an estimate of peak intensities as well as the energy and angular distribution of
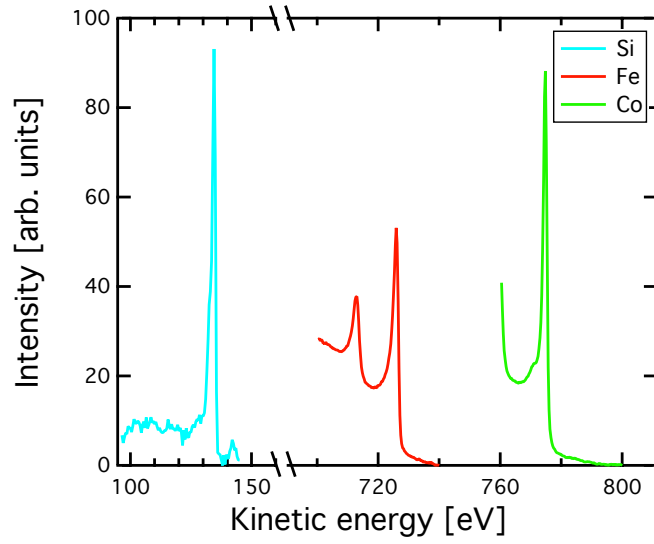
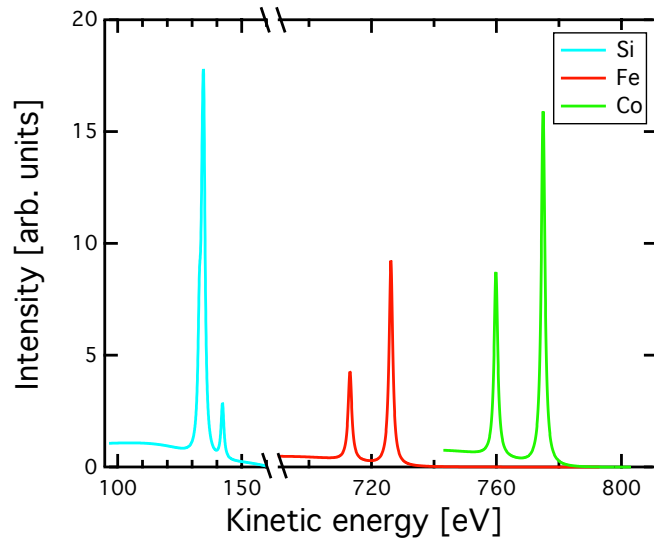Figure 4.15: Measured core level photoemission spectra of Co$_2$FeSi after the last cycle of cleaning.

Figure 4.16: Simulated photoemission spectra of stoichiometric Co$_2$FeSi.

(a) Fe chemical contrast

(b) Co chemical contrast

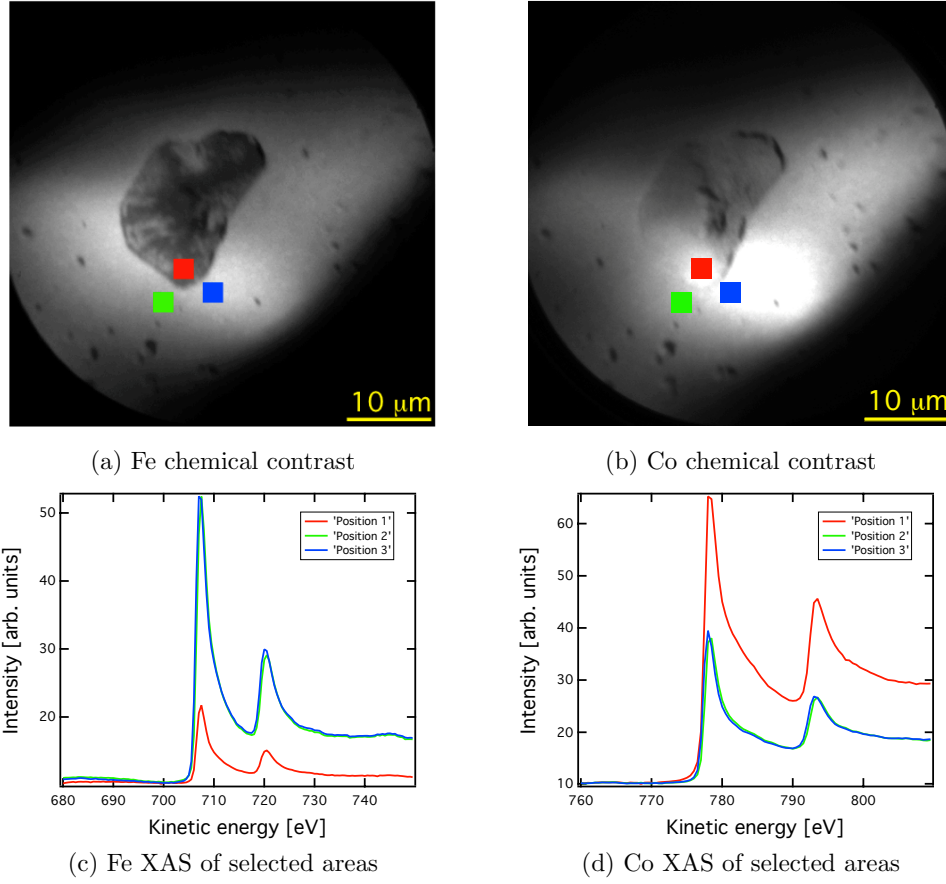(c) Fe XAS of selected areas

(d) Co XAS of selected areas

Figure 4.17: Images (a) and (b) show the chemical contrast after the last cleaning at Fe and Co edge, respectively. Colored squares indicated the area from which Fe (c) and Co (d) XAS spectra were integrated.

the emitted electron flux. We successfully simulated the bulk sample with Co_2FeSi composition. The result of the simulation is shown in figure 4.16. Both measured (figure 4.15) and simulated (figure 4.16) spectra show nearly identical intensity ratios which suggest that the sample composition is close to stoichiometric. A small discrepancy in the intensity of the silicon peak may come from an incorrect normalization procedure. The beamline and the GaAs diode used to estimate the photon flux are slightly contaminated with carbon, which produced a so called "dip" in the photon intensity in a certain energy range around C $1s$ core level. Due to this contamination the response of the diode is strongly non-linear around photon energies between 270 and 290 eV, which contains the photon energy used to measure the silicon XPS spectrum (285 eV).

The chemical contrast on the sample after the last cycle of cleaning is shown

59

in figures 4.17a and 4.17a for iron and cobalt respectively. The figures reveal a prominent structure in the center of each image. We compared the chemical composition of the structure by comparing the X-ray absorption spectra at and around the structure. We performed photon energy scans around the Fe and Co absorption edges recording an image at every step. Then the regions of interest were selected as it is noted in figures 4.17a and 4.17b with red, green and blue squares. For every image we integrated the intensity within each of these regions of interest. The resulting XAS spectra are shown in figures 4.17c and 4.17d for iron and cobalt respectively. The line color in figures 4.17c and 4.17d corresponds to regions of interest depicted in figures 4.17a and 4.17b. The spectra recorded outside the structure (green and blue) have almost the same intensity while the intensity of the spectrum taken from the structure (red) is different. The intensity differences in the absorption spectra indicate that the island contains about 2 times more Co and about 4 times less Fe than other areas on the sample.

4.4 Spin polarization at the Fermi level

The area shown in figure 4.17 was used for spin resolved investigations due to the large domains that are pinned at the defect. Figure 4.18 shows the XMCD-images around that area. The XMCD images shown in figures 4.18b and 4.18c were taken by rotating the sample by 22.5° and 45° with respect to the original sample position 4.18a. The rotation of the sample reveals the expected vectorial property of the contrast in XMCD-images as described by equation 4.1. The image displays a rather large defective area in the center that shows only weak magnetic contrast. Large domains are pinned at that defect. Three circles in figure 4.18a, marked by an arrow, corresponds to areas that were used for the spin resolved photoemission spectra.

In order to record spin resolved photoemission spectra three different areas on the sample were used – a dark domain, a bright domain and a mixture of the domains as it is shown in figure 4.18a with color circles. Inside a single domain all spins are aligned in the same direction. We exploited this to measure the spin polarization. The spectra were excited by photons of 120 eV energy. The electric field vector of the linearly polarized photons was aligned in the plane of incidence (p-polarization). The diameter of the selected area is 13 μm. The area was selected using the image aperture of the microscope (see figure 4.3). Before and after each spin detector scan an XMCD image of the selected area
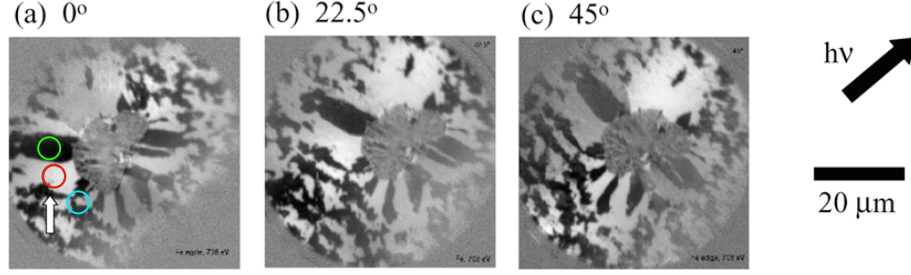
Figure 4.18: XMCD images of $Co_2FeSi(110)$. The images are recorded at the
Fe L_3-edge. The sample was rotated by 22.5° (b) and 45° (c) with respect to
the initial orientation (a). Color circles in (a), assigned by an arrow, marks
areas that were used for the spin resolved photoemission spectra.

was recorded (figures 4.19, 4.20 and 4.21). These images were used to perform
a correction for domain distribution within the selected areas. Bright and
dark domain will have to produce an opposite spin polarization. We measured
both of them in order to compensate for a possible instrumentally induced
asymmetry. We also measured mixed domains as a crosscheck of our result. For
each area we recorded XMCD images before and after the photoemission/spin
detector scans. Figure 4.19 shows a bright domain area, figure 4.20 a dark
domain and figure 4.21 a mixture of domains. The measured polarization was
scaled with the distribution of the domains inside the corresponding XMCD
image. We used two XMCD images taken before and after a spin resolved
photoemission scan to compensate for the observed sample drift – while the
experiment was running the distribution of the domains in the region of interest
was changing slightly. We assumed that the change in the polarization of the
selected area was linear as a function of time.

The resulted spectra and spin polarization are shown in figure 4.22. The
top panel shows the spin resolved spectra for spin-up states (red), spin-down
states (green) and average spectrum. The bottom panel shows the degree of
spin polarization. The spectra exhibit a peak at about 1 eV below the Fermi
energy (E_F) and a broader feature around -6 eV. The low lying s-states being
located at about -10 eV are absent. The same is true for the s–p hybridization
gap that appears in the electronic structure (compare [6]). Most evidently,
the spectra do not reveal the low density of states region found in high energy
photoemission [45, 5]. Considering the low energy resolution used here (0.5
eV), this shape of the spectra is expected. Due to the loss of intensity caused
by the spatial resolution as well as the spin detection, a higher resolution
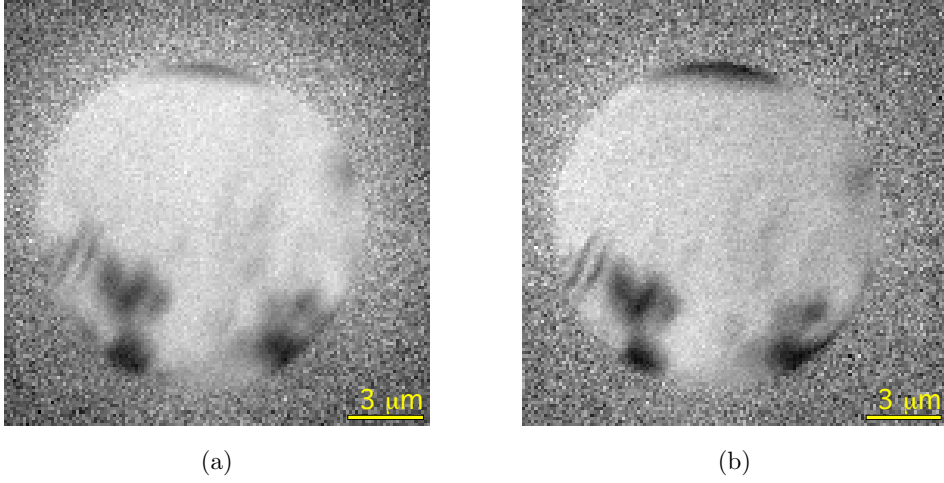cannot be applied. Overall, the spectra are similar to those taken with Mg-K$_\alpha$

(a)   (b)

Figure 4.19: XMCD images of the bright domain used for spin polarization calculation taken (a) before and (b) after the scan.
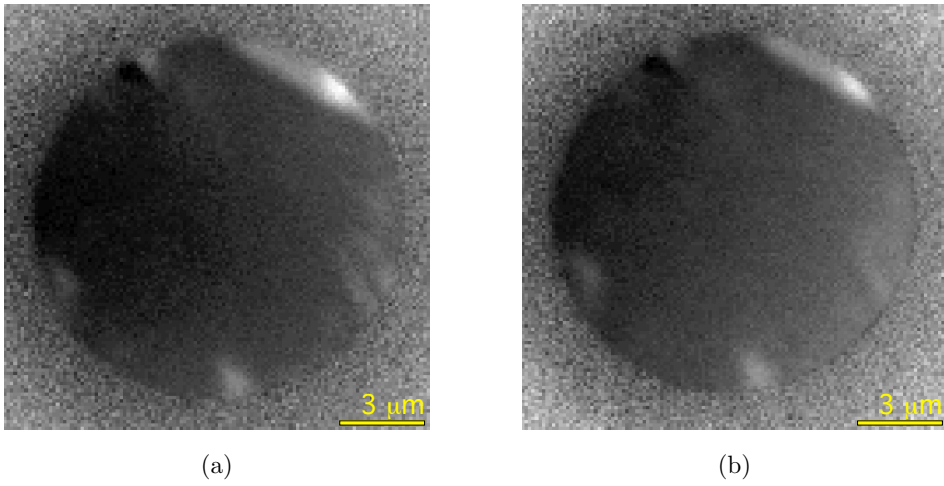

(a)   (b)

Figure 4.20: XMCD images of the dark domain used for spin polarization calculation taken (a) before and (b) after the scan.
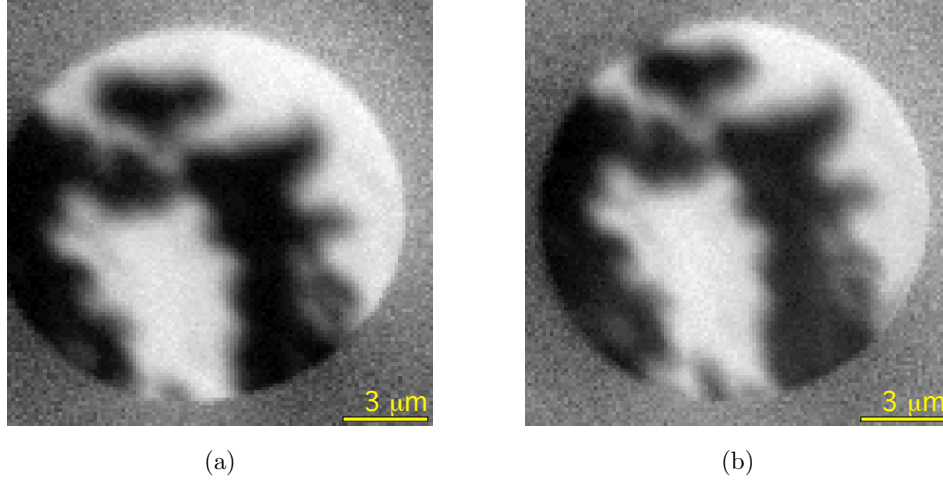
(a)   (b)

Figure 4.21: XMCD images of the mixture of the domains used for spin polar-
ization calculation taken (a) before and (b) after the scan.

radiation that also show a pronounced intensity only close to E_F[45]. The
enhancement of the emission from the d-bands with respect to the s-bands
is explained by the difference in the cross-section. The high density of states
at about 6 eV binding energy is, however, clearly seen in the spectra. The
spin polarization at the Fermi energy amounts to $(16 \pm 5)\%$ and increases to
$(35 \pm 4)\%$ in the region of the d-bands. It is positive over the entire range of
energies. The value at the Fermi energy is considerably higher than the one
reported by Wang *et al* [46, 47] for Co_2MnSi films $(8 \div 10\%)$ for photon energies
of 80 eV. The value at E_F does not reach the value of about 30% found in the
TMR study of Co_2FeSi thin films at room temperature [9], however, the spin
polarization of the d-bands is already slightly higher compared with that value.
The reduction of the spin polarization at room temperature may be caused by
a thermal occupation of the minority spin conduction bands insofar as the
half-metallic gap is very close to the bottom of those bands. This might hint
a partial loss of the half-metallicity in Co_2FeSi at elevated temperatures. It is
worthwhile to note that the observed reduction of the spin polarization may
also be caused by a contamination of the sample as the used excitation energy
makes the method extremely surface sensitive. At higher binding energies the
spin polarization stays constant at a value of about 30%. At energies below
-8 eV one expects the only emission from the low lying s-bands or secondary
electrons forming the background. The s-states are only weakly polarized.
Furthermore, the emission from the s-bands is strongly suppressed as discussed
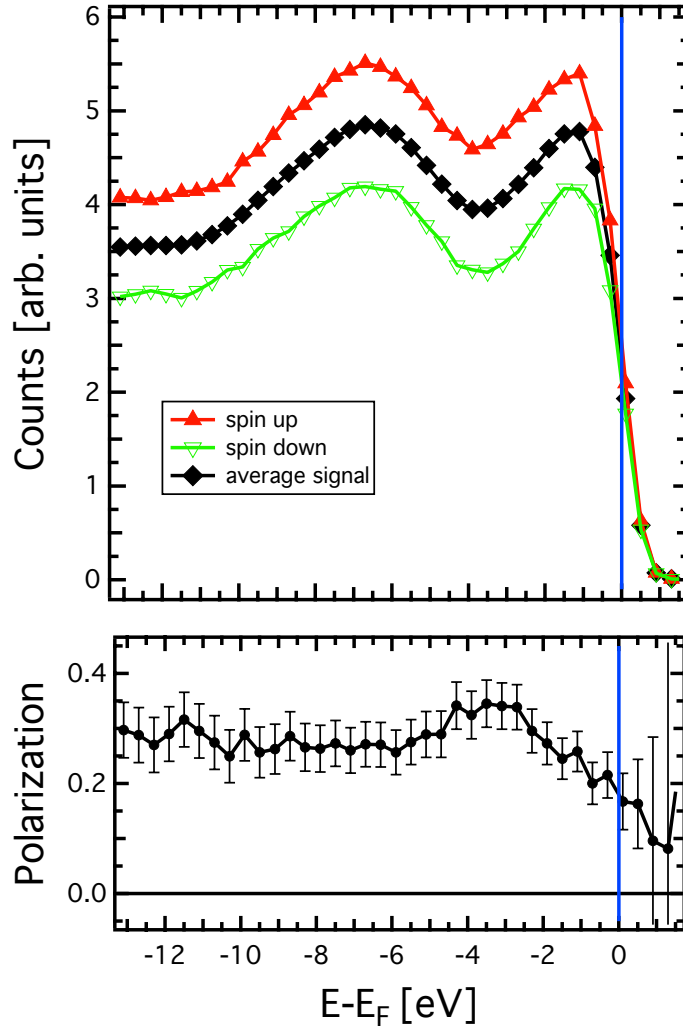in [45]. Therefore, the spin polarization of the electrons at these energies arises

63

Figure 4.22: Spin polarized photoemission of $Co_2FeSi(110)$. The spectra were taken in a single domain. The top panel shows the spin resolved spectra and the bottom panel shows the degree of spin polarization. The spectra were excited by photons of 120 eV energy.

from a polarization of the secondaries by the magnetization of the sample (transport polarization) as explained in [48, 49].

4.5 Summary

This chapter contains a study of the Co_2FeSi Heusler alloy by means of spin-resolved photoelectron spectro-microscopy. For this system 100 % spin polarization at the Fermi edge was predicted, thus making it an attractive candidate for the spintronics applications. Unfortunately the experimentally obtained polarization is much smaller and has a value of 10-12 %. At the beginning of our experiments we performed the commissioning of the spin detectors. Using the spin-resolved circularly polarized $2p$ (L_3) resonant photoemission technique, a spectroscopic tool with the unique property that it is capable of measuring the local $3d$ spin polarization independent of the orientation of the local moment, allowing the study of local moments not only below, but also above T_C, we measured the spin polarization of a thick nickel film and of CuO. By comparing the asymmetry obtained in the experiment with the published spin polarization for these materials we obtained the Sherman function value of 0.07.

Using photoelectron microscopy we demonstrate that the surface of Co_2FeSi sample has areas of mostly non-stoichiometric composition.

Selecting an area on the surface with composition close to the nominal stoichiometry and performing spin-resolved measurements of the valence band we obtained the spin polarization at the Fermi level of 16% which was the highest experimentally determined so far for this material.

Chapter 5

Photohole lifetime effects in ferromagnetic nickel

In this chapter we discuss the spin dependent quasiparticle band structure of Ni (111) investigated with high resolution angle resolved photoemission spectroscopy. At low temperatures (50 K) a renormalization of quasiparticle energy and lifetime indicative of electron-phonon coupling is observed in agreement with literature [50]. With increasing temperature we observe a decreasing quasiparticle lifetime at the Fermi level for all probed minority spin bands as expected from electron phonon coupling. Surprisingly the majority spin states behave differently. We actually observe a slightly increased lifetime at room temperature. The corresponding increase in Fermi velocity points to a temperature dependent reduction of the majority spin quasiparticle renormalization. In the first section of the chapter we introduce the experimental details. In the second part we discuss the analysis techniques which were applied for data processing. The third part holds a detailed analysis of correlation effects observed at low temperature. In the forth part we compare low and room temperature band structures and discuss observed changes at elevated temperatures.

5.1 Electronic properties of nickel

One of the fundamental consequences of electron correlation effects is that the bare particles in solids become 'dressed' with the excitation cloud resulting in quasiparticles. Such a quasiparticle will carry the same spin and charge as the original particle, but will have a renormalized mass and a finite lifetime. Understanding of the correlation effects drew a lot of research attention in the last decade due to its importance in various fields, ranging from

the superconductivity[51, 52] to spintronics[53]. Ni provides a suitable model system, since it has exchange-split Fermi surfaces where quasiparticles with different spin character and effective mass exist. There are both pure d and hybridized sp–d bands present at the Fermi surface [54, 55, 56, 57, 58].

Furthermore, the influence of electron correlation effects on the spin-polarized Ni $3d$ bands has been well established and ranges from unusual spectral features, such as the spin-polarized 6 eV satellite [59, 60, 61, 62], reduced $3d$ band widths and exchange splittings [63, 64, 65, 66]. Values of ≈25%[67, 54, 55, 56, 68] for the 3d bandwidth reduction and ≈50%[67, 54, 55, 56, 68] for a reduced exchange splitting relative to bandstructure calculations within the local spin-density approximation (LSDA)[69, 70] have been reported. We should also note that the electronic band structure of Ni is relatively simple from a theoretical point of view; most of the majority-spin $3d$ states of Ni are occupied, and less than one hole exists in the minority-spin $3d$ states[71]. The exchange splitting is typically $160 \div 330$ meV [64], displaying a temperature dependence as expected from the Stoner model [66].

The $3d$ band narrowing and the reduced exchange splittings of the Ni 3d bands are explained in terms of the electron correlation effects [72, 73, 74].

Here we report the spin dependent quasiparticle renormalization on energy scales below the Coulomb interaction, responsible for charge fluctuations, and the exchange interactions, responsible for spin fluctuations. The results point to an unexpected spin dependent electron-phonon coupling.

5.2 Experimental details

We studied the spin dependent quasiparticle band structure of Ni (111) with high resolution angle-resolved photoemission spectroscopy (ARPES) to obtain detailed insight into the electronic self energy. The experiment was performed at the UE-112 beamline of the BESSY-II storage ring using the "1^3" spectrometer. During our experiment the overall energy resolution of the beamline and analyzer was set to 11 meV and the minimum temperature that we reached at the sample was 40 K. A thick (≈100Å) Ni(111) film was grown epitaxially on a W(110) surface. The W substrate was cleaned by several cycles of oxygen treatment at high temperature followed by flashing to 2000 K. This resulted in a clean and atomically well ordered surface. The cleanness of the sample was checked by the presence and intensity of surface induced *4f* peaks as well as

the absence of carbon lines in the valence band [75]. W bulk and surface state photoemission was used to check the atomic order at the surface. During Ni evaporation the pressure in the chamber was kept below 1×10^{-9}mbar and the measurements were performed at a pressure better than 1×10^{-10}mbar. The ARPES spectra were recorded with a photon energy of 136 eV. This value was chosen since at that photon energy the curvatures of constant energy spheres in k-space are relatively small. We can therefore scan wavevector values for the Γ-point to the Brillouin zone boundary in about 17° varying the photoelectron emission direction. The photon energy was also chosen to scan through the Γ-point of the 3-rd Brilouin zone. This can be seen as follows: For a cubic lattice the relation between the primitive lattice vectors and the reciprocal lattice vectors is $\mathbf{b} = \frac{2\pi}{\mathbf{a}}$. Knowing the lattice parameter of Ni to be $\mathbf{a} = 3.52$Å we get $\mathbf{b} = 1.78$Å^{-1}. Taking into account the inner potential value $V_0 = 8.14$ eV [56] we could estimate that the third Γ point of Ni corresponds to a kinetic energy of electrons of about 132eV. Now taking into account the work function of the analyzer the required excitation energy of 136 eV is obtained. The accessible
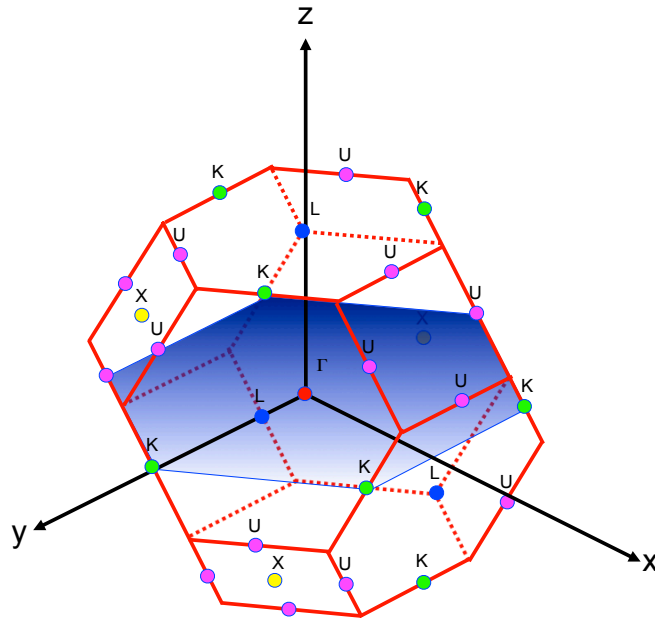

Figure 5.1: Sketch of the Ni Brillouin zone

plane in the Ni bulk Brillouin zone is shown in figure 5.1. The notations of the high symmetry points of the Brillouin zone are used after Bouckaert et al. [76]. The measured Fermi surface is presented in figure 5.2d. The solid yellow line indicates the line along which ARPES data were taken. The dashed lines indicate the positions of d and sp-like bands. The Fermi surface measurement
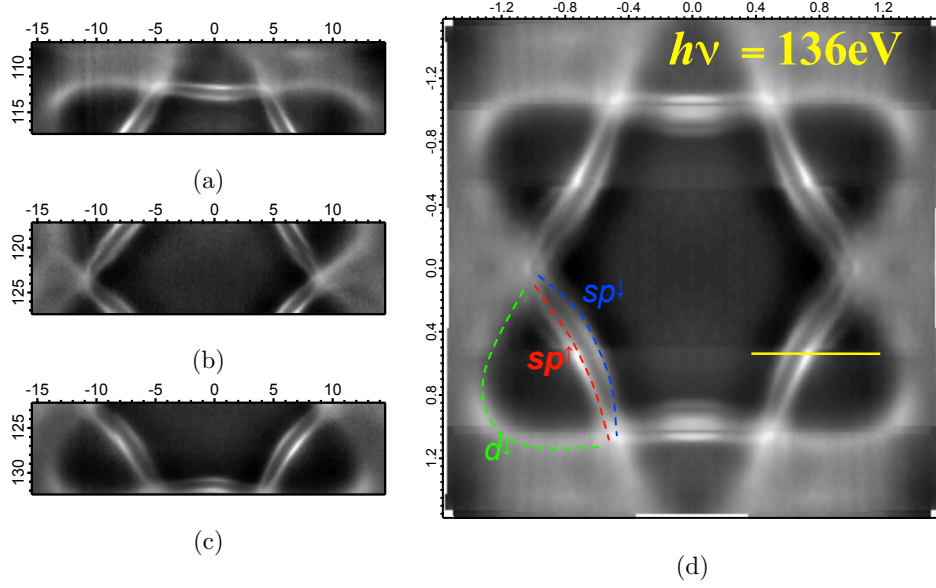
Figure 5.2: Experimental Fermi surface. Measured polar angle regions (a) from $-15°$ to $-5°$, (b) from $-5°$ to $+5°$ and from (c) $0°$ to $+10°$ (d) Experimentally obtained Fermi surface of Ni with the assignment of minority d ($d^\downarrow$), majority sp-like ($sp^\uparrow$) and minority sp-like ($sp^\downarrow$) bands.

was done by scanning three polar angle regions relative to the $\Gamma - K$ direction: the polar angle of the sample position was varied from $-15°$ to $-5°$ (see figure 5.2a), from $-5°$ to $+5°$ (figure 5.2b) and from $0°$ to $+10°$ (figure 5.2c). Later on the measured slices were merged together, converted from angular to k scale and, taking the symmetry into account, the resulting image was mirrored against $k_x = 0$ (horizontal axis in figure 5.2d)and $k_y = 0$ (vertical axis in figure 5.2d) lines in order to enhance the image. The yellow line in figure 5.2d denotes the position in the Brillouin zone where the high resolution data shown below were recorded. The overall energy resolution in the experiment was set to 12meV. The angular resolution of the analyzer for the detailed scans was set to $0.01°$ which at the given excitation energy corresponds to a momentum resolution below 0.05Å^{-1}.

A wide angle scan along the yellow line in figure 5.2d is shown in figure 5.3. The figure shows the dispersing minority sp-like ($sp^\downarrow$), majority sp-like ($sp^\uparrow$), minority d ($d^\downarrow$) and majority d ($d^\uparrow$) bands which cross the Fermi level as indicated in figure 5.2d. As it is known from theoretical calculations [50] the sp-like bands contain approximately 80-90% of the d weight.
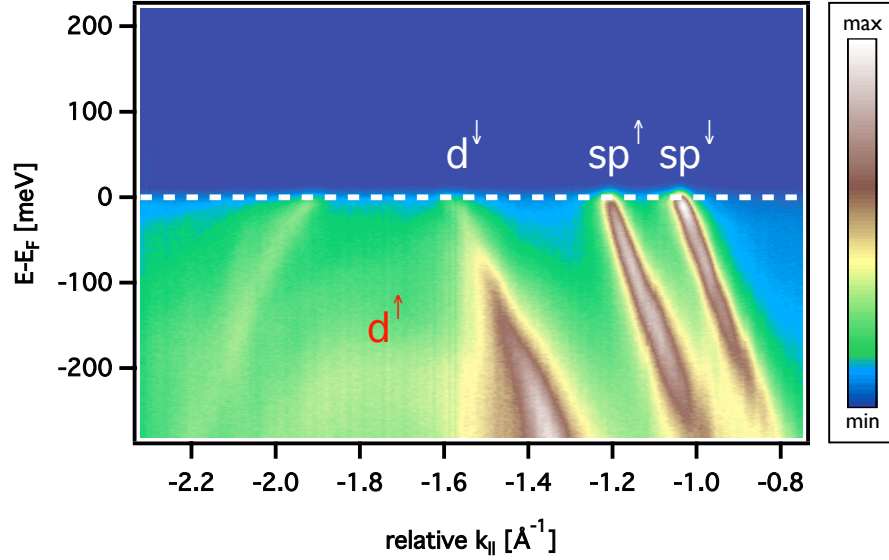
Figure 5.3: Wide angle scan of Ni(111). The dispersing $sp^{\uparrow\downarrow}$ and $d^{\uparrow\downarrow}$ bands which cross the Fermi level are also indicated.

5.3 Data analysis procedures

The data analysis applied to the measured spectra generally consists of three main steps. In the first step the measured data are normalized, converted from angular to k scale and converted from kinetic energy to binding energy scales. In the second step the band dispersion and band width are extracted from the measured ARPES image. In the third step we analyze the properties of the band obtained in the second step in order to gain insight into the interactions present in the sample. In addition to the automated data analysis scripts we also developed a model. Each of the steps will be described in detail in the following parts.

5.3.1 Data normalization

Before the measured data can be analyzed a normalization procedure is required in order to correct for non-linearities in the response of the detection system. This detector function includes all possible effects that influence the measured image, e.g. detector sensitivity, interference at the analyzer slit, inhomogeneous illumination of the detector due to an imperfect alignment of the sample, *etc.* For correcting the detector sensitivity we must consider how the recording scheme of the analyzer functions.

In the sweep mode each intensity distribution curve at a given energy as

a function of dispersion angle (angular distribution curve ADC) runs through the whole multichannel plate detector. Thus along the energy direction the recorded images are corrected for the detector sensitivity. However the detector sensitivity along the angular direction is not corrected in this scheme and this can lead to a distorted image along the angular direction as shown in figure 5.4a.

It is important to mention here that all the above enumerated effects included in the detector function are influencing the recorded data in completely different ways. Such a complex influence requires that the data used for normalization should be acquired exactly at the same sample position and for the same analyzer settings as the data. In order to overcome this problem we used one of two known normalization techniques. If the experiment was performed at low excitation energy $h\nu \leq 70$eV, then the second order light $2h\nu$ from the monochromator is strong enough to provide sufficient intensity above the Fermi level at photon energy $h\nu$. In case of high excitation energy, when the second order light can not provide sufficient intensity to perform the normalization we used another technique called background wave normalization. In this case we changed the excitation energy by 15–20 eV, left the sample and analyzer settings unchanged and repeated the scan. Thus we were measuring the background signal as shown by the background wave in figure 5.4c. This procedure relies on the assumption that at such photoelectron kinetic energies only the unstructured inelastic photoemission background contributes. In both cases we integrated the background signal along the energy direction in order to improve the signal to noise ratio (figure 5.4d) and then we divided each ADC channel with the obtained background. The result of the normalization procedure is illustrated in figure 5.4b. After this normalization a k-scale conversion was performed. As described in section 3.2 the angular momentum $k_{||}$ depends on kinetic energy and scattering angle as given by

$$k_{||} = \sqrt{\frac{2m_e}{\hbar^2}} \sqrt{E_{kinetic}} \sin\theta. \qquad (5.1)$$

Since the dependence of $k_{||}$ on the angle is not linear a direct one–to–one conversion is not possible. Instead, during the conversion procedure, we created a new dataset with a higher number of points along the k direction as in the original dataset. Minimum and maximum values of $k_{||}$ were calculated directly from equation 5.1. Intermediate points were calculated as the linear interpolation between the two closest angles in the measured dataset for a selected
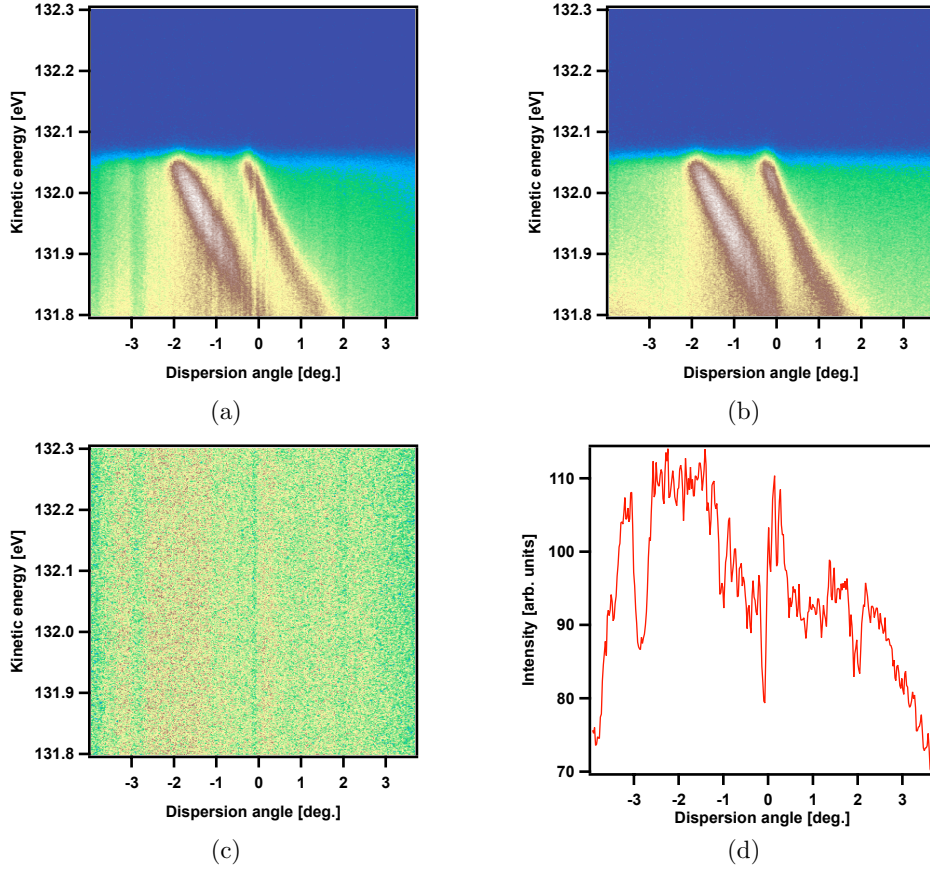
Figure 5.4: Data normalization. Measured image is transposed to have data presentation consistent with other plots. (a) ARPES image as measured; (b) after normalizing to the background wave; (c) background wave; (d) normalization curve.

$k_{\parallel}$.

The last step of the data normalization contains the conversion from kinetic energy to binding energy scale. Since the precise position of the monochromator, especially in the scale of few meV, is not known we extracted the position of the Fermi level from the dataset itself. In order to do this, we integrated the whole dataset along the k direction which resulted in the angle-integrated spectrum (AIS) shown in figure 5.5a with red symbols. We found that in most of the cases we could describe this spectrum with the following eq.

$$\text{AIS} = P_4(E) * f(E, E_f) + C, \qquad (5.2)$$

where $P_4(E)$ is a 4th order polynomial function $- c_0 + c_1 * x + c_2 * x^2 + c_3 * x^3$, $f(E, E_f)$ is the Fermi-Dirac distribution $- 1/(\exp(\frac{E-E_f}{k_b T}) + 1)$, E_f is the Fermi

energy and C is a constant offset. The result of the fit is shown as a green line in figure 5.5a. By subtracting E_f from the energy scale of our dataset we obtain the final result of the normalization procedures shown in figure 5.5b.

5.3.2 ARPES image fits

In order to quantitatively analyze the spectral line shape in the second step of the data analysis we performed fits of the normalized datasets.

In our analysis we fitted the momentum distribution curves (MDC's) – the intensity distribution curves as a function of momentum for a given binding energy. MDC analysis has a few advantages when compared to the EDC (energy distribution curve at given momentum) analysis. One of the biggest problems of EDC analysis lies in the fact that in the case of the interacting electron system EDCs show a complicated line shape structure. In figure 5.6a we calculated a model ARPES image. In this model we assumed the presence of two bands with linear dispersion. For both bands strong electron-phonon coupling was included. Vertical colored lines depict the positions where the EDCs shown in figure 5.6b where taken. As seen in the figure the line shape is very complicated and the number of peaks is changing from line to line. In contrast to EDCs, the MDCs always show two easily distinguishable peaks for all energies (see figures 5.6c and 5.6d).

As it was shown in section 3.2 the spectral function measured in photoe-
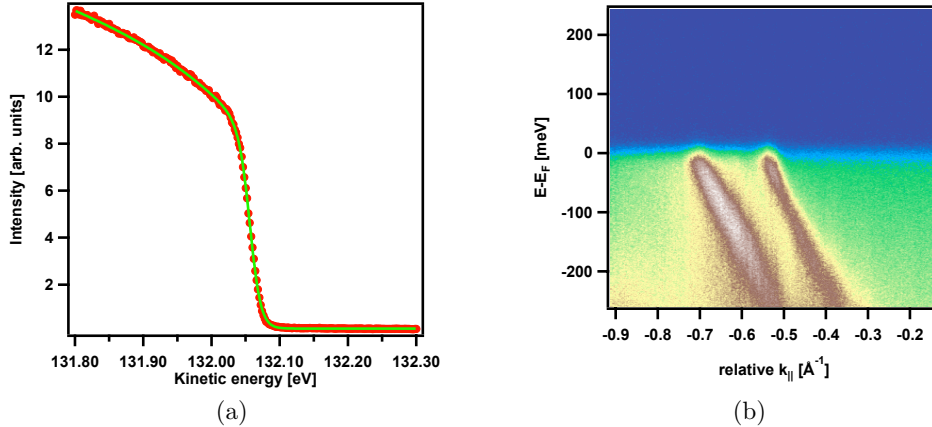

Figure 5.5: (a) Fermi level fit. Red squares represent angle-integrated spectrum, solid green line shows result of the fit. (b) Final image after all normalizations and conversions.
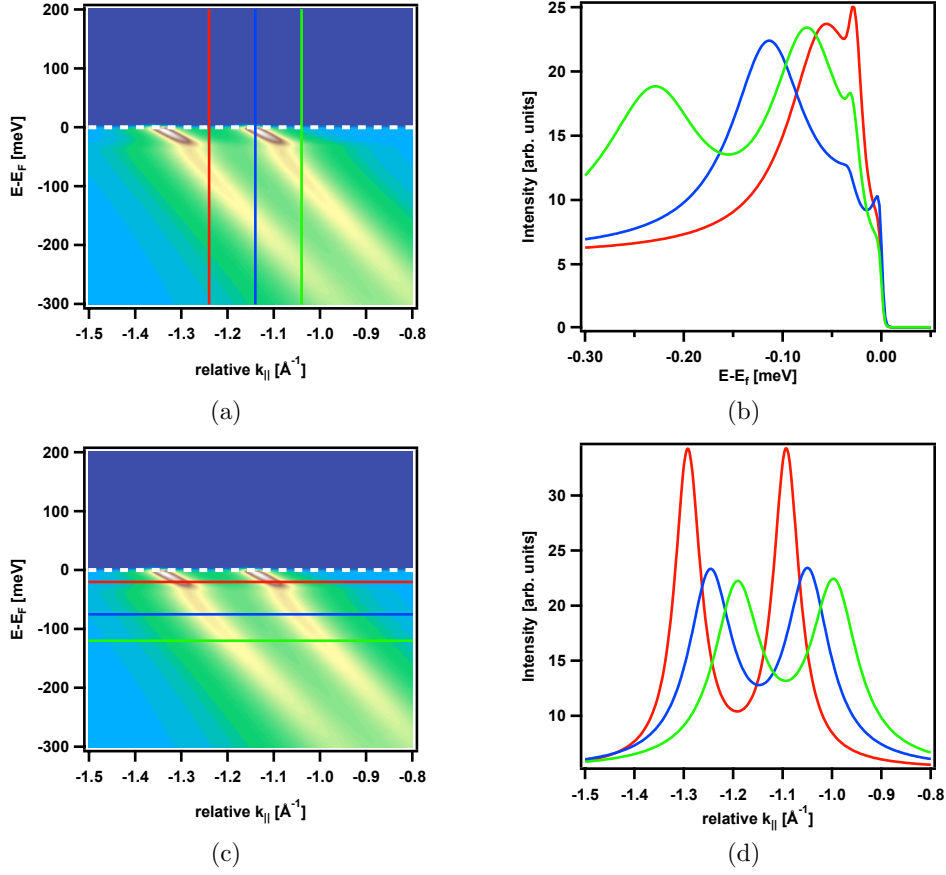
Figure 5.6: Model of two strongly interacting bands (a and c) with (b) EDC
and (d) MDC cuts. Colored vertical (horizontal) lines denotes position where
EDC (MDC) was cut.

mission can be expressed as:

$$A(E, \mathbf{k}) = \frac{1}{\pi} \frac{\operatorname{Im} \Sigma}{(E - E^0(\mathbf{k}) - \operatorname{Re} \Sigma)^2 + \operatorname{Im} \Sigma^2}, \tag{5.3}$$

where Σ is the self energy and $E^0(\mathbf{k})$ is the bare particle dispersion. Taking
into account that the self energy is usually assumed k independent $\Sigma \neq \Sigma(\mathbf{k})$
[77] and that the bare particle dispersion can be represented as the linear
function $E^0(\mathbf{k}) = \hbar v_f(\mathbf{k} - \mathbf{k}_f)$, for a given binding energy equation 5.3 can be
expressed as:

$$A(\mathbf{k}) = I_0 \frac{\omega}{(k - k_0)^2 + \omega^2}, \tag{5.4}$$

which is a Lorenzian line shape by definition. In this expression k_0 defines the
quasiparticle dispersion $k = k(E)$ and ω is the half-width at half-maximum
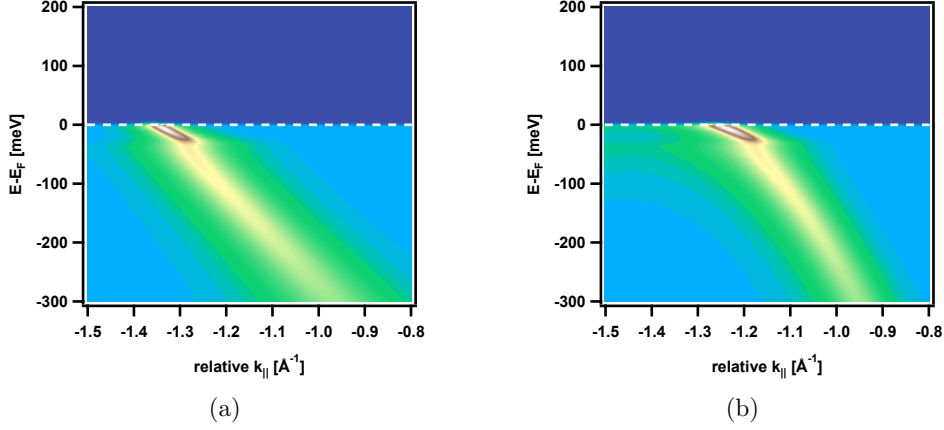(HWHM) of the band. ω is related to the imaginary part of the self energy

75

Figure 5.7: (a) Linear band model. (b) Parabolic band model.

as $\mathrm{Im}\,\Sigma = \hbar v_f \omega$, where v_f is the Fermi velocity. The Fermi velocity is usually estimated as a slope of the fitted dispersion within the first $\approx 50 - 70$ meV. The determination of the Fermi velocity is more complicated, if the band shows electron-electron interaction. As it was explained in section 2.5, the real part of the self energy in case of electron-electron interaction is a linear function which would be added to the quasiparticle dispersion and would contribute to the Fermi velocity. At the moment there is no standard procedure to remove the electron-electron interaction contribution. In our analysis we performed MDC fits of the normalized dataset. Each of the energy momentum distribution curves was expressed as a sum of Lorentzian profiles for each of the present peaks and a linear background. The results of the fit are the dispersions and HWHM's of each of the bands. In our fitting procedures the fit of the first line was done in a manual mode namely the initial guesses for peak position and width had to be manually defined. The rest of the image was fitted in an automatic mode and the results of the previous fit were used as an initial guess for the new MDC. While this technique is working very well for a linear band, it fails to produce the correct band width in case of strongly non-linear band dispersion (see figures 5.8a, 5.8c, 5.8e). Clearly when $E^0(\mathbf{k})$ is non-linear, $A(E, \mathbf{k})$ is not Lorenzian any more. In order to overcome this problem we developed an alternative fitting technique which is the dispersion dependent line shape (DDL) fit. The DDL fit is a fit of the complete spectral function for selected binding energies expressed as:

$$I^{\mathrm{DDL}} = I_0 \frac{\mathrm{Im}\,\Sigma}{(E - E(k) - \mathrm{Re}\,\Sigma)^2 + \mathrm{Im}\,\Sigma^2}, \qquad (5.5)$$
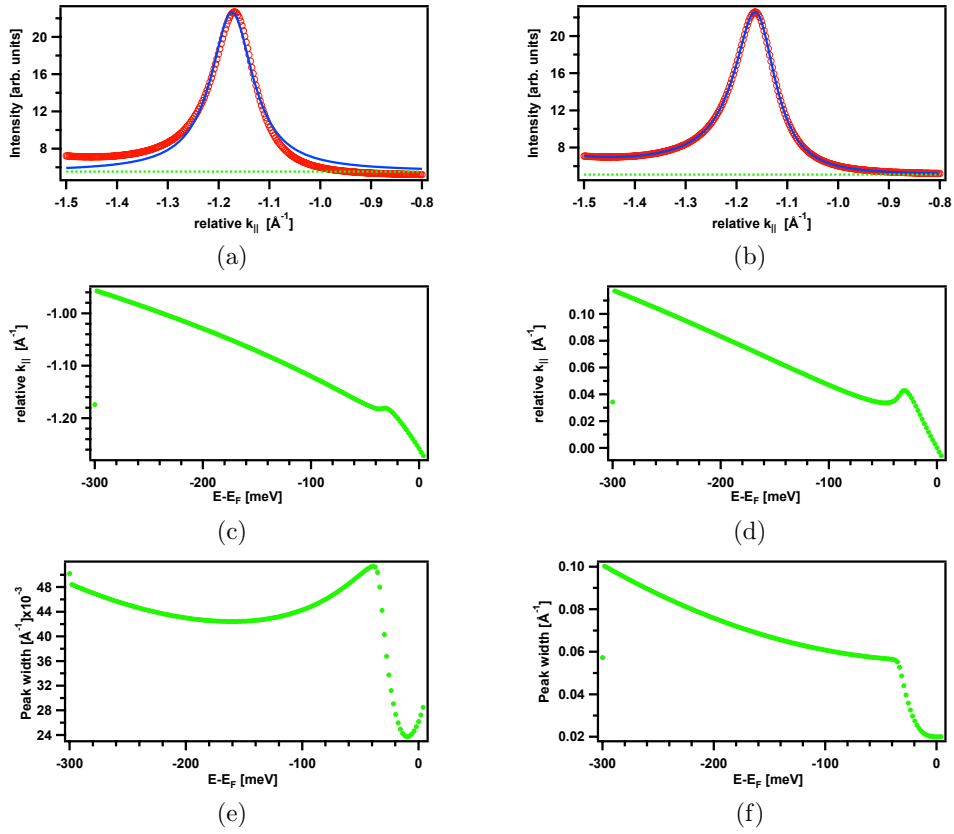
Figure 5.8: A Lorenzian fit (a) can not describe the line shape properly. While the correlated dispersion (c) is defined quite well, the band width (e) shows unreasonable shape. The DDL fit produces a much better fit of the peak (b). The result of the fit can be interpreted as the $\mathrm{Re}\,\Sigma$ (d) and $\mathrm{Im}\,\Sigma$ (f).

where $\mathrm{Im}\,\Sigma$, $\mathrm{Re}\,\Sigma$ and I_0 are the free fit variables, E is the binding energy of the current MDC and $E(k)$ has to be an input parameter to the fit determined by fitting the previous dispersion. When the bare dispersion is exactlly known then the fit produces extremely good results (see figures 5.8b, 5.8d, 5.8f). When the non-correlated dispersion is not known then it can be estimated by the Lorenzian fit as described above. However such a procedure of the bare particle dispersion will also suffer from the same problem as the determination of the Fermi velocity. One of the solutions in this case is to introduce a linear correction term $C * k$ to E(k) and fit it together with $\mathrm{Im}\,\Sigma$, $\mathrm{Re}\,\Sigma$ and I_0. Nevertheless the introduction of this term can lead to an instability in the fitting procedure.

5.3.3 Electron self energy analysis

In the third and last step of the data analysis we investigate the real and imaginary parts of the self energy obtained in the previous step. Usually we estimate quasiparticle couplings present in a band by analyzing the imaginary part of the self energy. Normally each type of coupling has an easily recognizable shape of the self energy. In case of electron-electron coupling $\mathrm{Im}\,\Sigma$ has a quadratic dependence (see section 2.5):

$$\mathrm{Im}\,\Sigma^{El-El}(E,T) = \beta \left[E^2 + (\pi k_B T)^2\right],\qquad(5.6)$$

where β is the coupling constant defining the strength of the interaction. The electron-boson interaction produces a step like function in the imaginary part of the self energy (see section 2.6). In case of the electron-phonon interaction $\mathrm{Im}\,\Sigma$ can be expressed as:

$$\mathrm{Im}\,\Sigma^{el-ph} = 2\pi \int_0^{\hbar\Omega_{max}} \alpha^2 F_k\left(E'\right)\left[2n\left(E'\right) + f\left(E'+E\right) + f\left(E'-E\right)\right],\quad(5.7)$$

where $f(E)$ is the Fermi-Dirac function, $n(E)$ is the Bose-Einstein distribution and $\alpha^2 F_k$ is the Eliashberg function. In case of the Debye model, which we used in our analysis, it can be expressed as:

$$\alpha^2 F(E) = \begin{cases} \lambda \left(\dfrac{E}{\hbar\omega_D}\right)^2 & \text{for } E \leq \hbar\omega_D \\ 0 & \text{for } E > \hbar\omega_D \end{cases},\qquad(5.8)$$

where ω_D is the Debye energy. Finally, the contribution from inelastic scattering as well as from the finite experimental resolution was estimated as a constant offset to the imaginary part of the self energy. We fitted the imaginary part of the self energy obtained in the previous analysis step against the sum of those contributions.

5.3.4 Data modeling

Besides the previously described data analysis procedures we also concentrated on developing a data modeling procedure in order to be able to isolate a few of the following aspects: an accurate estimation of the finite experimental resolution, noise level, analyzer artifacts found in the fitted results and follow the band changes as a function of sample temperature. The data model was also successfully used as source of parameters for the further development of the analysis and fitting algorithms and technique in view of the fact that the results of the fits are required to give the same output as the model input.

In the model we calculated the 2D spectral function as defined by equation 5.5. The implementation of this function was done in Igor Pro 6.05 [78]. The bare particle $E^0(k)$ dispersion was defined as: a) a linear function described by the Fermi velocity and k_F, b) a parabolic function $E^0(k) = W(k - k_0)^2 + \Delta E$ with the following parameters: the center of the parabola defined by k_0, the offset from the Fermi level ΔE and the "opening" of the parabola given by a W coefficient. The quasiparticle interactions are represented by the Debye model (see section 2.6) and the Fermi liquid model (see section 2.5). In a first step, the imaginary part of the self energy $\mathrm{Im}\,\Sigma$ is calculated for both models. Then a constant offset is added to account for impurity scattering and then by using the Kramers-Kronig transformation the real part $\mathrm{Re}\,\Sigma$ is obtained. In the next step, the values of $E^0(k)$, $\mathrm{Im}\,\Sigma(E)$ and $\mathrm{Re}\,\Sigma(E)$ are inserted into 5.5 and the full spectral function is calculated. After calculating the spectral function an offset was added to account for scattered electrons background, then multiplied by the Fermi function. At this point another offset was added with the aim of accounting for the higher orders of the monochromator.

Subsequently the result from the previous step was convoluted with a 2 dimensional Gaussian function that accounts for the finite resolution in both energy and angle directions. In the final step we multiplied with a function that accounts for the noise of the photon beam and added a function that comprises the spectrometer detector noise. No transition matrix element was modeled or included in the simulation.

All the previus figures referred to as models were simulated using the procedure just described.

5.4 Low temperature kinks in Ni metal

The low temperature measurements were performed at a sample temperature of 50 K. We recorded with high resolution *sp*-like bands and *d*-bands.

The experimentally obtained ARPES image of *sp*-like bands is presented in figure 5.9. It is exhibiting two prominent features which are assigned to majority *sp*-like (left) and minority *sp*-like bands. A small increase of the intensity visible in the bottom left corner of the image comes from the minority *d* band. The position of the Fermi level is marked with a white dashed line. Several momentum distribution curves (red circles) and their fits with Lorenzian profiles (fit result shown as solid blue line, separate peaks and background as dashed green lines) at different binding energies are shown in figure 5.10. The overall fit quality is good except for a small feature positioned between the minority and majority peaks. This feature arises from a defect of the detector and can
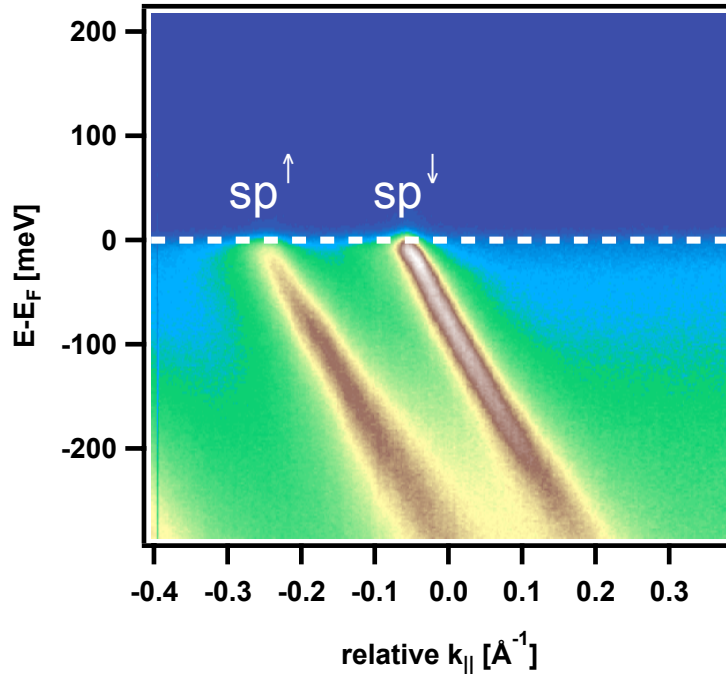
Figure 5.9: ARPES image measured at low temperature ($\approx$ 50K) of Ni (111) surface for *sp*-like bands. The white dashed line denotes the position of the Fermi level.
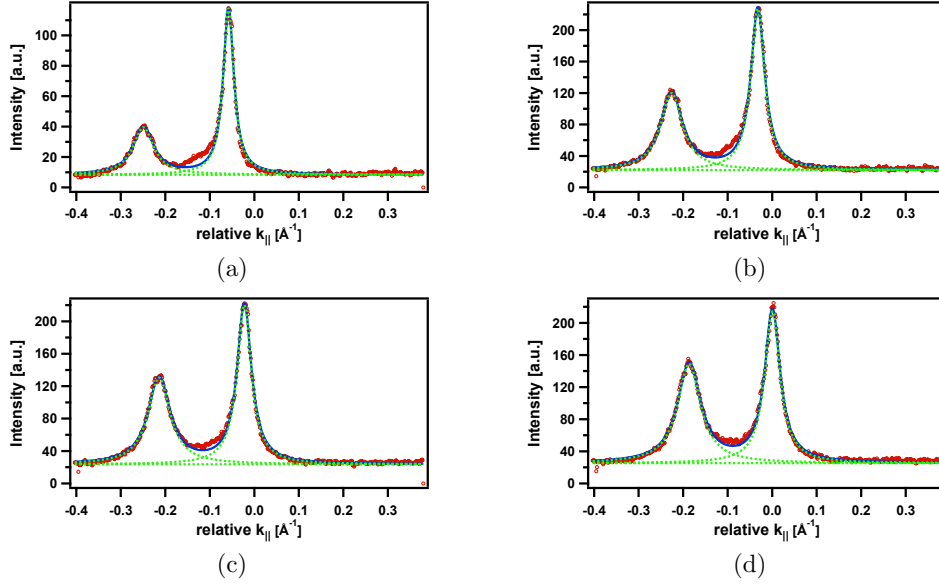
Figure 5.10: Momentum distribution curves (red circles) cut from figure 5.9 and fits (fit result shown as solid blue line, separate peaks and background as dashed green line) at different binding energies. (a) at the Fermi level (E_B=0 meV), (b) E_B=35 meV, (c) E_B=50 meV, (d) E_B=80 meV.

not be completely removed by the normalization procedure. The dispersions and peak widths obtained from the fits are depicted in figures 5.11 and 5.12. The blue symbols in both figures correspond to the minority *sp*-like states, the red ones correspond to the majority states and the dashed line denotes the position of the Fermi level. The green solid lines in figure 5.11 depict a linear fit to the dispersion. Since the fit describes with the measured data very well, we assumed a linear band dispersion in the absence of the kink. From the linear fits we estimated the Fermi velocities as $v_F = 1/\hbar \partial\Sigma/\partial k$ which will give us $v_F^{\uparrow} = 1.88 \pm 0.04$Å/fs for the majority band and $v_F^{\downarrow} = 1.73 \pm 0.04$Å/fs for the minority band.

The difference between the dispersion of the majority band and the line fit is shown in figure 5.13 with red triangles. A small deviation from the linear behavior next to the Fermi level is an artifact arising from the combination of finite experimental energy resolution and intensity drop around the Fermi level. In the same figure the difference between the dispersion of the minority and majority states is plotted using blue triangles. The non zero slope of the curve shows that the Fermi velocities are different for majority and minority bands. A deviation of the linear behavior between 0 and 50 meV can be assigned to the couling to a bosonic mode and was attributed in the literature
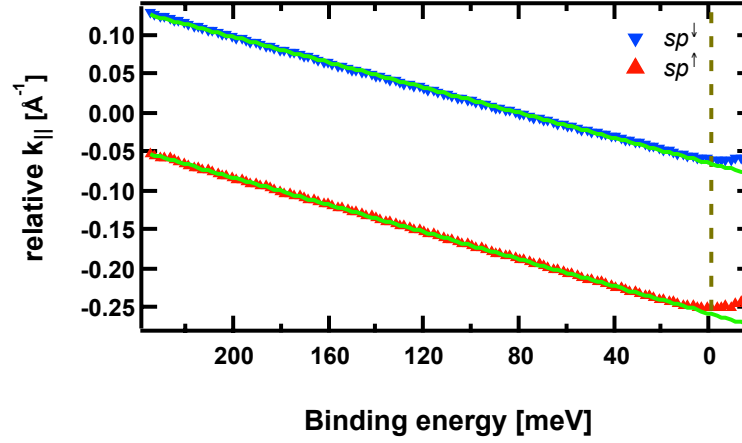
81

Figure 5.11: Dispersion of low temperature ($\approx$ 50K) Ni (111) *sp*-like bands resulting from fit. Blue (red) symbols correspond to minority (majority) states. Solid green lines show the linear fit of the band dispersion. The dashed line denotes the position of the Fermi level.
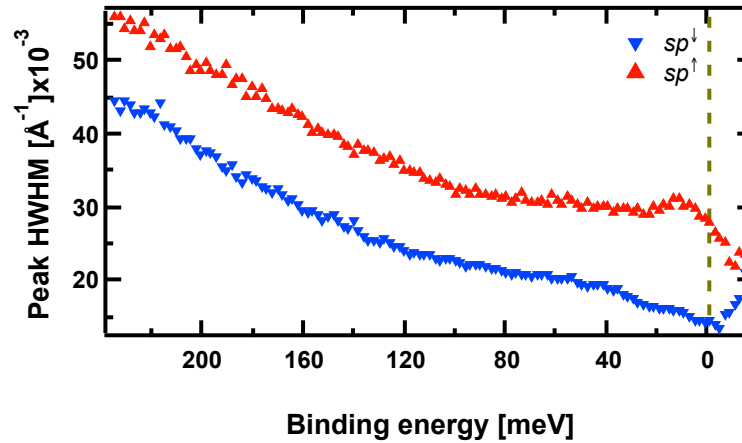

Figure 5.12: HWHM of low temperature ($\approx$ 50K) Ni (111) *sp*-like bands resulting from fit. Blue (red) symbols correspond to minority (majority) states. The dashed line denotes the position of the Fermi level.
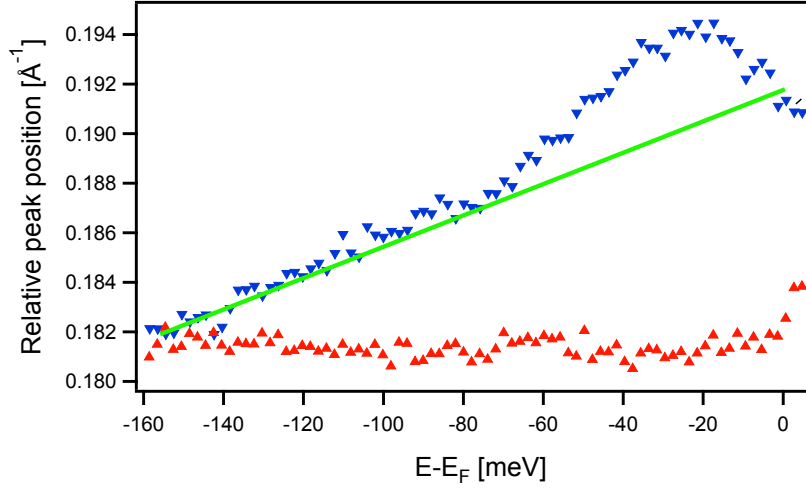
Figure 5.13: Difference of the fitted dispersions. Red symbols represent the difference between the majority *sp*-like band and a line fit of it. Blue symbols represent the difference between the dispersions of the minority and the majority *sp*-like bands. The red curve was offset by 0.182Å^{-1} for presentation purposes. A green line was used as a baseline to estimate the real part of the self energy $\mathrm{Re}\,\Sigma$ for the minority *sp*-like band.

to electron-phonon coupling[50, 79]. By subtracting the baseline, shown in figure 5.13 as a solid green line, we obtain the real part of the self energy of the minority *sp*-like band, plotted in figure 5.14.

From the real part of the self energy we estimate the electron-phonon contribution as a slope around Fermi level: $\lambda = \frac{d\,\mathrm{Re}\,\Sigma}{dE}\big|_{E=E_F}$ (see section 2.6). The obtained value of the coupling constant is $\lambda = 0.21 \pm 0.03$. Knowing the Fermi velocities we could also obtain the imaginary part of the self energy as $\mathrm{Im}\,\Sigma = \hbar v_F \delta k$ (see figure 5.15). Applying the fit procedure described in section 5.3.3 we obtain the electron-phonon coupling $\lambda = 0.19 \pm 0.03$, the Debye energy $E_D = 27 \pm 2$ meV, the electron-electron interaction constant $\beta = 0.48 \pm 0.03$ and the sample temperature $T = 55 \pm 5$ K. The fit result is shown in figure 5.15 as solid green line. The value of the electron-phonon coupling constant obtained by fitting of the $\mathrm{Im}\,\Sigma$ coincides with the value obtained from the slope of $\mathrm{Re}\,\Sigma$ around the Fermi level.

The measured dispersion for *d*-bands is shown in figure 5.16. The high intensity feature in the center of the image corresponds to the minority *d* band, $d^{\downarrow}$. The broad feature below can be identified as the majority *d* band, $d^{\uparrow}$. On the left side the majority *sp*-like band is visible. The position of the Fermi level is marked with a white dashed line. Several momentum distribution curves (red
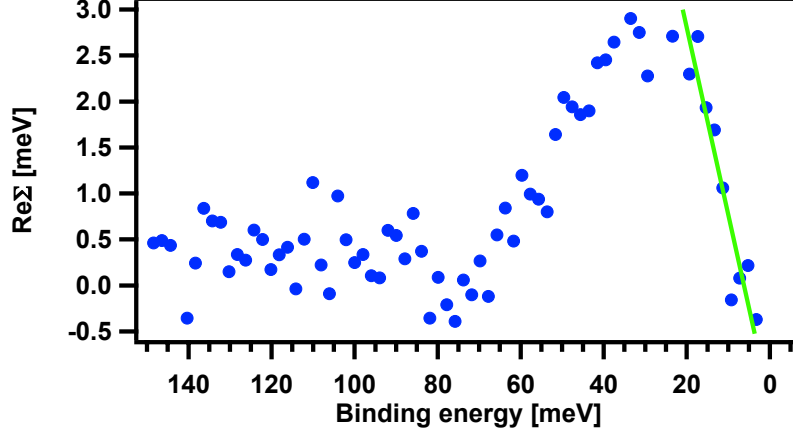
Figure 5.14: Real part of the self-energy for the Ni minority *sp*-like band. Blue circles represent the experimentally obtained real part of the self energy while the solid green line was used to deduce the mass enhancement factor λ.
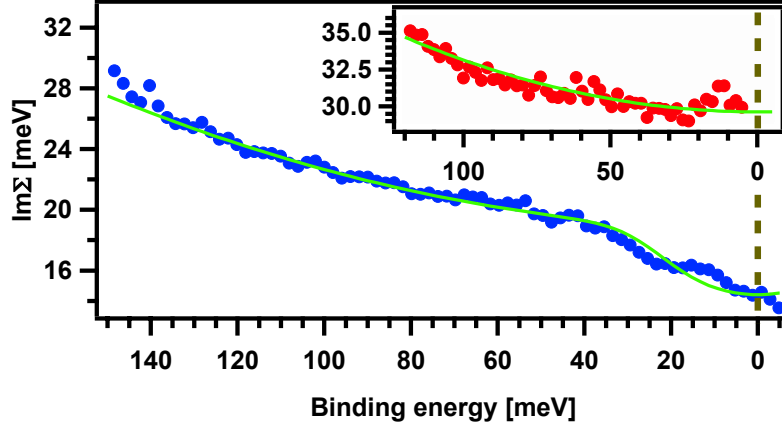

Figure 5.15: Imaginary part of the self-energy for the Ni minority *sp*-like band compared to the model. Blue circles represent the experimentally obtained imaginary part of the self energy while the green line is the fit result with parameters $\lambda = 0.19$, mode energy $E_{mode} = 27$ meV and temperature $T = 55$ K. The dashed line denotes the position of the Fermi level. The inset shows fit of the majority band.
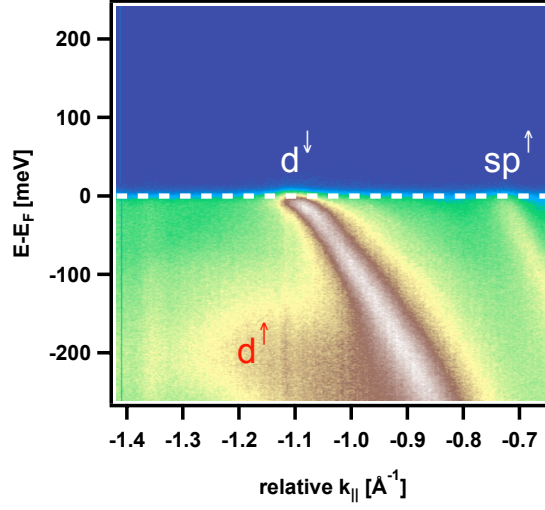
Figure 5.16: ARPES image of Ni (111) surface d-band measured at low temperature ($\approx$ 50K). The white dashed line denotes the position of the Fermi level.

circles) and Lorenzian fits (fit result shown as a solid blue line, separate peaks and background as dashed green lines) at different binding energies are shown in figure 5.17. These plots demonstrate that the momentum distribution curves have a slightly asymmetric line shape.

The dispersion and the peak width obtained from the fit are depicted in figures 5.18 and 5.19, respectively. The blue symbols in both figures correspond to the minority d states and the dashed line denotes the position of the Fermi level. It is obvious that the dispersion of the minority d band is non-linear (see green straight line in figure 5.18). This non-linearity is also contributed to the asymmetry visible in the MDC fits (see section 5.3.2 and figure 5.8a in particular). A much better fit agreement can be achieved by using the DDL fit procedure described above. We used the parabolic fit of the dispersion shown in figure 5.18 to estimate the bare particle dispersion required for the DDL fit. The resulting imaginary part of the self energy is shown in figure 5.20. The Im Σ exhibits a decrease for binding energies $E_B \leq 40$ meV which implies the presence of interaction with a bosonic mode. For higher energies $E_B > 40$ meV the imaginary part of the self energy displays roughly a parabolic increase which we attribute to the electron-electron interaction. The fit of the imaginary part with contributions from the Debye model, Fermi liquid model and constant offset is shown in figure 5.20 with a solid green line. The fit results in values of the electron-phonon coupling constant $\lambda = 0.36 \pm 0.03$, Debye energy $E_{mode} = 35 \pm 0.02$ meV, electron-electron coupling $\beta = 0.74 \pm 0.05$ and
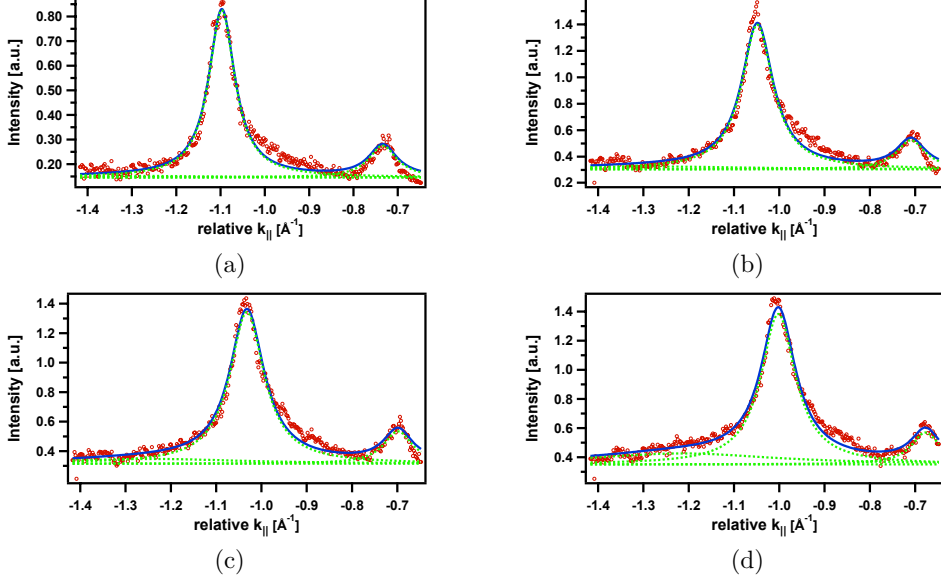
85

Figure 5.17: Momentum distribution curves (red circles) of the Ni minority *d*-band from figure 5.16 and fits (fit result shown as a solid blue line, separate peaks and background as dashed green lines) at different binding energies. (a) at the Fermi level (E_B=0 meV), (b) E_B=35 meV, (c) E_B=50 meV, (d) E_B=80 meV.
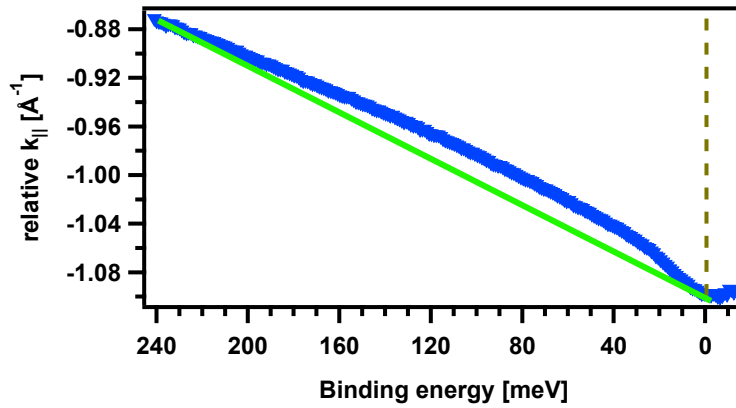

Figure 5.18: Dispersion of the minority *d*-band of Ni (111) at low temperature ($\approx$ 50 K) resulting from fit. The dashed line denotes the position of the Fermi level. The solid green line along the measured dispersion is a guide to the eye that demonstrates that the dispersion is not linear.
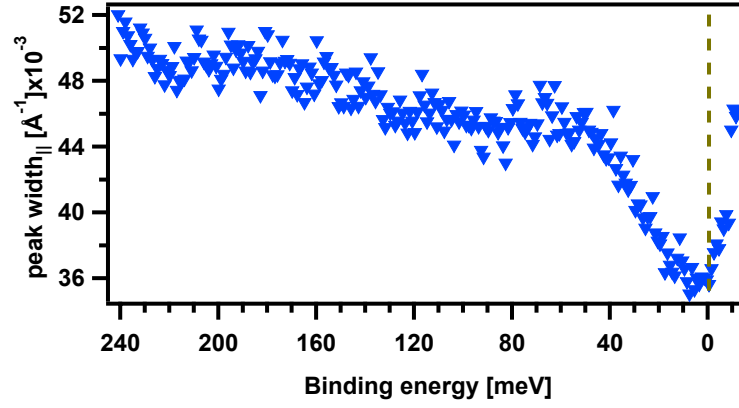
Figure 5.19: HWHM of the minority d-band of Ni (111) at low temperature ($\approx$ 50 K) resulting from fit. The dashed line denotes the position of the Fermi level.
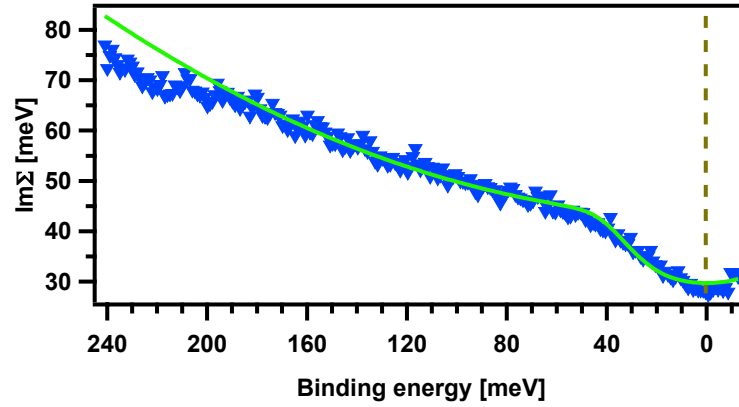

Figure 5.20: Im Σ of minority d-band of Ni (111) at low temperature ($\approx$ 50 K) resulting from fit. Blue symbols represent the experimentally obtained imaginary part of the self energy while the green line is the fit result with parameters $\lambda = 0.36$, mode energy $E_{mode} = 35$ meV and temperature $T = 55$ K

Band	λ	E_{mode}, meV	β	v_f, Å^{-1}/fs
minority d	0.36 ± 0.03	35 ± 2	0.74 ± 0.04	–
minority sp-like	0.20 ± 0.03	27 ± 2	0.48 ± 0.03	1.73 ± 0.02
majority sp-like	–	–	0.59 ± 0.03	1.88 ± 0.03

Table 5.1: The electron-phonon coupling constant (λ), mode energy (E_{mode}), electron-electron coupling constant (β) and Fermi velocity (v_f) evaluated from the experimental results.

temperature $T = 55 \pm 5$ K.

The results are summarized in table 5.1.

The obtained results are similar to the ones reported before by Higashiguchi *et al* [50] but in our case all values are smaller. Contrary to Higashiguchi *et al* we see coupling to different boson modes as clearly indicated by the different energies for sp-like and d bands in table 5.1. The difference in the values may be attributed to the different point in k space measured here.The authors of reference [50] attribute the kink visible in the minority bands to electron-phonon interaction based on the fact that the mode energy value of $\approx 40meV$ coincides well with the value derived from the Debye temperature ($\Theta_D = 450$ K) known to be for Ni $E_D = \Theta_D k_B = 38$ meV[80]. The fact that the kink is present only in the minority bands remains unexplained [50].

The magnitude of λ may be related to the relative weight of the d states for the individual bands. On average d electrons are more localized compared to sp electrons and should be easier influenced by the motion of ions [81]. As it is known from theoretical calculations [50] the minority sp-like band contains approximately 90% of the d weight. While the symmetry of the minority and majority sp-like band is the same, the d weight of the majority band at Fermi energy is slightly smaller ($\approx 80\%$) than for the minority band due to the exchange splitting [50]. Albeit the reduction of the d weight follows the trend (largest coupling for minority d band, smaller for minority sp-like and none for majority sp-like), the difference of $\approx 10\%$ seems too small to explain the absence of the kink structure in majority sp-like band.

We propose to relate the kink to the coupling to a magnon mode. While electron-phonon scattering happens within the same band (see section 2.6) electron-magnon interaction involves two bands with opposite spin character (see section 2.7). This type of transitions at $T = 0$ K temperature can only take place when the photohole generated in the minority band is filled by an

electron from the majority band. Opposite spin flip process are not possible due to the fact that the system has a saturated magnetization at $T = 0$ K. At non zero temperature both absorption and emission of magnons can occur for both majority and minority bands, but the minority spin quasiparticle will always have higher density of states to scatter into. Thus, at low temperatures, electron-magnon interaction should lead to a kink only in minority bands, a fact which is observed in our experiment.

In nickel the magnon dispersion is not linear and at low energies the magnons dispersion could be nearly parabolic [82]:

$$E_{mag} = D\mathbf{q}^2, \tag{5.9}$$

where $\mathbf{q}$ is a magnon wave vector, E_{mag} is the energy of the magnon and $D = 374$ meV/Å^2 for Ni[82]. The parabolic dependence leads to a situation where in case of electron-magnon scattering the only magnon which can be emitted is the one possesing the energy defined by the distance in the momentum space between the minority and majority bands.

We approximate the involved $\mathbf{q}$ values from the bands displayed in figure 5.3. Assuming that minority d- and sp-like holes are filled by electrons in the majority band we obtain $\mathbf{q}_d = \mathbf{k}_d^{\downarrow} - \mathbf{k}_{sp}^{\uparrow} = 0.36 \pm 0.03$ Å^{-1} and $\mathbf{q}_{sp} = \mathbf{k}_{sp}^{\downarrow} - \mathbf{k}_{sp}^{\uparrow} = 0.17 \pm 0.03$ Å^{-1}. Using equation 5.9 we obtain the corresponding magnon energies $E_d = 48.5 \pm 8$ meV and $E_{sp} = 10.8 \pm 3.8$ meV respectively. Comparing to our experimental data ($E_d = 35$ meV and $E_{sp} = 27$ meV, see table 5.1), we see the same tendency, when for the higher $\mathbf{q}$ distance the mode energy is higher. The discrepancy in the values originates from the very cruel model we used. The selected $\mathbf{q}$ values may be not the most probable one as well as the magnon density of states have to be taken into account. Taking this considerations into account should produce better agreement with the measured data.

Our experiment was performed at a higher temperature (≈ 50 K) than the one by Higashiguchi *et al* (10 K). Due to the exchange splitting, the distance between minority and majority band is decreased and this can be another explanation to the reduced values of kink energies observed in our experiment. Coupling to a different magnon could possibly also lead to the change of λ.

Recently, Hofmann et al. have reported a kink structure at 340 meV [83] derived from the electron-magnon interaction in a bulk states of Ni(110) grown on W(110). The low energy kink around 30 meV was also observed in their experiment. The origin of the low energy kink is not discussed by the authors,

nevertheless it is explained as a phonon coupling by referencing the work of Higashiguchi *et al* [50]. The parameters of the low energy kink reported by Hofmann *et al* are a mode energy of 35 meV and a coupling constant of $\lambda = 0.3$. These numbers are in a better agreement with our results than the results of Higashiguchi *et al* [50].

5.5 Temperature dependent quasiparticle renormalization

The experimentally obtained at room temperature ($\approx 320K$) ARPES image of *sp*-like bands is presented in figure 5.21a. The image has to be interpreted in a similar way as the low temperature one. The two bands in the center of the image are assigned to majority *sp*-like, $sp^{\uparrow}$, and minority *sp*-like, $sp^{\downarrow}$, bands. In the bottom left corner of the image a part the minority d band is visible. The experimentally obtained ARPES image of d band is presented in figure 5.22a. The band in the center of the image is assigned to the minority d band, $d^{\downarrow}$. The broad feature at lower-left side of the image is the majority d band, $d^{\uparrow}$. The position of the Fermi level is marked with a white dashed line. The momentum distribution curves (red circles) and their fits with Lorenzian profiles (fit result shown as a solid blue line, separate peaks and background as dashed green lines) at Fermi level for *sp*-like and d bands are shown in figures 5.21b and 5.22b respectively. The overall fit quality of the *sp*-like bands is good and no asymmetry in the line shape is visible. The deviation from pure Lorenzian profile visible in the middle of the plots arises from the defect of the detector and can not be completely removed by the normalization procedure. The presence of the majority d band and relatively poor statistics allows only analysis of the MDC widths at the Fermi level for the minority d band.

The resulting dispersions and band widths of the *sp*-bands fit are shown in figures 5.23 and 5.24 respectively. The blue symbols in both figures correspond to minority states and red – to majority band. The band dispersions can be assumed linear, as demonstrated by the linear function fit shown as a solid green line in figure 5.23. Fermi velocities obtained from the band dispersion are 2.06±0.03 Å/fs for the minority band and 2.04±0.03 Å/fs for the majority. The band width of both bands shows continuous increase within the complete measured energy range. At expected kink energies, there is no abrupt change of the band width visible.

The imaginary part of the self energy obtained by scaling the measured
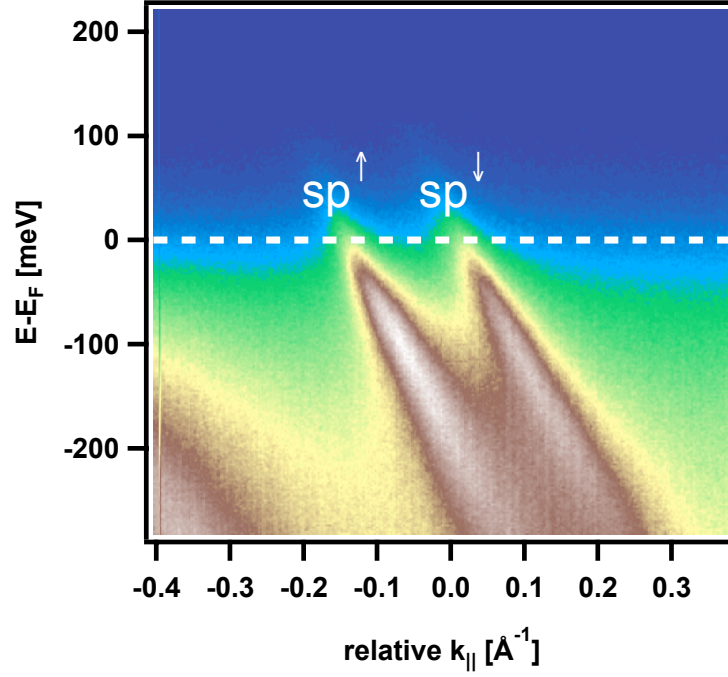
(a)
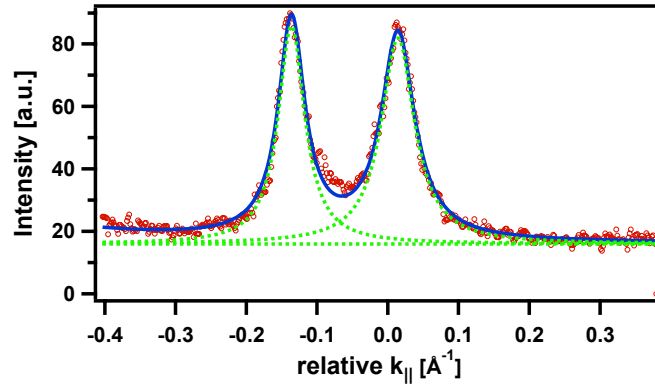
(b)

Figure 5.21: (a) ARPES image of Ni (111) surface for *sp*-like bands measured at room temperature (≈ 320K). The white dashed line denotes the position of the Fermi level. (b) Momentum distribution curves (red circles) cut and fits (fit result shown as solid blue line, separate peaks and background as dashed green line) at $E = E_F$.
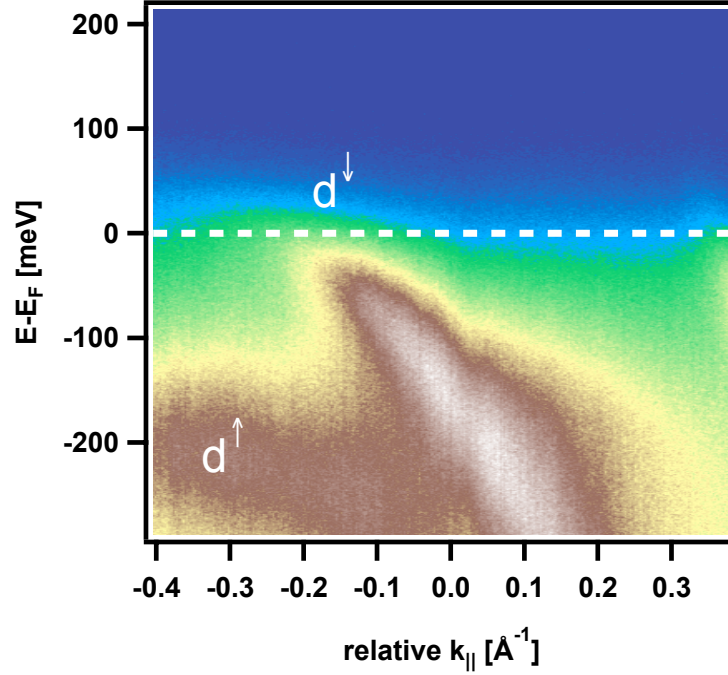
(a)
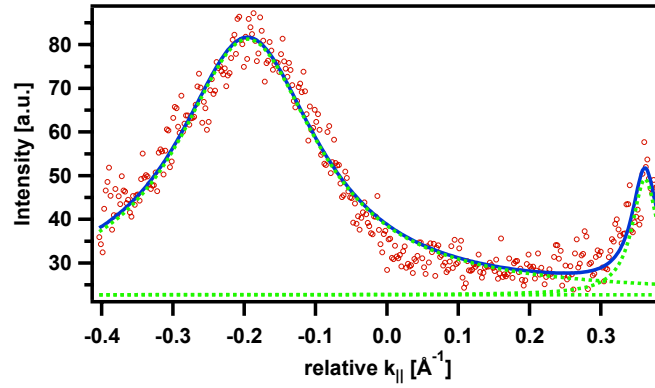
(b)

Figure 5.22: (a) ARPES image of Ni (111) surface for d band measured at room temperature ($\approx$ 320K). The white dashed line denotes the position of the Fermi level. (b) Momentum distribution curves (red circles) cut and fits (fit result shown as solid blue line, separate peaks and background as dashed green line) at $E = E_F$.
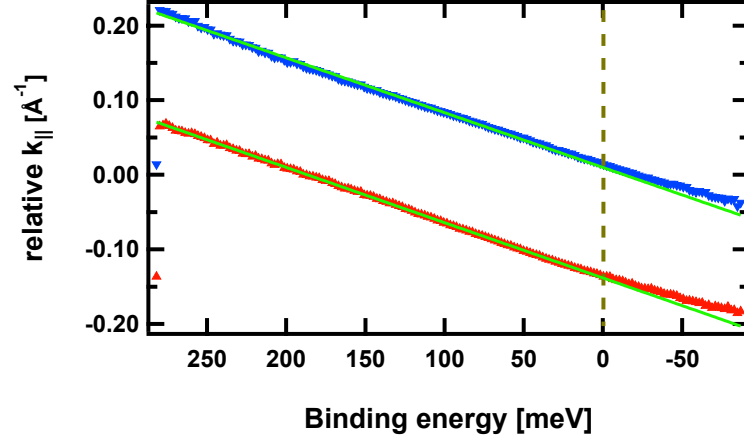
Figure 5.23: Dispersion of room temperature (≈ 320K) Ni (111) *sp*-like bands resulting from fit. Blue (red) symbols correspond to minority (majority) states. Solid green lines show a linear fit of the band dispersion. The dashed line denotes the position of the Fermi level.
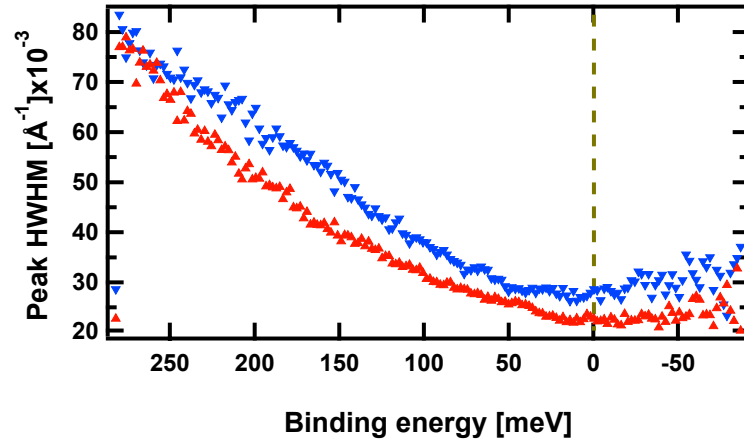

Figure 5.24: HWHM of room temperature (≈ 320K) Ni (111) *sp*-like bands resulting from fit. Blue (red) symbols correspond to minority (majority) states. The dashed line denotes the position of the Fermi level.

93

band with the Fermi velocity is shown in figure 5.25. Im Σ was fitted using
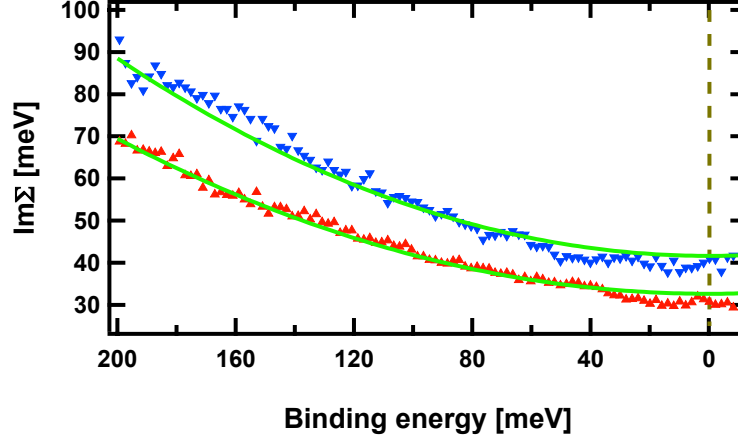

Figure 5.25: Im Σ of room temperature ($\approx$ 320K) Ni (111) *sp*-like bands resulting from fit. Blue (red) symbols correspond to minority (majority) states. Solid green lines show a Fermi liquid model fit of the band dispersion. The dashed line denotes the position of the Fermi level.

the Fermi liquid model (see equation 5.6). The result of the fit is presented as solid green lines in figure 5.25. For the minority *sp*-like band we obtain $\beta = 1.1 \pm 0.09$ and for the majority *sp*-like band $\beta = 0.92 \pm 0.08$. Both values are withing the experimental uncertainty identical. Since no distinct kink features are visible at room temperature, we can assume that electron-boson coupling results and offset independent of binding energy in figure 5.25. Observed increase of the electron-electron coupling constant from $\beta = 0.48$ for the minority *sp*-like band and $\beta = 0.59$ for the majority *sp*-like band at 50 K to $\beta \approx 1$ at 320 K for both bands is rather surprising as it is not expected from the Fermi liquid behavior.

Comparing the imaginary part of the self energy for the low temperature and room temperature cases we find that while the minority *d* and *sp*-like bands show the expected increase in the lifetime broadening at elevated temperature, the majority *sp*-like band behaves anomalously and shows a slightly increasing lifetime. In the following paragraphs we will present a more detailed discussion of this finding.

The temperature dependence of the imaginary part of the self energy for coupling to a bosonic mode (see equation 5.7) predicts that the variation with binding energy of the band width becomes less pronounced at elevated temperatures. It also predicts that the lifetime broadening at the Fermi energy should increase with temperature. For a Fermi liquid, the shape of the imaginary part
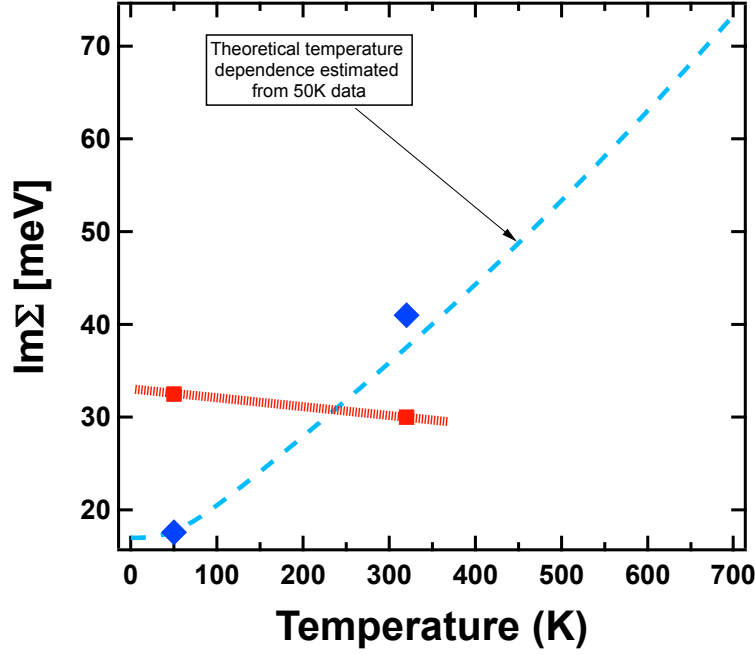
Figure 5.26: Imaginary part of the self energy at the Fermi level. Blue squares show measured $\text{Im}\,\Sigma$ of the minority sp-like band. Red squares depict $\text{Im}\,\Sigma$ of the majority sp-like states. The blue dashed line denotes the increase of the imaginary part of the self energy as expected by electron-phonon interaction model. The red line is just an eye guide.

of self energy due to electron-electron interactions does not change as temperature increases, but it gains a constant offset proportional to the temperature. With increasing temperature we observe a decreasing quasiparticle lifetime at the Fermi level for all probed minority spin bands as expected for electron-phonon coupling. The sp-like minority spin band displays an increase of lifetime broadening from $0.014 \pm 0.003 \text{Å}^{-1}$ to $0.029 \pm 0.002 \text{Å}^{-1}$ between 50 K and 320 K, respectively. The d minority band lifetime broadening increases from $0.038 \pm 0.002 \text{ Å}^{-1}$ to $0.096 \pm 0.004 \text{ Å}^{-1}$, respectively. Surprisingly the majority sp-like spin states behave differently. We actually observe a slightly increased lifetime at room temperature. The width of the majority band decreases with increasing temperature from $0.029 \pm 0.002 \text{ Å}^{-1}$ to $0.023 \pm 0.002 \text{ Å}^{-1}$ corresponding to an actual increase of the elastic mean free path from $34 \pm 2.3 \text{ Å}$ to $43.5 \pm 3.8 \text{ Å}$. The corresponding increase in Fermi velocity from $1.73 \pm 0.03 \text{ Å/fs}$ to $2.04 \pm 0.03 \text{ Å/fs}$ points to a temperature dependent reduction of the majority sp-like spin quasiparticle renormalization.

Another way to look at the band width changes at the Fermi level is to compare values of the imaginary part of the self energy for all the temperatures.

From the set of parameters we defined for the minority band at low temperature: $E_{mode} = 27$ meV, $\lambda = 0.2$ and $\beta = 0.5$ we could calculate the expected increase of the band width as it is predicted by the Debye model and Fermi liquid behavior. The result is shown as a blue dashed line in figure 5.26. Blue diamonds in the same figure show the measured $\text{Im}\,\Sigma$ of the minority sp-like band and red squares depict $\text{Im}\,\Sigma$ of the majority sp-like states. As it follows from the figure, an increase in the lifetime of the minority band coincides very well with the value predicted by the model (the measured $\text{Im}\,\Sigma = 41$ meV and predicted $\text{Im}\,\Sigma = 38$ meV). At the same time the majority band shows a decrease of the $\text{Im}\,\Sigma$ from 32.5 meV to 30 meV.

Although the origin of this novel effect is still unclear it could possibly arise from coupling to spin excitations together with a temperature dependent "undressing" of quasiparticle as evidenced by the the corresponding increase in Fermi velocities. In order to find an explanation of the anomalous behavior we are planning to perform further experiments. We are planning to measure high resolution ARPES data at various k-points of the Ni Fermi surface for an extended accessible temperature range between about 40 K and 500 K. We will complete these measurements by a systematic investigation of the k-dependence. Establishing if 'kinks' are indeed only observed in the minority spin bands would provide a strong indication for the importance of electron-magnon coupling which should affect only the minority bands at low temperatures. We will then investigate the temperature dependence up to about 500K of the individual spin bands. In order to obtain quantitative information about the spectral function we need to account for the increasing thermal broadening with temperature. We aim at adopting a 'deconvolution' procedure developed recently in order to correct for the often insufficient energy resolution in ARPES experiments [84].

Chapter 6

Summary

The first part of this thesis contains a study of the Co_2FeSi Heusler alloy by means of spin-resolved photoelectron spectro-microscopy. For this system 100 % spin polarization at the Fermi edge was predicted, thus making it an attractive candidate for the spintronics applications. Unfortunately the experimentally obtained polarization is much smaller and has a value of 10-12 %. At the beginning of our experiments we performed the commissioning of the spin detectors. Using the spin-resolved circularly polarized $2p$ (L_3) resonant photoemission technique, a spectroscopic tool with the unique property that it is capable of measuring the local $3d$ spin polarization independent of the orientation of the local moment, allowing the study of local moments not only below, but also above T_C, we measured the spin polarization of a thick nickel film and of CuO. By comparing the asymmetry obtained in the experiment with the published spin polarization for these materials we obtained the Sherman function value of 0.07.

Using photoelectron microscopy we demonstrate that the surface of Co_2FeSi sample has areas of mostly non-stoichiometric composition.

Selecting an area on the surface with composition close to the nominal stoichiometry and performing spin-resolved measurements of the valence band we obtained the spin polarization at the Fermi level of 16% which was the highest experimentally determined so far for this material.

The second part of the thesis deals with electron correlation effects in case of nickel bulk material. One of the fundamental consequences of electron correlation effects is that the bare particles in solids become "dressed" with an excitation cloud resulting in quasiparticles. Such a quasiparticle will carry the same spin and charge as the original particle, but will have a renormalized mass and a finite lifetime. The properties of many-body interactions are de-

scribed with a complex function called self energy which is directly accessible to modern high-resolution angle resolved photoemission spectroscopy (ARPES). Usually with increasing temperature the quasiparticle lifetime should decrease due to scattering with phonons. We studied this process spin dependent by looking at ferromagnetic Ni (111) where exchange split majority and minority spin bands are well separated. Surprisingly we found a spin dependent quasiparticle renormalization with unusual temperature dependence where the majority spin lifetime at the Fermi level hardly changes with temperature.

At the low temperature we were able to resolve the kink structure for the minority bands. Estimated values for electron-phonon coupling $\lambda = 0.19 \pm 0.03$, the mode energy $E_{mode} = 27 \pm 2$ meV, the electron-electron interaction constant $\beta = 0.48 \pm 0.03$ for the minority sp-like and $\lambda = 0.36$, $E_{mode} = 35$ meV, $\beta = 0.74$ for minority d band are slightly less than reported before[50]. We attribute the difference in the values to the different points in k space. We proposed to relate the kink not to the electron-phonon interaction, as it explained by Higashiguchi *et al* [50], but to an electron-magnon interaction. Our assumption is based on the fact that the kink is present only in the minority bands as well as that the observed mode energies are different for sp-like and d states. At high temperatures the kink disappears in the line broadening but we could still compare MDCs at the Fermi level. With increasing temperature we observe a decreasing quasiparticle lifetime at the Fermi level for all probed minority spin bands as expected for electron-phonon coupling. The sp-like minority spin band displays an increase of lifetime broadening from 0.014Å^{-1} to 0.029Å^{-1}, while d minority band lifetime broadening increases from 0.038Å^{-1} to 0.096Å^{-1}. Surprisingly the majority spin states behave differently. We actually observe a slightly increased lifetime at room temperature. The width of the majority band decreases with increasing temperature from 0.029Å^{-1} to 0.023Å^{-1} corresponding to an actual increase of the elastic mean free path from 33Å to 43.5Å. The corresponding increase in Fermi velocity from 1.73Å/fs to 2.06Å/fs points to a temperature dependent reduction of the majority spin quasiparticle renormalization. The microscopic origin of this novel effect is still unclear. Further studies may establish if there are compelling effects such a temperature dependent changes of electronic hybridization.

Acknowledgments

Bibliography

[1] P. Grünberg, R. Schreiber, Y. Pang, M. B. Brodsky, and H. Sowers. Layered magnetic structures: Evidence for antiferromagnetic coupling of fe layers across cr interlayers. *Phys. Rev. Lett.*, 57(19):2442–2445, Nov 1986.

[2] M. Julliere. Tunneling between ferromagnetic films. *Physics Letters A*, 54(3):225 – 226, 1975.

[3] R. A. de Groot, F. M. Mueller, P. G. van Engen, and K. H. J. Buschow. New class of materials: Half-metallic ferromagnets. *Phys. Rev. Lett.*, 50(25):2024–2027, Jun 1983.

[4] J. Kübler, A. R. William, and C. B. Sommers. Formation and coupling of magnetic moments in Heusler alloys. *Phys. Rev. B*, 28(4):1745–1755, Aug 1983.

[5] Benjamin Balke, Gerhard H. Fecher, Hem C. Kandpal, Claudia Felser, Keisuke Kobayashi, Eiji Ikenaga, Jung-Jin Kim, and Shigenori Ueda. Properties of the quaternary half-metal-type Heusler alloy $Co_2Mn_{1-x}Fe_xSi$. *Physical Review B (Condensed Matter and Materials Physics)*, 74(10):104405, 2006.

[6] Hem Chandra Kandpal, Gerhard H. Fecher, Claudia Felser, and Gerd Schonhense. Correlation in the transition-metal-based Heusler compounds Co_2MnSi and Co_2FeSi. *Physical Review B (Condensed Matter and Materials Physics)*, 73(9):094422, 2006.

[7] Sabine Wurmehl, Gerhard H. Fecher, Hem Chandra Kandpal, Vadim Ksenofontov, Claudia Felser, and Hong-Ji Lin. Investigation of Co_2FeSi: The Heusler compound with highest Curie temperature and magnetic moment. *Applied Physics Letters*, 88(3):032503, 2006.

[8] Sabine Wurmehl, Gerhard H. Fecher, Hem C. Kandpal, Vadim Ksenofontov, Claudia Felser, Hong-Ji Lin, and Jonder Morais. Geometric,

electronic, and magnetic structure of Co_2]FeSi: Curie temperature and magnetic moment measurements and calculations. *Physical Review B (Condensed Matter and Materials Physics)*, 72(18):184434, 2005.

[9] K. Inomata, S. Okamura, A. Miyazaki, M. Kikuchi, N. Tezuka, M. Wojcik, and E. Jedryka. Structural and magnetic properties and tunnel magnetoresistance for Co_2(Cr,Fe)Al and Co_2FeSi full-Heusler alloys. *Journal of Physics D: Applied Physics*, 39(5):816–823, 2006.

[10] N. Tezuka, S. Okamura, A. Miyazaki, M. Kikuchi, and K. Inomata. Structural dependence of the tunnel magnetoresistance for magnetic tunnel junctions with a full-Heusler Co_2Fe(Al,Si) electrode. *50th Annual Conference on Magnetism and Magnetic Materials*, 99(8):08T314, 2006.

[11] F. Reinert and S. Hüfner. Photoemission spectroscopy with very high energy resolution: Studying the influence of electronic correlations on the millielectronvolt scale. *Very High Resolution Photoelectron Spectroscopy*, pages 13–53, 2007.

[12] N. David Mermin Neil W. Ashcroft. *Solid State Physics*. Brooks Cole, 1976. ISBN: 978-0-03-083993-1.

[13] Charles Kittel. *Introduction to Solid State Physics*. Wiley; 8 edition, 2004.

[14] E. C. Stoner. Collective Electron Ferromagnetism. II. Energy and Specific Heat. *Royal Society of London Proceedings Series A*, 169:339–371, February 1939.

[15] Peter Mohn, editor. *Magnetism in the Solid State: An Introduction*, volume Volume 134 of *Springer Series in Solid-State Sciences*. Springer Berlin Heidelberg, 2006.

[16] S. Hüfner, editor. *Photoelectron Spectroscopy. Principles and Applications*. Springer-Verlag Berlin, 3rd edition, 2003.

[17] A. Einstein. Die plancksche theorie der strahlung und die theorie der spezifischen wärme. *Annalen der Physik*, 327(1):180–190, 1906.

[18] W. L. McMillan and J. M. Rowell. Lead phonon spectrum calculated from superconducting density of states. *Phys. Rev. Lett.*, 14(4):108–112, Jan 1965.

[19] H. Hertz. Ueber sehr schnelle electrische schwingungen. *Annalen der Physik und Chemie*, 267(7):421–448, 1887.

[20] A. Einstein. Über einen die erzeugung und verwandlung des lichtes betreffenden heuristischen gesichtspunkt. *Annalen der Physik*, 322(6):132–148, 1905.

[21] P. D. Innes. the velocity of the cathode particles. *Proceedings of the Royal Society of London*, 79:442, 1907.

[22] K. Seigbahn, C. Nordling, A. Fahlman, R. Nordberg, K. Hamrin, J. Hedman, G. Johansson, T. Bergmark, S. Karlsson, I. Lindgren, and B. Lindberg. Esca, atomic, molecular and solid state structure studied by means of electron spectroscopy. *Nova Acta Regiae Societatis Scientiarum Upsaliensis*, 20:235–236, 1967.

[23] E. Plumer and W. Eberhardt. Angle resolved photoemission as a tool for the study of surfaces. *Advances in Chemical Physics*, 49, 1982.

[24] Daniel R. Bes. *Quantum Mechanics: A Modern and Concise Introductory Course.* Springer Berlin Heidelberg, 2007.

[25] N. V. Smith, P. Thiry, and Y. Petroff. Photoemission linewidths and quasiparticle lifetimes. *Phys. Rev. B*, 47(23):15476–15481, Jun 1993.

[26] Joachim Stöhr. *NEXAFS Spectroscopy.* Springer-Verlag Berlin, 2nd edition, 1996.

[27] Fr. Heusler. Über manganbronze und über die synthese magnetisierbarer legierungen aus unmagnetischen metallen. *Zeitschrift für Angewandte Chemie*, 17(9):260–264, 1904.

[28] Fr. Heusler. *Verh. Deutsch. Phys. Ges.*, 5:219, 1903.

[29] Fr. Heusler, W. Starck, and E. Haupt. *Verh. Deutsch. Phys. Ges.*, 5:220, 1903.

[30] O. Heusler. *Ann. Phys. (Leipzig)*, 19:155, 1934.

[31] Andrei Gloskovskii, Joachim Barth, Benjamin Balke, Gerhard H Fecher, Claudia Felser, Florian Kronast, Ruslan Ovsyannikov, Hermann Durr,

Wolfgang Eberhard, and Gerd Schonhense. A spatially resolved investigation of the local, micro-magnetic domain structure of single and polycrystalline co2fesi. *Journal of Physics D: Applied Physics*, 40(6):1570–1575, 2007.

[32] N. F. Mott. The scattering of fast electrons by atomic nuclei. *Proceedings of the Royal Society of London. Series A, Containing Papers of a Mathematical and Physical Character (1905-1934)*, 124(794):425–442, June 1929.

[33] J. Kessler. *Polarized Electrons*. Springer, Berlin, 2nd edition, 1985.

[34] V. N. Petrov, V. V. Grebenshikov, B. D. Grachev, and A. S. Kamochkin. New compact classical 40 kV Mott polarimeter. *Review of Scientific Instruments*, 74(3):1278–1281, 2003.

[35] V. N. Petrov, M. Landolt, M. S. Galaktionov, and B. V. Yushenkov. A new compact 60 kv mott polarimeter for spin polarized electron spectroscopy. *Review of Scientific Instruments*, 68(12):4385–4389, 1997.

[36] M. Taborelli, R. Allenspach, and M. Landolt. Spin-polarized auger electron spectroscopy on gd. *Phys. Rev. B*, 34(9):6112–6116, Nov 1986.

[37] L. H. Tjeng, B. Sinkovic, N. B. Brookes, J. B. Goedkoop, R. Hesper, E. Pellegrin, F. M. F. de Groot, S. Altieri, S. L. Hulbert, E. Shekel, and G. A. Sawatzky. Spin-resolved photoemission on anti-ferromagnets: Direct observation of Zhang-Rice singlets in CuO. *Phys. Rev. Lett.*, 78(6):1126–1129, Feb 1997.

[38] J. Ghijsen, L. H. Tjeng, H. Eskes, G. A. Sawatzky, and R. L. Johnson. Resonant photoemission study of the electronic structure of cuo and *cu*2o. *Phys. Rev. B*, 42(4):2268–2274, Aug 1990.

[39] H. Eskes, L. H. Tjeng, and G. A. Sawatzky. Cluster-model calculation of the electronic structure of cuo: A model material for the high-*tc* superconductors. *Phys. Rev. B*, 41(1):288–299, Jan 1990.

[40] L. H. Tjeng, C. T. Chen, J. Ghijsen, P. Rudolf, and F. Sette. Giant cu 2p resonances in cuo valence-band photoemission. *Phys. Rev. Lett.*, 67(4):501–504, Jul 1991.

[41] B. Sinkovic, L. H. Tjeng, N. B. Brookes, J. B. Goedkoop, R. Hesper, E. Pellegrin, F. M. F. de Groot, S. Altieri, S. L. Hulbert, E. Shekel, and G. A. Sawatzky. Local electronic and magnetic structure of Ni below and above T_C: A spin-resolved circularly polarized resonant photoemission study. *Phys. Rev. Lett.*, 79(18):3510–3513, Nov 1997.

[42] P. Fulde. *Electron Correlations in Molecules and Solids*, volume 100 of *Springer Series in Solid-State Sciences*. Springer-Verlag, Berlin, 1991.

[43] Werner Smekal, Wolfgang S. M. Werner, and Cedric J. Powell. Simulation of electron spectra for surface analysis (SESSA): a novel software tool for quantitative Auger-electron spectroscopy and X-ray photoelectron spectroscopy. *Surface and Interface Analysis*, 37(11):1059–1067, 2005.

[44] Wolfgang S. M. Werner. Electron transport in solids for quantitative surface analysis. *Surface and Interface Analysis*, 31(3):141–176, 2001.

[45] Gerhard H Fecher, Benjamin Balke, Siham Ouardi, Claudia Felser, Gerd Schönhense, Eiji Ikenaga, Jung-Jin Kim, Shigenori Ueda, and Keisuke Kobayashi. High energy, high resolution photoelectron spectroscopy of $Co_2Mn_{1-x}Fe_xSi$. *Journal of Physics D: Applied Physics*, 40(6):1576–1581, 2007. Hol 19.

[46] W. H. Wang, M. Przybylski, W. Kuch, L. I. Chelaru, J. Wang, Y. F. Lu, J. Barthel, H. L. Meyerheim, and J. Kirschner. Magnetic properties and spin polarization of Co_2MnSi Heusler alloy thin films epitaxially grown on GaAs(001). *Physical Review B (Condensed Matter and Materials Physics)*, 71(14):144416, 2005.

[47] W.H. Wang, M. Przybylski, W. Kuch, L.I. Chelaru, J. Wang, Y.F. Lu, J. Barthel, and J. Kirschner. Spin polarization of single-crystalline Co_2MnSi films grown by PLD on GaAs(001). *Journal of Magnetism and Magnetic Materials*, 286:336–339, 2005.

[48] G. Schnhense and H. C. Siegmann. Transmission of electrons through ferromagnetic material and applications to detection of electron spin polarization. *Annalen der Physik*, 505(5):465–474, 1993.

[49] M. Getzlaff, J. Bansmann, and G. Schnhense. Spin-polarization effects for electrons passing through thin iron and cobalt films. *Solid State Communications*, 87(5):467–469, August 1993.

[50] Mitsuharu Higashiguchi, Kenya Shimada, Keisuke Nishiura, Xiaoyu Cui, Hirofumi Namatame, and Masaki Taniguchi. Energy band and spin-dependent many-body interactions in ferromagnetic Ni(110): A high-resolution angle-resolved photoemission study. *Physical Review B (Condensed Matter and Materials Physics)*, 72(21):214438, 2005.

[51] Andrea Damascelli, Zahid Hussain, and Zhi-Xun Shen. Angle-resolved photoemission studies of the cuprate superconductors. *Rev. Mod. Phys.*, 75(2):473–541, Apr 2003.

[52] A. Lanzara, P. V. Bogdanov, X. J. Zhou, S. A. Kellar, D. L. Feng, E. D. Lu, T. Yoshida, H. Eisaki, A. Fujimori, K. Kishio, J.-I. Shimoyama, T. Noda, S. Uchida, Z. Hussain, and Z.-X. Shen. Evidence for ubiquitous strong electron-phonon coupling in high-temperature superconductors. *Nature*, 412(6846):510–514, August 2001.

[53] M Bowen, J-L Maurice, A Barthelemy, M Bibes, D Imhoff, V Bellini, R Bertacco, D Wortmann, P Seneor, E Jacquet, A Vaures, J Humbert, J-P Contour, C Colliex, S Blugel, and P H Dederichs. Using half-metallic manganite interfaces to reveal insights into spintronics. *Journal of Physics: Condensed Matter*, 19(31):315208 (27pp), 2007.

[54] D. E. Eastman, F. J. Himpsel, and J. A. Knapp. Experimental exchange-split energy-band dispersions for Fe, Co, and Ni. *Phys. Rev. Lett.*, 44(2):95–98, Jan 1980.

[55] F. J. Himpsel, J. A. Knapp, and D. E. Eastman. Experimental energy-band dispersions and exchange splitting for Ni. *Phys. Rev. B*, 19(6):2919–2927, Mar 1979.

[56] W. Eberhardt and E. W. Plummer. Angle-resolved photoemission determination of the band structure and multielectron excitations in Ni. *Phys. Rev. B*, 21(8):3245–3255, Apr 1980.

[57] P. Aebi, T. J. Kreutz, J. Osterwalder, R. Fasel, P. Schwaller, and L. Schlapbach. k-space mapping of majority and minority bands on the fermi surface of nickel below and above the curie temperature. *Phys. Rev. Lett.*, 76(7):1150–1153, Feb 1996.

[58] T. J. Kreutz, T. Greber, P. Aebi, and J. Osterwalder. Temperature-dependent electronic structure of nickel metal. *Phys. Rev. B*, 58(3):1300–1317, Jul 1998.

[59] S. Hüfner and G. K. Wertheim. Multielectron effects in the xps spectra of nickel. *Physics Letters A*, 51(5):299 – 300, 1975.

[60] R. Clauberg, W. Gudat, E. Kisker, E. Kuhlmann, and G. M. Rothberg. Nature of the resonant 6-ev satellite in ni: Photoelectron spin-polarization analysis. *Phys. Rev. Lett.*, 47(18):1314–1317, Nov 1981.

[61] Y. Sakisaka, T. Komeda, M. Onchi, H. Kato, S. Masuda, and K. Yagi. New observation of the valence-band satellite in ni(110). *Phys. Rev. Lett.*, 58(7):733–736, Feb 1987.

[62] A. Kakizaki, J. Fujii, K. Shimada, A. Kamata, K. Ono, K.-H. Park, T. Kinoshita, T. Ishii, and H. Fukutani. Fluctuating local magnetic moments in ferromagnetic ni observed by the spin-resolved resonant photoemission. *Phys. Rev. Lett.*, 72(17):2781–2784, Apr 1994.

[63] J. Bunemann, F. Gebhard, T. Ohm, R. Umstatter, S. Weiser, W. Weber, R. Claessen, D. Ehm, A. Harasawa, A. Kakizaki, A. Kimura, G. Nicolay, S. Shin, and V. N. Strocov. Atomic correlations in itinerant ferromagnets: Quasi-particle bands of nickel. *EPL (Europhysics Letters)*, 61(5):667–673, 2003.

[64] K.-P. Kämper, W. Schmitt, and G. Güntherodt. Temperature and wave-vector dependence of the spin-split band structure of ni(111) along the γ-l line. *Phys. Rev. B*, 42(16):10696–10705, Dec 1990.

[65] M. Mulazzi, M. Hochstrasser, M. Corso, I. Vobornik, J. Fujii, J. Osterwalder, J. Henk, and G. Rossi. Matrix element effects in angle-resolved valence band photoemission with polarized light from the Ni(111) surface. *Physical Review B (Condensed Matter and Materials Physics)*, 74(3):035118, 2006.

[66] H. Hopster, R. Raue, G. Güntherodt, E. Kisker, R. Clauberg, and M. Campagna. Temperature dependence of the exchange splitting in ni studied by spin-polarized photoemission. *Phys. Rev. Lett.*, 51(9):829–832, Aug 1983.

[67] Eberhard Dietz, Ulrich Gerhardt, and Christa J. Maetz. Exchange splitting in nickel. *Phys. Rev. Lett.*, 40(13):892–896, Mar 1978.

[68] K. Ono, A. Kakizaki, K. Tanaka, K. Shimada, Y. Saitoh, and T. Sendohda. Electron correlation effects in ferromagnetic ni observed by spin- and

angle-resolved photoemission. *Solid State Communications*, 107(4):153 – 157, 1998.

[69] C. S. Wang and J. Callaway. Energy bands in ferromagnetic nickel. *Phys. Rev. B*, 15(1):298–306, Jan 1977.

[70] F. Weling and J. Callaway. Semiempirical description of energy bands in nickel. *Phys. Rev. B*, 26(2):710–719, Jul 1982.

[71] David R. Penn. Effect of bound hole pairs on the *d*-band photoemission spectrum of ni. *Phys. Rev. Lett.*, 42(14):921–925, Apr 1979.

[72] Ansgar Liebsch. Effect of self-energy corrections on the valence-band photoemission spectra of ni. *Phys. Rev. Lett.*, 43(19):1431–1434, Nov 1979.

[73] Leonard Kleinman. Correlation effects on the energy band of ni. *Phys. Rev. B*, 19(2):1295–1298, Jan 1979.

[74] G. Treglia, F. Ducastelle, and D. Spanjaard. Comments on the electronic structure of nickel. *Phys. Rev. B*, 21(8):3729–3733, Apr 1980.

[75] D. M. Riffe and G. K. Wertheim. Submonolayer oxidation of W(110): a high-resolution core-level photoemission study. *Surface Science*, 399(2-3):248–263, March 1998.

[76] L. P. Bouckaert, R. Smoluchowski, and E. Wigner. Theory of brillouin zones and symmetry properties of wave functions in crystals. *Phys. Rev.*, 50(1):58–67, Jul 1936.

[77] F. J. Himpsel, K. N. Altmann, G. J. Mankey, J. E. Ortega, and D. Y. Petrovykh. Electronic states in magnetic nanostructures. *Journal of Magnetism and Magnetic Materials*, 200(1-3):456 – 469, 1999.

[78] see http://www.wavemetrics.com/.

[79] Mitsuharu Higashiguchi, Kenya Shimada, Keisuke Nishiura, Xiaoyu Cui, Hirofumi Namatame, and Masaki Taniguchia. High-resolution angle-resolved photoemission study of Ni(110). *Journal of Electron Spectroscopy and Related Phenomena*, 144147:639–642, 2005.

[80] R. J. Birgeneau, J. Cordes, G. Dolling, and A. D. B. Woods. Normal modes of vibration in nickel. *Phys. Rev.*, 136(5A):A1359–A1365, Nov 1964.

[81] G. D. Gaspari and B. L. Gyorffy. Electron-phonon interactions, d resonances, and superconductivity in transition metals. *Phys. Rev. Lett.*, 28(13):801–805, Mar 1972.

[82] S. J. Pickart, H. A. Alperin, V. J. Minkiewicz, R. Nathans, G. Shirane, and O. Steinsvoll. Spin-wave dispersion in ferromagnetic Ni and fcc Co. *Phys. Rev.*, 156(2):623–626, Apr 1967.

[83] A. Hofmann, X. Y. Cui, J. Schäfer, S. Meyer, P. Höpfner, C. Blumenstein, M. Paul, L. Patthey, E. Rotenberg, J. Bünemann, F. Gebhard, T. Ohm, W. Weber, and R. Claessen. Renormalization of bulk magnetic electron states at high binding energies. *Physical Review Letters*, 102(18):187204, 2009.

[84] H.-B. Yang, J. D. Rameau, P. D. Johnson, T. Valla, A. Tsvelik, and G. D. Gu. Emergence of preformed cooper pairs from the doped mott insulating state in bi2sr2cacu2o8+[dgr]. *Nature*, 456(7218):77–80, November 2008.